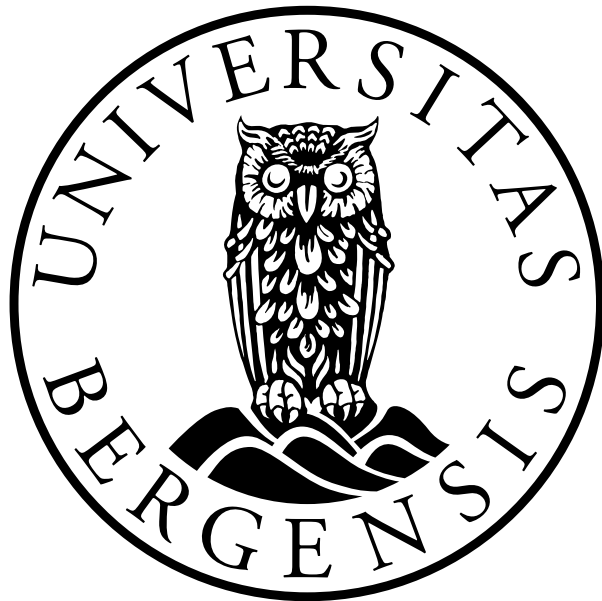


Surface coil development for multinuclear MRI

Master's Thesis in Medical Technology

by

Mari Maaløy Alsaker



Department of Physics and Technology
University of Bergen

Date: June 2, 2024

Abstract

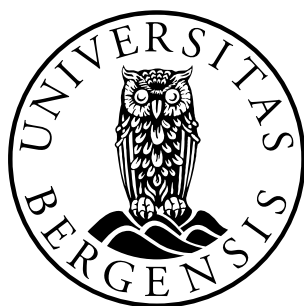
Multinuclear imaging is a topic of research with great potential within Magnetic Resonance Imaging (MRI). Since the first Nuclear Magnetic Resonance experiments, it was known that many different nuclei could be analyzed with this technique, for example, hydrogen (1H), carbon (^{13}C), and sodium (^{23}Na). However, clinical use of MRI today has focused on the hydrogen nucleus because of its superior magnetic properties. The availability of hydrogen MRI systems at high (3T) and ultra-high (7T) magnetic fields has increased because of a desire for images with higher resolution. Increased field strengths increase the Signal to Noise Ratio (SNR) of the scans, which can be exploited to increase the spatial resolution of the final images. Higher fields also increase the SNR of the nuclei with less favorable magnetic properties than hydrogen. An intriguing nucleus with suitable MRI properties in the context of human physiology is ^{23}Na , despite its intrinsically low SNR caused by its lower gyromagnetic ratio, low concentrations in vivo, and shorter relaxation time. ^{23}Na plays a significant role in several parts of the human body, for example, the musculoskeletal system and the brain. The physiological information of a sodium MRI (^{23}Na -MRI) scan combined with the anatomical information from a 1H -MRI scan has the potential to answer questions about human physiology in general and abnormal conditions. This project aimed to develop sodium Radio Frequency (RF) surface coils for ^{23}Na -MRI at 3T with an increased SNR in a particular Region of Interest (ROI) in the brain (visual cortex area) compared to a birdcage head coil and general-purpose surface coils.

Three designs were included: a simple transceiver single-loop surface coil, a simple enhancing secondary resonator to enhance the field of a birdcage head coil during reception, and a transceiver quadrature surface coil consisting of two loops similar to the single-loop. All coils had geometric shapes fitting to the ROI. The coils' performances were all analyzed through laboratory measurements and phantom MRI scans with a radial 3D cones (CN) Ultra-short Echo Time (UTE) sequence specialized for imaging ^{23}Na with its short relaxation times.

The two transceiver coils successfully increased SNR in the defined ROI. The quadrature coil had the superior SNR because of its circularly polarized magnetic field combined with the specialized shape. This coil provided a more inhomogeneous field than the single-loop coil, but inhomogeneity corrections were successfully applied using the Double-Angle Method (DAM). The enhancing coil successfully enhanced the birdcage coil's field in a slightly different region than expected. Static field calculations were used to explain this, requiring further confirmation. The three in-house developed coils may be suitable for in vivo ^{23}Na -MRI scans.

Scientific environment

This master thesis work was carried out at the Department of Physics and Technology at the University of Bergen, Norway, in collaboration with the Max Planck Institute for Biological Cybernetics in Tübingen, Germany. The work was supported by researchers at the Mohn Medical Imaging and Visualisation Centre (MMIV).



Department of Physics and Technology, Faculty of Mathematics and Natural Sciences



Mohn Medical Imaging and Visualisation Centre (MMIV).



MAX PLANCK INSTITUTE
FOR BIOLOGICAL CYBERNETICS



Max Planck Institute (MPI) for Biological Cybernetics.

Acknowledgements

I want to thank my supervisors, Frank Riemer and Renate Grüner, for inspiring and helping me through the work with this thesis. Thank you for sharing your knowledge with me and connecting me with so many helpful people in your research environment. Thank you for introducing me to the Mohn Medical Imaging and Visualisation Centre (MMIV) researchers, with whom I enjoyed many interesting discussions about my project. Thank you to Ivan Maximov, who established contact with RF coil specialist and senior research scientist Nicolai Avdievitch at the Max Planck Institute (MPI) of Biological Cybernetics in Tübingen, Germany. Nicolai Avdievitch provided essential guidance in design choices and implementation of the coil designs. Thank you, Nikolai, for investing time in my project through several digital meetings, personal meetings in Bergen in August 2023, and receiving me in Tübingen in October 2023 (travel costs covered by the national network of precision imaging and machine learning (PRESIMAL)). Thank you, postdoc Georgiy Solomakha at MPI, for personal guidance in coil construction and for showing me around during my stay in Tübingen. The trip to Tübingen provided me with substantial input from experienced RF coil engineers and access to ideal components for RF coils, increasing the likelihood of success and widening this project's scope.

I want to express my gratitude for the help I received from the Medical Technical Department at Haukeland University Hospital. A special thank you to electrician Alaa Sulaiman Ali Assadi for helping me better understand RF circuits and to Rolf Arne Haakonsen at the 3D printing lab for swiftly realizing my coil designs.

Thank you to Lars Ersland and Alexander Richard Craig-Craven for sharing their research time on the MRI system and for showing enthusiasm for my project. Thank you to Nordic Neuro Lab for letting me use their laboratories and lending me their laboratory instruments, especially the pocketVNA. Thank you to Attiq Ur Rehman for finding a laboratory workplace for me at the Department of Physics and Technology, University of Bergen.

Furthermore, I would like to thank my parents and close friends for listening to all my thoughts and reflections on this project for the past year and showing enthusiasm for my work. Thank you to my fellow students for all the collaboration, exciting conversations, and much-needed distractions over the past five years.

Mari Maaløy Alsaker
Bergen, June 2, 2024

Nomenclature

Abbreviations

2D	two-dimensional
3D	three-dimensional
^{23}Na-MRI	sodium MRI
AC	Alternating Current
ADC	Analog-to-Digital Converter
BOLD	Blood Oxygenation Level Dependant contrast
CAD	Computer Aided Design
CAE	Computer Aided Engineering
CAM	Computer Aided Manufacturing
CN	3D cones
CT	Computed Tomography
DAM	Double-Angle Method
DUT	Device Under Test
FID	Free Induction Decay
FOV	Field Of View
MDR	Medical Device Regulation
MRI	Magnetic Resonance Imaging

MROI	Measurement Region of Interest
MS	Multiple Sclerosis
NEMA	National Electrical Manufacturers Association
NMR	Nuclear Magnetic Resonance
PCB	Printed Circuit Board
PET	Positron Emission Tomography
PET-G	Polyethylene Terephthalate Glycol
PLA	Polylactic Acid
RF	Radio Frequency
ROI	Region of Interest
SAR	Specific Absorption Rate
SMA	SubMiniature version A
SNR	Signal to Noise Ratio
SOL	Short-Open-Load
SOLT	Short-Open-Load-Through
SPECT	Single Photon Emission Computed Tomography
SR	Self Resonance
STL	Stereolithography
TE	Echo Time
TR	Repetition Time
TSC	Tissue total Sodium Concentration
UTE	Ultra-short Echo Time
VDC	Volts of Direct Current
VNA	Vector Network Analyzer

Symbols

$\Delta\alpha$	flip angle
δ	skin depth
ϵ_p	permittivity
γ	gyromagnetic ratio
\hbar	reduced Planck constant
μ_p	permeability
ω_0	Larmor frequency
$\vec{\mu}$	magnetic moment
\vec{M}	net magnetization vector
τ	torque
\mathcal{E}	electromotive force
B_1	RF pulse
B_0	main magnetic field flux density
C	capacitance
c	speed of light
H	Henry
J	intrinsic angular momentum
k	Boltzmann's constant
L	inductance
M_0	net magnetization equilibrium value
q	electric charge
s	spin quantum number
T_1	spin-lattice relaxation time

T_2	spin-spin relaxation time
Z_0	characteristic impedance
Z	atomic number

Contents

	Page
Abstract	iii
Scientific environment	v
Acknowledgements	vii
Nomenclature	ix
List of Figures	xvii
List of Tables	xviii
1 Introduction	1
1.1 Motivation	2
1.2 Recent developments and Contribution	2
1.3 Problem Statement and thesis outline	3
2 Theory	5
2.1 MRI	5
2.1.1 Spin and magnetic momentum	6
2.1.2 The motion of nuclei on the atomic level	8
2.1.3 The net magnetization vector	10
2.1.4 The dynamics of the net magnetization vecotr	10
2.1.5 Transmission of signal	13
2.1.6 Reception of signal	15
2.1.7 Pulse sequences	17
2.1.8 Image reconstruction	19
2.1.9 Hardware	20
2.1.10 Sodium MRI	22
2.2 Electromagnetic fields	24
2.2.1 Electric fields	24
2.2.2 Magnetic fields	25
2.2.3 Induction and alternating current	26

2.3	RF electronics	26
2.3.1	Passive components in RF circuits	27
2.3.2	Electric resonators	32
2.3.3	Transmission lines	36
2.3.4	The Smith Chart	37
2.3.5	Linear network analysis	38
2.3.6	The Vector Network Analyzer	39
2.4	RF coil design for MRI	39
2.4.1	Surface coils	40
2.4.2	Volume coils	40
2.5	General concepts of RF coil construction for MRI	43
2.5.1	Matching and tuning	43
2.5.2	Capacitor distribution	46
2.5.3	Quality measurement	46
2.5.4	Noise	48
2.5.5	Phantom properties	49
2.5.6	Interaction and coupling between several coil elements	49
2.5.7	Detuning circuits	49
2.5.8	Connecting coils to the MRI	50
2.5.9	Quadrature driving	50
2.6	Current knowledge	52
2.7	Thesis motivation and aim	53
3	Methods	55
3.1	3D printed coil holders	55
3.2	Magnetic field calculations	56
3.3	RF circuit simulation	57
3.3.1	Considerations for the Medical Device Regulation	57
3.4	Design 1: Single-loop coil	58
3.5	Design 2: Enhancing coil	60
3.6	Design 3: Quadrature coil	61
3.6.1	The Hybrid	62
3.7	Laboratory evaluations	64
3.8	Phantoms	65
3.9	MRI acquisition and image processing	66
3.9.1	Correction for B1 field inhomogeneities	68
3.9.2	Data analysis and evaluation	69
4	Results	71
4.1	Designs and visualizations	71
4.1.1	3D printed coil holders	71
4.1.2	Visualizations of magnetic field	71
4.2	Laboratory evaluation	78
4.2.1	Design 1: Single-loop coil	78
4.2.2	Design 2: Enhancing coil	80
4.2.3	Design 3: Quadrature coil	82

4.2.4	Prior designs	87
4.2.5	Summary of laboratory evaluations	89
4.3	MRI performance	89
4.3.1	Design 1: Single-loop coil	90
4.3.2	Design 2: Enhancing coil	90
4.3.3	Design 3: Quadrature coil	91
4.3.4	Prior designs	92
4.3.5	Correction for B1 field inhomogeneities	93
4.3.6	Comparison across coil designs	95
5	Discussion	109
6	Conclusions and Future Work	115
	Bibliography	117
	Appendices	127
A	GitHub repository	127
B	Travel report, PRESIMAL	128
C	Poster presented at the MMIV conference in December 2023	130

List of Figures

2.1	An illustration of the magnetic field of a proton	7
2.2	The precession of a spin system in a constant magnetic field	9
2.3	The precession of a spin system in a rotating reference frame	9
2.4	Relaxation, example in the brain white matter.	14
2.5	The RF pulse's influence on the net magnetization vector	16
2.6	An illustration of a wire loop in the proximity of a magnetic moment.	16
2.7	Sequence diagram for a spin-echo sequence.	18
2.8	Sequence diagram for an imaging spin-echo sequence.	19
2.9	Sequence diagram of a radial 3D cones UTE sequence	23
2.10	K-space trajectory of a radial 3D cones UTE sequence	23
2.11	Example images from sodium MRI (^{23}Na -MRI) scans.	24
2.12	Comparing square and circular loops enclosing areas of equal size	29
2.13	The current flow through a p-n junction	31
2.14	The simplest version of a perfect electric resonator.	33
2.15	A schematic representation of a series RLC circuit	33
2.16	The complex impedance of a series RLC circuit	34
2.17	A schematic representation of a parallel RLC circuit.	35
2.18	The complex impedance of a parallel RLC circuit	36
2.19	Lumped element circuit model of a transmission line.	37
2.20	An empty Smith chart.	38
2.21	Example picture of a birdcage coil	41
2.22	The magnetic field inside a birdcage coil	42
2.23	The lumped element circuit of a square loop	43
2.24	The L-shaped matching network	44
2.25	Illustration of a matching procedure for simple resonators	45
2.26	Illustration of a circularly polarized field.	51
2.27	The working principle of a 90° Hybrid.	52
2.28	The lumped element circuit for a $\lambda/8$ Hybrid	52
3.1	3D scan of a GE coil's underside imported to Fusion 360	56
3.2	Electronic schematic of the single-loop coil design.	60
3.3	Electronic schematic of the enhancing coil design.	61
3.4	Electronic schematic of the quadrature coil design.	64
3.5	Picture of the Prior Design One surface coil	65
3.6	Picture of the Prior Design Two surface coil	66
3.7	Picture of the chosen MRI phantom	67

4.1	Image of the 3D-designed enhancing coil holder	72
4.2	Image of the 3D-designed stand-alone coil holder	72
4.3	Visualization of the magnetic field around the single-loop coil	73
4.4	Visualization of the magnetic field around the enhancing coil	74
4.5	Visualization of the magnetic field around the quadrature coil	75
4.6	The circularly polarized field of the quadrature coil	76
4.7	The circularly polarized field of the birdcage and enhancing coil	77
4.8	Image of the single-loop coil	79
4.9	Plots of the single-loop coil's laboratory measurements	79
4.10	Image of the enhancing coil	81
4.11	Homemade single-loop probe	81
4.12	Plots of the enhancing coil's laboratory measurements	82
4.13	Image of the quadrature coil	83
4.14	Plot of the quadrature coil's unloaded S-parameter measurements	84
4.15	Plot of the quadrature coil's loaded S-parameter measurements	84
4.16	Smith plot of the quadrature coil's S-parameter measurements	85
4.17	S-parameter magnitude plots from the Hybrid	86
4.18	Plots of the Prior Design One's laboratory measurements	88
4.19	Plots of the Prior Design Two's laboratory measurements	88
4.20	Single-loop MRI, phantom images	90
4.21	Birdcage MRI, phantom images	91
4.22	Enhancing coil MRI, phantom images	92
4.23	Quadrature coil MRI, phantom images	93
4.24	Prior Design One MRI, phantom images	94
4.25	Prior Design Two MRI, phantom images	95
4.26	Blurred B1 correction for Prior Design One	96
4.27	Blurred B1 correction for Prior Design Two	96
4.28	Blurred B1 correction example for the single-loop coil	97
4.29	Blurred B1 correction for the quadrature coil	97
4.30	Blurred B1 correction for the birdcage coil	98
4.31	Blurred B1 correction for the enhanced birdcage coil	98
4.32	B1 field map correction for the quadrature coil	99
4.33	B1 field map correction for the enhanced birdcage coil	100
4.34	SNR values calculated from phantom images for all coils.	101
4.35	Signal intensity comparison, vertical line plot of the CN-197 scans . . .	102
4.36	Signal intensity comparison, vertical line plot of the CN-1442 scans . .	103
4.37	Signal intensity comparison, vertical line plot of the CN-2552 scans . .	104
4.38	Signal intensity comparison, horizontal line plot of the CN-197 scans .	105
4.39	Signal intensity comparison, horizontal line plot of the CN-1442 scans .	106
4.40	Signal intensity comparison, horizontal line plot of the CN-2552 scans .	107
1	Picture of a famous neighborhood in Tübingen, Germany.	129
2	Poster for the MMIV conference	131

List of Tables

2.1	Physical constants with their symbols and values [42].	6
2.2	Details on nuclei in the human body available for MRI examination . . .	8
2.3	List of magnetic susceptibility values for selected materials	21
2.4	Overview of relevant passive components used in RF circuits	32
3.1	Overview of MRI pulse sequence scanning parameters used in this thesis.	67
4.1	Components used for the single-loop coil	78
4.2	Components used for the enhancing coil	80
4.3	Components used for the quadrature coil	83
4.4	S-parameter measurements of the Hybrid	87
4.5	Laboratory evaluation of all coils	89

Chapter 1

Introduction

Conventional clinical Magnetic Resonance Imaging (MRI) scans produce detailed three-dimensional image volumes of internal organs and structures of the human body [1]. This visualization is made by interactions between magnetic fields and hydrogen atoms' spins in the body. The development of this intricate technique spanned many years. The discovery of the spin angular momentum of electrons was an essential observation by Stern and Gerlach after their experiments with silver atoms in 1920 [2]. Rabi and his group described how a constant magnetic field applied to a sample gives the spins in the sample a precessional motion around the field direction [3]. By extending quantum mechanical concepts around this, Bloch and Purcell measured the precession of proton spins in 1946 [4, 5]. The previous work led to the first Nuclear Magnetic Resonance (NMR) scan of a water sample performed by Paul Lauterbur in 1973 [6]. Lauterbur used a second field to make several one-dimensional projections of a phantom and reconstruct them into a two-dimensional (2D) image. In 1977, Peter Mansfield and his group became the first to perform medical imaging by NMR [7], later called MRI.

The transmission and reception of signal in an MRI experiment is performed by Radio Frequency (RF) pulses produced by antennas, which in MRI are called RF coils [1]. The most straightforward design is a single wire formed into a circle. Applying Alternating Current (AC) with the same frequency as the hydrogen spin system to this simple RF coil produces an RF field through Faraday's law of induction [8, 9]. When the RF field is applied orthogonally to the constant magnetic field, the RF field will flip the precessing spins away from equilibrium, exciting them [10]. The excited spin system will return to equilibrium immediately if the RF field is switched off. During this return, a current is induced in the RF coil, which can be measured and interpreted by the MRI system [11].

Hydrogen has superior MRI sensitivity because of its ideal magnetic properties and vast abundance in the human body [1]. However, other essential nuclei in human physiology can also be detected. Imaging other nuclei than hydrogen, for example, sodium (^{23}Na), is called non-proton, X-nuclei, or multinuclear MRI. The first sodium MRI (^{23}Na -MRI) scan of a human was performed by Hilal et al. in 1980 [12].

1.1 Motivation

Examination of ^{23}Na concentration is particularly interesting for studies of brain function, but also for the musculoskeletal system, cartilage, and other organs like the heart and kidneys [13, 14]. The propagation of neuronal signals in and between neurons in the human brain depends on ^{23}Na [15]. ^{23}Na and potassium (^{19}K) act like electrolytes in a battery by exchanging ions across the cell membrane to create a potential difference, exciting a small part of the membrane [16]. A nerve impulse can be described as a traveling wave of excitation and is produced by momentary openings of voltage-gated $^{23}\text{Na}^+$ channels cascading down the cell membrane. After influx, the $^{23}\text{Na}^+$ is pumped out of the cell again through the $^{23}\text{Na}^+/\text{K}^+$ pump, leaving the cell membrane unexcited [16].

Currently, the Blood Oxygenation Level Dependant contrast (BOLD) method, first described by Ogawa et al. in 1990 [17], is the most used method for brain activity measurement [18]. However, ^{23}Na -MRI combined with ^1H -MRI could provide a more direct brain activity measurement [19] and be a biomarker for diagnosing and monitoring neurologic diseases like brain tumors, Multiple Sclerosis (MS), and Alzheimer's disease [20, 21]. Many studies have evaluated the Tissue total Sodium Concentration (TSC) in acquired voxels, and some have attempted to measure the temporal change of TSC using dynamically repeated ^{23}Na -MRI [22, 23]. Several challenges with measuring TSC are pointed out in these studies, among them the low spatial resolution and Signal to Noise Ratio (SNR) of ^{23}Na -MRI images, the long acquisition time, and the lack of an exact microbiological explanation for the calculated values in the acquired voxels. ^{23}Na -MRI have intrinsically low SNR because of the lower gyromagnetic ratio, lower ^{23}Na concentrations in vivo, and lower relaxation times than for hydrogen imaging [24].

1.2 Recent developments and Contribution

^{23}Na -MRI has gained interest over the past two decades because of the increasing availability of high (3T) and ultra-high fields (7T) in MRI, more advanced scanner hardware, and improved acquisition methods [14, 25]. Transmission and Reception of multinuclear signals require additional equipment. Some clinical MRI systems can be delivered with a broadband RF amplifier to transmit signal in multinuclear imaging [26, 25]. Frequency conversion on proton-only scanners has also been demonstrated [27]. RF coils are usually constructed in-house, and the designs are still in development [26]. Transmit coils should provide strong RF fields to shorten the time required for flipping the spins and good homogeneity over the imaged volume [28]. Receive coils should also provide good homogeneity, but the most critical parameter is a high SNR.

Dual-tuned coils allow proper co-registration of ^1H -MRI and multinuclear MRI [29]. The physiological information available to ^{23}Na -MRI needs the anatomical information available to ^1H -MRI. Most clinical MRI scanners have a body coil within the scanner bore, which can provide relatively low resolution ^1H -MRI images for ref-

erence [30]. However, dually tuned coils usually provide a higher 1H -SNR, which can be traded in for a higher resolution of 1H -MRI, even if the ^{23}Na -SNR is prioritized [29]. Dual tuning is challenging because the coil elements must be placed close together, increasing the likelihood of electromagnetic interactions [26]. Many challenges have been overcome, and dual-tuned array coils are a reality. Some designs even allow interleaved 1H and ^{23}Na imaging. At high fields, the increased SNR is accompanied by more challenges because of shorter RF wavelengths, leading to inhomogeneities in the magnetic fields and reduced SNR, making it harder to design good RF coils at 7T [31]. However, many of these challenges have been overcome [13], and a dual-tuned 32-element array allowing interleaved 1H and ^{23}Na imaging at 7T was realized by Wilferth et al. in 2022 [32].

At 3T, the achievable SNR is limited [26]. Some researchers might argue that the low SNR of ^{23}Na -MRI makes studies in 3T scanners less feasible. However, there are many possible applications of ^{23}Na -MRI at 3T [33, 22] and several approaches to maximize SNR [34]. One approach to increase SNR in a particular Region of Interest (ROI) is to fit the coil wires to only cover the specific ROI [28]. A further improvement in SNR is achievable by creating circularly polarized magnetic fields instead of linearly polarized fields, which quadrature driving of two coil elements can realize [35]. Birdcage coils usually produce circularly polarized magnetic fields, but the designs prefer field homogeneity, offering lower SNR compared to surface coils [36]. Smaller secondary resonator coils magnetically coupled to larger volume coils can improve sensitivity in small volumes [37, 38].

1.3 Problem Statement and thesis outline

Maximizing the MRI sensitivity is essential to unlocking the full potential of studies involving ^{23}Na -MRI at 3T [22, 13]. This master's project aims to create various surface coils specialized for an increased SNR of ^{23}Na -MRI in the visual cortex, found just inside the cranial bone in the back of the human head. The improvement will be discussed relative to two general-purpose surface coils and a 16-rod birdcage coil from RAPID Biomedical.

Three different coil designs will be developed and tested.

- The single loop coil - A single loop of wires, the simplest surface coil geometrically shaped to fit the ROI.
- The enhancing coil - A secondary resonator loop that enhances the magnetic field of a 16-rod birdcage coil in the ROI.
- The quadrature coil - Two wire loops operated in quadrature to create a circularly polarized magnetic field in the ROI.

The in-house developed coils will be tested and compared to other coils through laboratory measurements and MRI phantom images.

Chapter 2

Theory

2.1 MRI

MRI is a widely used imaging method within the medical field. Since its first application, MRI has become a powerful tool in clinical settings and research [1]. Compared with X-ray and Computed Tomography (CT) imaging, which both expose the patient to ionizing radiation, MRI is less harmful and provides different information in the images [39]. X-ray is a 2D footprint of intensity loss due to electron density in the body, and CT combines several X-ray examinations into a volume of grey scale values indicating how much of the radiation was attenuated in the specific voxel. X-ray and CT have several advantages, such as excellent bone contrast and short examination time. MRI requires considerably more time but provides substantially more detailed contrast between different soft tissues in the human body. In research, other measurements are also made from MRI, but few have been included in clinical practice [1]. All three image modalities are crucial for discovering anatomical abnormalities.

Image modalities like Positron Emission Tomography (PET) or Single Photon Emission Computed Tomography (SPECT) measure the biochemical distribution of radiotracers. In both examinations, a radioactive pharmaceutical is injected into the patient's bloodstream to partake in the body's physiological processes. By capturing the radiation produced by the radioactive substances, the pharmaceutical can be traced spatially and show where the body uses it. To provide an anatomical map, the radiation detectors are combined with a CT or MRI machine so that the two examinations can be done while the patient remains in the same position. Such examinations are expensive, and the pharmaceuticals are short-lived and require extra caution during production and use because of the radiation. The examinations give essential info, but they are only done when required because of the radiation exposure.

No ionizing radiation is involved in MRI and ultrasound. Ultrasound uses sound waves with frequencies above the human hearing range to examine tissue properties. MRI examine the different tissues of the human body based on their electromagnetic properties. MRI has enormous potential for studying physiological functions, and much

research goes into finding new ways to apply the technology, for example, in studies of the brain [40]. Ultrasound cannot provide information on the brain because the skull bone entirely absorbs the sound waves.

Explanations of MRI often start with the atom. Previously, it was considered the smallest building block of the physical world, but this turned out to be untrue as the atom consists of protons and neutrons whose interactions explain the properties of the atom [41]. One of these properties is the magnetic moment or spin. MRI scans of humans manipulate the accumulated magnetic moments in tissue through static magnetic fields and oscillating RF-pulses to generate electromagnetic signals from the atoms in the body [1]. From these electromagnetic signals, images of human tissue are reconstructed, containing information on the concentration and motional freedom of the specific atom type targeted by the MRI.

The following section presents the basic principles of MRI, some of its major hardware components, and the hardware differences for imaging different nuclei.

Table 2.1: *Physical constants with their symbols and values [42].*

Name	Symbol	Value
The reduced Planck constant	\hbar	$\frac{6.62607 \cdot 10^{-34}}{2\pi} = 1.05457 \cdot 10^{-34} m^2 kg/s$
Boltzmann's constant	k	$1.38065 \cdot 10^{-23} J/K$
Reduced gyromagnetic ratio	γ	$\frac{\gamma'}{2\pi}$
Vacuum permittivity	ϵ_{p0}	$8.85419 \cdot 10^{-12} F/m$
Vacuum permeability	μ_{p0}	$4\pi \cdot 10^{-7} H/m$

2.1.1 Spin and magnetic momentum

Spin and magnetic momentum are properties of an atom. In quantum mechanics, every particle is assigned four quantum numbers to describe its position and energy [43]. One of these is the spin quantum number (s) related to the intrinsic angular momentum (J), which is proportional to the magnetic moment ($\vec{\mu}$) [44]. A single proton (1H) generates a weak magnetic field around it because of its inherent intrinsic angular momentum, similar to the result of a circulating electric current. Figure 2.1 illustrates the field around a proton using field lines, indicating direction by arrows and intensity by their spacing. Experiments have shown that the z-component of the intrinsic angular momentum aligned with a magnetic field directed along the z-axis is related to the reduced Planck constant (\hbar) by equation 2.1 [44]. The value of \hbar is given in Table 2.1.

The magnetic quantum number (m_j) can take $m_j = -j, -j + 1, \dots, j - 1, j$ different values, where j is an integer value or a half-integer value related to the intrinsic angular momentum [44]. The range of possible intrinsic angular momentum values is not continuous but discretized and can only take on a certain set of values. The intrinsic angular momentum (J) is a sum of the orbital motion (\vec{L}) and the intrinsic spin (\vec{S}), like equation 2.2 shows. By equation 2.1, these two quantities are analogous to the intrinsic angular momentum, but with new quantum numbers called m_l and

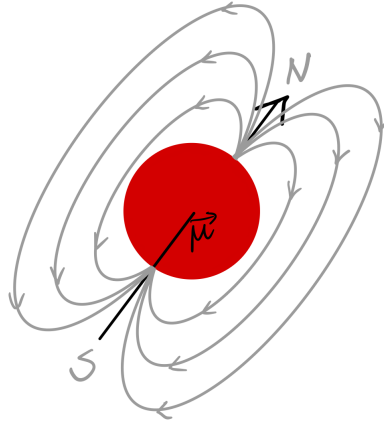


Figure 2.1: An illustration of the magnetic field of a proton – A proton with its magnetic field due to its magnetic moment ($\vec{\mu}$).

m_s , respectively. $m_l = -l, -l + 1, \dots, l - 1, l$, and l can only be integer values, while $m_s = -s, -s + 1, \dots, s - 1, s$ and s can be either integer or half-integer values like j . For an MRI experiment to work, i.e., transmit and receive signal to and from a sample, the investigated atoms must have a non-zero magnetic moment.

$$J_z = \vec{m}_j \cdot \hbar \quad (2.1)$$

$$\vec{J} = \vec{L} + \vec{S} = \vec{m}_l \cdot \hbar + \vec{m}_s \cdot \hbar \quad (2.2)$$

The magnetic moment is measured from experiments and is proportional to J by the proportionality constant called the gyromagnetic ratio (γ), see equation 2.3 [44]. The discrete nature of the J makes $\vec{\mu}$ a discrete quantity. The gyromagnetic ratio used in this thesis is the reduced one presented in Table 2.1.

$$\vec{\mu} = \gamma \cdot \vec{J} \quad (2.3)$$

An atom's atomic number (Z) tells the number of protons in the nucleus [43]. Atomic nuclei also contain neutrons to counteract the repelling forces between the protons when several protons are present. The collective term for protons and neutrons is nucleons. Every proton contributes with its spin unless it is paired with a second proton, which counteracts the spin of the first proton, resulting in a neutralized proton pair containing two protons in the two possible spin quantum states, so their spin and orbital motion cancel. Neutrons also pair up similarly. The nucleon pairs stack up in the center of the nucleus, and only unpaired nucleons in the outer shell contribute to the nucleus's total intrinsic angular momentum [45].

A nucleus with an even number of protons and an even number of neutrons will have zero intrinsic angular momentum and by equation 2.3 also a zero magnetic moment. When either the number of protons, the number of neutrons, or both numbers are odd, the magnetic moment of the nucleus is non-zero, and a gyromagnetic ratio can be

determined [45]. Hence, a non-zero spin quantum number (s) is required for a non-zero gyromagnetic ratio, which results in a non-zero magnetic moment, making the nucleus detectable in an MRI experiment. The magnetic moment is measured in nuclear magneton, μ_n , defined by the following physical quantity: $\mu_n = \frac{eh}{4\pi m_e} \approx 5.05 \times 10^{-27} \text{ A} \cdot \text{m}^2$. Unpaired protons lead to positive gyromagnetic ratios, and unpaired neutrons lead to negative gyromagnetic ratios. An overview of some MRI detectable nuclei present in the human body is given in Table 2.2 [45].

Table 2.2: *Details on nuclei in the human body available for MRI examination* – Spin quantum number, magnetic moment and gyromagnetic ratio of MRI detectible nuclei in the human body [14, 45]. The sodium concentrations in the brain's Grey Matter (GM) and White Matter (WM) are specified.

Nucleus	Spin, s	$\vec{\mu}$ [μ_n]	γ [MHz/T]	Concentration in human body
Hydrogen, 1H	1/2	2.7928	42.58	88 M
Sodium, ^{23}Na	3/2	2.2175	11.27	80 mM (mean) 20-60 mM (WM) 30-70 mM (GM)
Phosphorus, ^{31}P	1/2	1.136	17.25	75 mM

2.1.2 The motion of nuclei on the atomic level

If a general system of identical atoms with nonzero magnetic moment experience a nonzero total torque ($\vec{\tau}$), it will have a total magnetic moment changing according to equation 2.4. A torque is a force that twists or turns an object to cause a rotation around an axis. Such a torque may be applied to the magnetic moment by an external magnetic field (B). The total experienced torque in this situation will depend on the magnetic moment of the atom and the flux density of the external magnetic field following equation 2.5 [45]. Magnetic flux can be explained as the number of field lines passing through an area.

$$\frac{d\vec{\mu}}{dt} = \gamma \vec{\tau} \quad (2.4)$$

$$\vec{\tau} = \vec{\mu} \times \vec{B} \quad (2.5)$$

By combining equation 2.4 with equation 2.5, the resulting differential equation (Eq. 2.6) shows how the magnetic moment changes with time [45].

$$\frac{d\vec{\mu}}{dt} = \gamma' \vec{\mu} \times \vec{B} \quad (2.6)$$

$$\omega_0 = 2\pi f_0 = \gamma \cdot B_0 \quad (2.7)$$

The solution to equation 2.6 reveals a precessional motion of the magnetic moment crucial to the MRI application [45]. The frequency of this motion, f_0 , is found

from this equation and expressed by a separate equation called the Larmor equation 2.7. A drawing of the precessional motion is shown in Figure 2.2 where the externally applied magnetic field is directed along the z -axis. The figure also illustrates the angular frequency $\omega_0 = 2\pi f_0$ and the angle α between the $\vec{\mu}$ and the field direction, i.e., the z -axis. In this situation, the magnetic moment is aligned with the magnetic field because the precessional motion in $x - y$ -direction cancels out over time, leaving the z -directional component of the magnetic moment.

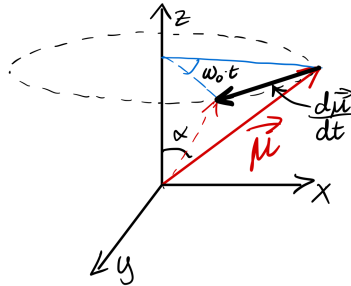


Figure 2.2: *The precession of a spin system in a constant magnetic field* – The precession of a spin system's magnetic moment about the directional axis of a constant magnetic field. The angular motion is negative.

The constant precession of the magnetic moments makes it hard to picture the exact workings of an MRI experiment. It is easier to picture in a rotating coordinate system, which is essentially the same x, y , and z components as drawn in Figure 2.2 rotating about the z -axis with the same frequency as the magnetic moment. In the rotating reference system, the directional components are denoted with a prime, x' , y' , and z' , and the magnetic moment looks like Figure 2.3.

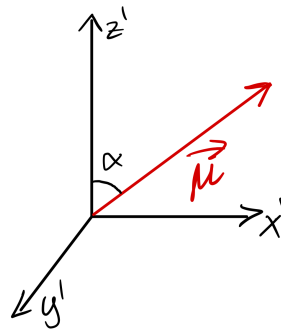


Figure 2.3: *The precession of a spin system in a rotating reference frame* – The precession of a spin system's magnetic moment about the directional axis of a constant magnetic field. Presented in a rotating coordinate system with x' , y' , and z' rotating about the z -axis with an angular frequency equal to the spin system's precession frequency.

The energy of a proton in the presence of an external magnetic field can be determined by equation 2.8 [44], which use equations 2.1 and 2.3, resulting in discrete energy levels. Hydrogen has $s = \frac{1}{2}$ which results in $m_s = -\frac{1}{2}, +\frac{1}{2}$. The spin quantum number, combined with equation 2.8, concludes that hydrogen has two possible energy states. The quantization of energy levels was observed in the Stern-Gerlach experiment [43, 2]. The most favorable of these is when $m_s = +\frac{1}{2}$ and $E_{\uparrow} = \frac{-1}{2}\gamma\hbar B_z$, see equation 2.9 [44].

$$E = -\vec{\mu} \cdot \vec{B} = -\mu_z B_z = -\gamma m_s \hbar B_z \quad (2.8)$$

$$m_s = +\frac{1}{2} \Rightarrow E_{\uparrow} = -\frac{1}{2} \gamma \hbar B_z, \text{ and } m_s = -\frac{1}{2} \Rightarrow E_{\downarrow} = +\frac{1}{2} \gamma \hbar B_z \quad (2.9)$$

If a proton transitions between the two energy states, E_{\downarrow} and E_{\uparrow} , an RF photon with energy equal to the energy difference will be involved. This difference is $\Delta E = \frac{1}{2} \gamma \hbar B_0 - (-\frac{1}{2} \gamma \hbar B_0) = \hbar \gamma B_0$. The quantum energy is absorbed or emitted as a photon with a frequency equal to the Larmor precession frequency found from the Larmor equation (Eq. 2.7).

2.1.3 The net magnetization vector

A small volume, f.ex., $V = (1 \times 1 \times 1) \text{mm}^3$, called a 1mm^3 voxel, contains millions of nuclei. If the volume contains water and experiences a homogeneous magnetic field, many hydrogen atoms will align with the field direction because of their magnetic moment. Figure 2.2 shows the alignment that requires the least energy and the other points in the opposite direction along the z-axis [10]. The first energy state can be referred to as parallel and the other as antiparallel to the z-axis. The two different states pair up, and the total magnetic moment of such a pair will be zero. The MRI experiment depends on an unbalance between the energy states. Fortunately, the most favorable energy state, E_{\uparrow} in equation 2.9, is the majority. All the individual magnetic moments of the 1mm^3 voxel or any other small volume can be summed together through the principle of superposition. The resulting vector-sum divided by the volume V is called the net magnetization vector (\vec{M}), see equation 2.10, where N_s is the total number of spins in the volume.

$$\vec{M} = \frac{1}{V} \sum_{n=1}^{N_s} \vec{\mu}_n \quad (2.10)$$

The net magnetization vector of an atom type present in the human tissue is manipulated through an MRI experiment and provides a signal that can be processed and interpreted as an MRI image. Over the example volume of a 1mm^3 voxel, the external fields are to a good approximation uniform over the entire volume, simultaneously as the volume contains enough protons to make a signal strong enough for an MRI experiment [10].

2.1.4 The dynamics of the net magnetization vector

In MRI, the main magnetic field is usually denoted B_0 . The protons in a 1mm^3 voxel interact with the environment, but to simplify the explanation, this is ignored. With that simplification, the motion of the \vec{M} can be described like the motion of a single

$\vec{\mu}$ resulting in equation 2.11, named the Bloch equation, where \vec{B}_{ext} refers to the total external magnetic field experienced by the $1mm^3$ voxel [10].

$$\frac{d\vec{M}}{dt} = \gamma\vec{M} \times \vec{B}_{ext} \quad (2.11)$$

For the analysis of the net magnetization vector's dynamics, it is convenient to decompose the vector into a parallel component M_{\parallel} and a perpendicular component \vec{M}_{\perp} relative to the magnetic field. The cross product with B_0 in equation 2.11 is expressed by the decomposed vectors in equations 2.12 and 2.13. When considering interactions with the molecular environment, they will include additional terms [10].

$$M_{\parallel} = M_z, \quad \frac{dM_{\parallel}}{dt} = 0 \quad (2.12)$$

$$M_{\perp} = M_x\hat{x} + M_y\hat{y}, \quad \frac{d\vec{M}_{\perp}}{dt} = \gamma\vec{M}_{\perp} \times \vec{B}_{ext} \quad (2.13)$$

A formula for the potential energy of a \vec{M} experiencing a magnetic field B_0 is presented in equation 2.14 [10]. The minimum potential energy involves only the parallel magnetization because the transverse or perpendicular component of the magnetization vanishes as the magnetization returns to the equilibrium state. Pierre Curie showed the equilibrium potential energy dependence of temperature T , magnetic flux density B_0 , and a constant C_c , see equations 2.15 and 2.16 [10].

$$U_M = -\vec{M} \cdot \vec{B} = -M_{\parallel}B_0 \quad (2.14)$$

$$M_0 = C_c \frac{B_0}{T} \quad (2.15)$$

$$C_c = \rho_0 \frac{s(s+1)\gamma^2\hbar^2}{3k} \quad (2.16)$$

The constant C_c in Curie's law (2.15) can be determined through the expression in equation 2.16, where ρ_0 is the density of spins per volume and k is Boltzmann's constant. This calculation for C_c is only approximate and requires $\hbar\omega_0 \ll kT$, which is a typical condition for MRI experiments [46]. The C_c defines how many excess spins are in the favorable energy state, i.e., aligned with the field, compared to how many are reverse aligned with the field B_0 . At room temperature, the proton energy is minimal compared to the thermal energy, and the lowest energy level is weakly favorable. If M_0 were to be calculated more accurately, the statistical mechanics of distinguishable particles must be included [47]. Then, the Boltzmann distribution, $n_i = Ae^{-\frac{\epsilon_i}{kT}}$, gives the number of particles in each energy state and the difference between the numbers of

particles in each state can be calculated precisely.

The equilibrium can be disturbed by transferring energy to the system, rotating the net magnetization vector away from its equilibrium position. After the disturbance, when only the main magnetic field is left, the net magnetization vector will try to return to equilibrium.

Spin-lattice interaction

The longitudinal component of the net magnetization vector will return to the equilibrium magnitude through spin-lattice interaction [10]. Lattice refers to the structure of atoms and molecules nearby, and their interactions with the spins are thermal. The amount of interaction is higher when the system is far from the equilibrium state M_0 . The interaction increase is proportional to this difference with the inverse proportionality constant called spin-lattice relaxation time (T_1), see equation 2.17 which replaces equation 2.12 when $|\vec{M}| \neq M_0$ in the presence of a magnetic field.

$$\frac{dM_{\parallel}}{dt} = \frac{1}{T_1}(M_0 - M_{\parallel}) \quad (2.17)$$

The spin-lattice relaxation time describes the time scale for regrowth of the parallel component and ranges from milliseconds to seconds between different tissues. It also depends on the main magnetic field flux density (B_0), temperature T [10], and type of nucleus.

Spin-spin interaction

The transverse component of the net magnetization vector will seek to return to zero through spin-spin interactions, meaning interactions with the magnetic fields of other spins nearby [10]. Each proton's experienced field is slightly different, resulting in different precession frequencies. First, when \vec{M} is rotated away from its equilibrium, all the individual $\vec{\mu}$ s are in phase. Over time, the different experienced fields make them de-phase after only a few rotations, resulting in the total transverse component of the \vec{M} canceling out. The reduction rate is related to the transverse component through an inverse proportionality constant called spin-spin relaxation time (T_2). The inverse component adds a decay rate term to the differential equation in equation 2.13, resulting in equation 2.18. It is worth mentioning that the observed T_2 is shorter than the theoretical one because of local, random, time-dependent field inhomogeneities in the MRI.

$$\frac{d\vec{M}_{\perp}}{dt} = (\gamma\vec{M}_{\perp} \times \vec{B}_{ext}) - \frac{1}{T_2}(\vec{M}_{\perp}) \quad (2.18)$$

The Bloch equations

The modified Bloch equation (2.19) describes the total motion of the net magnetization vector in a magnetic field after being pushed away from its equilibrium state. With the introduced proportionality constants T_1 and T_2 , a time-dependent solution to this equation predicts the image contrast from an imaging sequence [10].

$$\frac{d\vec{M}}{dt} = \gamma\vec{M} \times \vec{B}_{ext} + \frac{1}{T_1}(M_0 - M_z)\hat{z} - \frac{1}{T_2}\vec{M}_{\perp} \quad (2.19)$$

The modified Bloch equation is a differential equation, and the solution can be formulated by two equations, one describing the parallel component and another describing the perpendicular component. Together, they describe the motion in all three spatial directions x , y , and z , see equation 2.20 [10], where t_0 refers to the time after the disturbance.

$$\begin{aligned} M_{\parallel}(t) &= M_{\parallel}(t_0)e^{-(t-t_0)/T_1} + M_0(1 - e^{-(t-t_0)/T_1}) & \left(\vec{B}_{ext} \parallel \hat{z} \right) \\ M_{\perp}(t) &= M_{\perp}(0)e^{-(t-t_0)/T_2} & \left(\vec{B}_{ext} \parallel \hat{z} \right) \end{aligned} \quad (2.20)$$

The process where the magnetization vector returns to its equilibrium position is called relaxation. The equations in equation 2.20 describe this mathematically, and by inserting values for T_1 , T_2 , and M_0 curves like the ones in Figure 2.4 can be plotted. The values applied here were measured in the brain's white matter [48]. The equilibrium or steady state solution for these equations can be found from the asymptotic limit $t \rightarrow \infty$, which yields $M_{\parallel}(\infty) = M_0$ and $M_{\perp} = 0$.

2.1.5 Transmission of signal

To rotate the net magnetization vector away from the equilibrium position requires energy. Energy is transmitted to the spin system using an RF-field, also called an RF pulse (B_1), because it is only active for a short time. An RF-pulse is an oscillating magnetic field and can be either linearly polarized or circularly polarized [49].

A linearly polarized RF-pulse can be described as a cosine wave propagating along the x -axis in a still coordinate system, mathematically expressed in equation 2.21 using unit vector \hat{x} [49]. If the frequency of the cosine wave is the same as the precession frequency of the nucleus, there is always a component of the field contributing to rotating the net magnetization vector down towards the $x - y$ -plane. In a rotating coordinate system, with unit vectors \hat{x}' and \hat{y}' , the same RF-pulse can be expressed by equation 2.22. This equation reveals a constant term and two oscillating terms. $\langle \vec{B}_{1,rot}^{lin} \rangle$ is the average signal over an infinite number of periods. The working component of the RF-pulse in the rotating coordinate system is equal to that shown in equation 2.23 because the oscillating terms cancel out. The effect is valid for the limited activation of an RF-pulse as long as the active time is long compared to the cosine period. Only half of the original amplitude b_1^{lin} works on rotating the net magnetization vector out

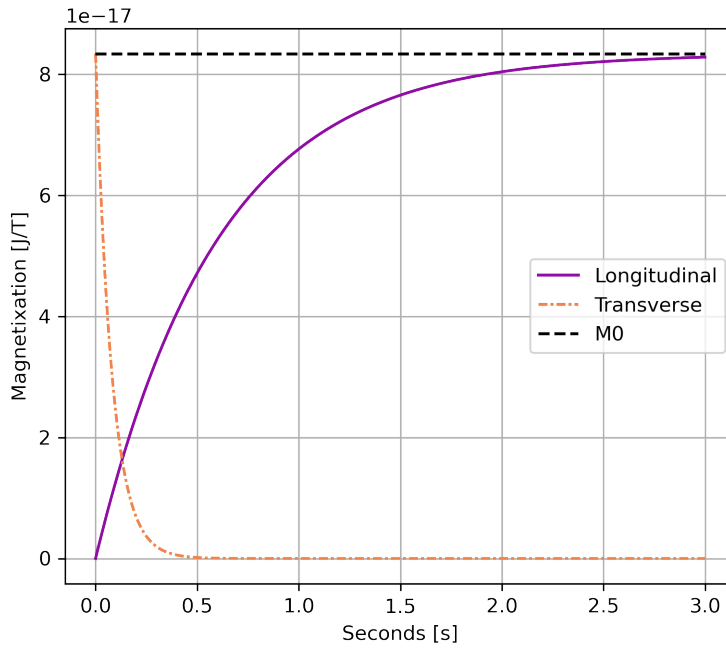


Figure 2.4: *Relaxation, example in the brain white matter.* – The Bloch equations were used to show the longitudinal recovery and the transverse fall-off as the magnetization vector returns to equilibrium. The applied values were measured in the brain’s white matter [48].

of its equilibrium, while the other half generates heat. A linearly polarized field can be decomposed into two rotating vectors with y-components opposite in magnitude and x-components half the original magnitude. With this decomposition, one rotating component will rotate with the precession and contribute to flipping the net magnetization vector. The other component will rotate in the opposite direction and be ineffective, i.e., generate heat.

$$\vec{B}_1^{lin} = b_1^{lin} \cos(\omega t) \hat{x} \quad (2.21)$$

$$\overrightarrow{B}_{1,rot}^{lin} = \frac{1}{2} b_1^{lin} [\hat{x}' (1 + \cos(2\omega t)) + \hat{y}' \sin(2\omega t)] \quad (2.22)$$

$$\langle \overrightarrow{B}_{1,rot}^{lin} \rangle = \frac{1}{2} b_1^{lin} \hat{x}' \quad (2.23)$$

A more efficient RF pulse would transfer all of its power to the net magnetization vector of the sample using a circularly polarized field rotating with the direction of the precessional motion of the spins [44]. Such a field can be produced by exploiting the fact that two RF pulses applied simultaneously will work together by the principle of superposition. Two linearly polarized fields with the same Larmor frequency and peak amplitude b_1^{lin} , but applied in such a way that their field lines are perpendicular with AC current supply 90° out of phase, will produce a circularly polarized RF pulse,

\vec{B}_1^{circ} [50]. Equation 2.24 expresses this mathematically for a still coordinate system. The 90° phase shift has associated the word 'quadrature' with this setup. In a rotating coordinate system, the circularly polarized field can be expressed by equation 2.25 [49]. The maximum amplitude b_1^{circ} of the two applied fields in the non-rotating reference frame is constantly available for spin flipping in the rotating coordinate system. With the circularly polarized RF pulse, less power is required to perform a given spin flip than with a linearly polarized RF pulse because there is no factor of one half in front of equation 2.22 [49].

$$\vec{B}_1^{circ} = b_1^{circ}(\hat{x}\cos(\omega t) - \hat{y}\sin(\omega t)) \quad (2.24)$$

$$\vec{B}_{1,rot}^{circ} = b_1^{circ}\hat{x}' \quad (2.25)$$

The applied RF pulse works together with the main magnetic field B_0 , and their superposition is expressed in equation 2.26 [10]. The effective field depends on the frequency of the circularly polarized magnetic field ω_1 , the spin-precession frequency ω_0 , and the rotational frequency of the reference frame. The dynamics of the net magnetization vector in the rotating reference frame resulting from the field is expressed in equation 2.27 and Figure 2.5 illustrates this motion in both the still and the rotating reference frame.

$$\vec{B}_{ext} = B_0\hat{z}' + B_1\hat{x}' \quad (2.26)$$

$$\left(\frac{d\vec{M}}{dt}\right)' = \vec{M} \times [\hat{z}'(\omega_0 - \omega) + \hat{x}'\omega_1] \quad (2.27)$$

If the frequency of the reference frame ω is equal to ω_0 , there is no contribution from the main magnetic field flux density to the torque, and it is purely parallel with the x' -axis because of the applied B_1 -field [10]. The requirement of equal frequencies puts the word 'resonance' in MRI and NMR because the spin only flips when the on-resonance condition (2.28) is fulfilled. Equation 2.27 also applies to the linearly polarized field, which can be decomposed into two rotating fields where only one is effective.

$$\omega = \omega_0 \quad (2.28)$$

2.1.6 Reception of signal

A net magnetization vector in the transverse plane will align with the main magnetic field. The force of the main magnetic field pulls the net magnetization vector back into the equilibrium position in a motion opposite to the one illustrated in Figure 2.5 when

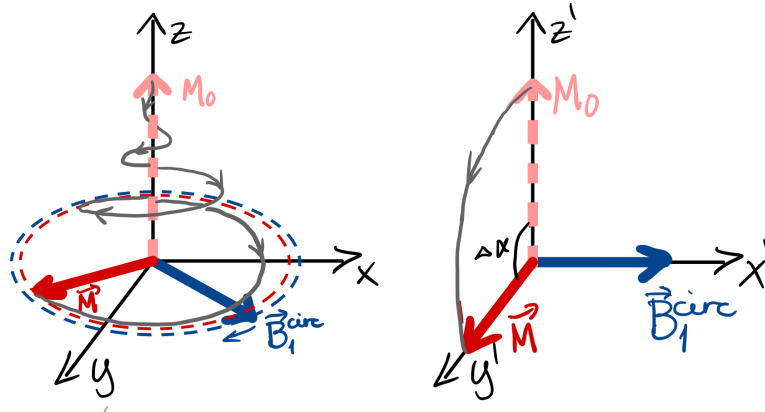


Figure 2.5: *The RF pulse's influence on the net magnetization vector* – An illustration of the net magnetization vector's dynamics when an RF pulse parallel with the rotating x-axis (x') is applied long enough to result in a flip angle of 90° . The left illustration is with a still coordinate system, while the coordinate system to the right rotates with the resonance frequency of the spin systems.

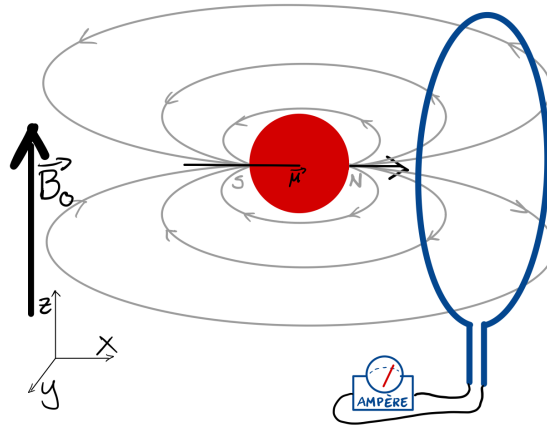


Figure 2.6: *An illustration of a wire loop in the proximity of a magnetic moment.*

the RF pulse is turned off [11].

The net magnetization vector produces an RF pulse as it returns to equilibrium. Changing fields can be detected by a circle of conducting wire, according to Faraday's law of induction (Eq. 2.29) [11, 9]. Faraday stated that an electromotive force (ε), or emf, is induced in any conducting wire loop experiencing a changing magnetic flux (Φ_B) through its loop area [8]. The area enclosed by the wire loop is represented by its normal vector \vec{A} in equation 2.29, and the vector field by \vec{B} .

$$\varepsilon = -\frac{d}{dt}(\Phi_B) = -\frac{d}{dt} \int_A \vec{B} \cdot d\vec{A} \quad (2.29)$$

A wire loop like the one drawn in Figure 2.6 can also be called a surface coil. A coil close to a precessing magnetic moment experiences a changing magnetic flux. Notice the magnetic field lines in Figure 2.6. By Faraday's law (Eq. 2.29), the changing flux induces an emf in the coil. The induced emf produces a current in the coil, creating a

magnetic field opposing the changes induced by the external field [11], i.e., the rotating net magnetization vector. The field lines running through the coil change direction periodically, inducing AC in the coil. The induced AC will have a decreasing voltage magnitude similar to the transverse component in Figure 2.4. The amplitude of the RF signal is low, even at the start of the decay, and the amplitude of a rapidly oscillating signal is challenging to detect, so the receiving equipment needs to amplify the signal significantly [11].

2.1.7 Pulse sequences

In MRI, a pulse sequence describes when the excitation, localization, and data acquisition of data occur in a scan [51]. The RF pulse is a critical component in sequence design. The length of application (t_α) is directly proportional to the flip angle ($\Delta\alpha$), i.e., the total angle between the \vec{M} and the z -axis after the RF pulse. With the on-resonance condition (2.28) in place, the motion of the net magnetization vector inflicted by a circularly polarized RF-pulse can be described by equation 2.30. The flip angle can be calculated by equation 2.31 [49].

$$\left(\frac{d\vec{M}}{dt}\right)' = \vec{M} \times \hat{x}'\omega_1 \quad (2.30)$$

$$\Delta\alpha = \gamma B_1 t_\alpha = \omega_1 t_\alpha \quad (2.31)$$

The importance of the resonance-condition (2.28) is evident when comparing equation 2.27 and 2.30, keeping in mind that B_0 is several orders of magnitude greater than B_1 . At resonance, an RF-pulse of weak amplitude is enough to tip the net magnetization vector.

The simplest MRI experiment is called the Free Induction Decay (FID), where the global spin from a sample region with a uniform magnetic field is detected using a $\Delta\alpha = \pi/2 = 90^\circ$ pulse to flip the net magnetization vector into the transverse plane [51]. The signal is detected by an RF coil, and the induced emf is measured by an Analog-to-Digital Converter (ADC), which entails a discretization of the signal. If a signal is collected at N points, the sample time T_s can be defined as $T_s = (N - 1)\Delta t$.

A source of signal loss is the rapid dephasing of spins, which is described by T_2^* , a combination of T_2 and T_2' . T_2' corresponds to effects induced by the external field but can be avoided through the spin-echo sequence [51]. In this sequence, a $\pi/2$ pulse is first applied along the x' -axis, then a π pulse is applied along the y' axis. This last pulse reverses the spin order so that the spins do a rephasing before a new dephasing. Because the spins' phases change at a constant pace, all of them are rephased at the same time, creating an echo. This signal peak at the Echo Time (TE) is limited in amplitude by the transverse relaxation curve because the external field effects mainly influence the speed of dephasing or rephasing and not the amplitude. Figure 2.7 shows a simplified version of the spin echo sequence diagram and an illustration of the restricted signal

echo amplitude. The TE is the time between the 90° pulse and a specific sampling.

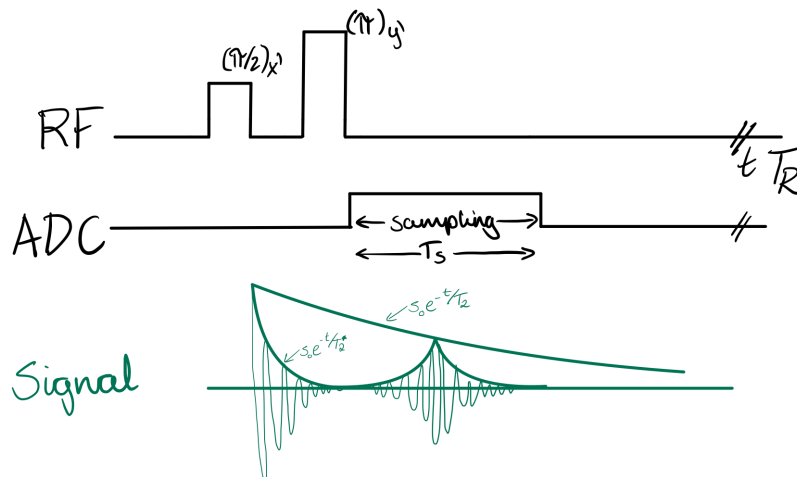


Figure 2.7: Sequence diagram for a spin-echo sequence. – This illustration is strongly inspired by Figure 8.3 in [51].

A key factor for imaging in MRI is the spatial localization of the signal. This information can be coded into the frequency information of the acquired signal by using gradient fields [52]. Gradient fields are, in the most common case, linear field changes introduced in the three linearly independent spatial directions, x , y , and z . With different experienced fields, the spins will have different Larmor frequencies in a specified voxel, and by applying the gradient fields in specific patterns, the RF signals become a function of both position and time. Without gradient fields applied, the precession frequency is assumed to be constant over the entire sample [53]. k -space is the overview of all voxels defined by the three-dimensional frequency vector \vec{k} , which associates the three linearly independent directions with frequency or phase encoding. The number of readouts in a scan refers to the total number of samples acquired in a volume.

The gradient fields can be applied before, during, or after an RF-pulse. The gradient echo method presents a typical way of spatial encoding. This method produces an echo by rephasing the spins as in the spin echo, but the phase change is due to the gradient field inhomogeneities. Suppose the gradient field produces a linear variation of the magnetic field symmetric around zero, summing with the B_0 . In that case, the range of difference in Larmor frequencies from the original Larmor frequency for the voxels along this field change will range from negative to positive. k -space must be sampled for all these frequencies to acquire a signal from all these voxels. In a typical gradient echo sequence for one line in k -space, this is done with a positive and then a negative pulse of a given amplitude; see Figure 2.8. The x -position is frequency encoded in the signal because the gathered samples can be reconstructed to a cosine signal consisting of different frequency components, each corresponding to a voxel along the gathered line in \hat{x} -direction.

The choice of gradient field directions relates to how k -space is covered [52]. A linear combination of the three physical gradient coils allows a linear change in field magnitude along any three-dimensional vector. A three-dimensional space can be covered using any three orthogonal vectors.

When the three gradient field directions are parallel to x , y , and z -axis, the traversal of k -space can be done line by line and slice by slice to end up with a three-dimensional space of samples [52]. An example is the imaging spin-echo sequence shown in Figure 2.8. Imaging spin-echo is a combination of spin-echo and the gradient echo method. Gradient echo is the technique used for the G_x , and an entire line, k_x , can be acquired in one sampling interval because the effect of the negative gradient pulse lasts halfway into the positive gradient pulse. [53]. The applied G_y gradient introduces phase encoding by letting the spins accumulate y -dependant phase, increasing along the y -direction. A slice can be acquired by repeating the process described in the sequence diagram of Figure 2.8 for every line in k -space. The different lines of G_y indicate the phase encoding steps. Applying G_z simultaneously with the RF-pulse performs slice selection. Slice thickness is dependent on the RF bandwidth. The slice is excited uniformly such that all spins have identical phases and flip angles before positional encoding of x - and y -position. The rephasing after the excitation is necessary to ensure uniform excitation [52].

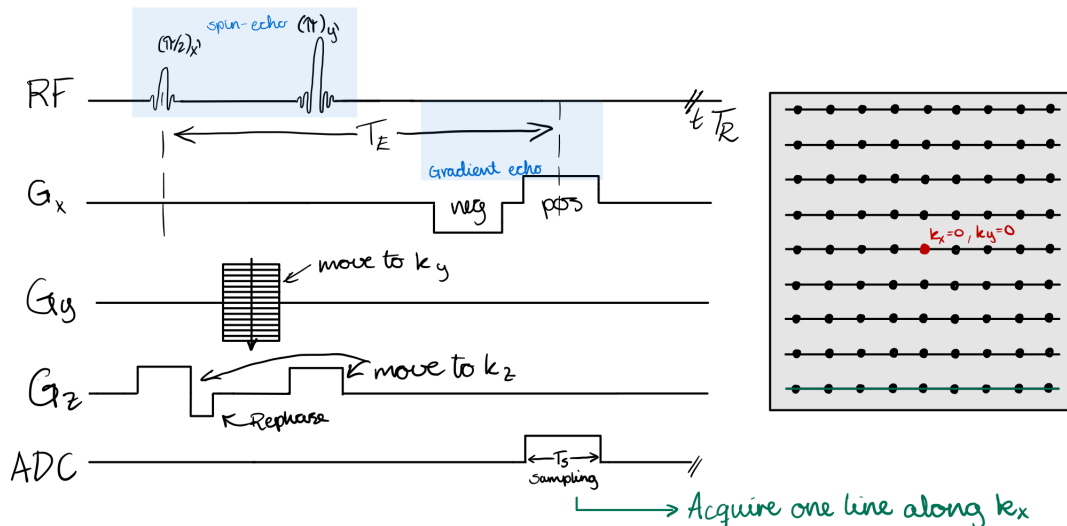


Figure 2.8: Sequence diagram for an imaging spin-echo sequence. – This illustration is strongly inspired by Figure 10.4 and Figure 10.17 in [52].

2.1.8 Image reconstruction

The acquired signal is given by equation 2.32, where the angle of a given magnetization vector is a function of spatial position and time, denoted by $\phi(\vec{r}, t)$, and expressed in equation 2.33 [53]. The spin density of the sample can be found by taking the inverse Fourier transform of the signal, which is defined by inserting the last part of equation 2.33 into equation 2.32.

$$s(t) = \int_V \rho(\vec{r}) e^{i\phi(\vec{r}, t)} d^3r \quad (2.32)$$

$$\phi(\vec{r}, t) = -\gamma \vec{r} \cdot \int_0^t \vec{G}(t') dt' = -2\pi \vec{k}(t) \vec{r} \quad (2.33)$$

The acquired signal can be used to find the spin density through equation 2.34. The spatial decoding and calculation of spin density are the same for different traversals of k -space. However, the relationship between the three different k -axes is defined by linear combinations of the cartesian axes relative to the applied gradient fields. The spatial resolution is defined by the shortest separation between two point sources necessary to distinguish between their signals in the resulting image [54]. The Fourier pixel size (Δx_f) is the limiting factor of spatial resolution. It can be defined by the sampling interval $\Delta k = 1/FOV$ in k -space and the number of samples (N) to be $\Delta x_f = \frac{1}{N\Delta k}$. The number of samples can be increased as high as the SNR and imaging time permits to maximize spatial resolution [54].

$$\hat{\rho}(\vec{r}) = \int k \cdot s(\vec{k}) \cdot e^{i2\pi \vec{k} \cdot \vec{r}} d^3k \quad (2.34)$$

Artifacts can arise from sample characteristics. The dielectric effect artifact arises because the lossy sample acts like a dielectric and changes the field strength through the object, i.e., the excitation flip angle varies between regions in the sample [55]. This artifact arises when the RF wavelength is shorter than the width or height of the imaged object and looks like a periodic shading in the image. The artifact looks different for linearly and circularly polarized fields but can arise for both [56].

Image distortions are misregistration of a spin's position due to an unexpected change in the magnetic field [57]. Suppose ferromagnetic materials are present in the scanner bore. In that case, they will introduce additional magnetic fields in their proximity, causing incorrect signal encoding, which looks like geometric distortions of expected shapes in the resulting image.

Inhomogeneities in the reception field will produce artifacts. For surface coils, the field strength falls off with distance from the coil. Such an inhomogeneous field can be mapped to a spatial dependency for more accurate spin density calculations [53].

If there are sudden changes between objects and air, ringing artifacts may occur [54]. Ringing is a typical artifact after a Fourier transformation of a step function, which results in a sinc function in the other domain. The sinc function is an oscillating function that never stops oscillating, although the amplitude reduces to zero as it approaches infinity. The reverse Fourier transform again will not be able to reconstruct the perfect step function because the Fourier transform is limited by temporal resolution, limiting the reverse Fourier transform's spatial resolution [53]. Oscillations at the edge of an object are called Gibbs ringing and can occur in both phase- and frequency-encoding directions.

2.1.9 Hardware

The most dominating part of the MRI machine is the solenoid magnet creating the strong B_0 -field. A strong B_0 field is essential because the maximum available SNR is proportional to B_0 [28]. Ultrahigh fields (7T) are often preferred when dealing with multinuclear MRI because of lower gyromagnetic ratios and concentrations in the hu-

man body, see Table 2.2. The solenoid magnet is usually a coil with many windings of superconducting material cooled down by liquid helium. The superconductivity and the associated cooling system take a long time to start up, so it is kept running constantly, except when it needs to be repaired.

All components and tools used inside the MRI room must be of non-magnetic material because of the ever-present main magnetic field. Paramagnetic and ferromagnetic materials have magnetic susceptibilities in the order of $10^{-6}m^3kg^{-1}$ and higher [58]. A list of common non-magnetic materials and their respective magnetic susceptibilities is provided in Table 2.3 [58, 59].

Table 2.3: *List of magnetic susceptibility values for selected materials* – Magnetic susceptibility of various materials fetched from [58] above the thick line and [59] below. Negative numbers are typical for diamagnetic materials. The value for an Flame Resistant 2 Printed Circuit Board (PCB) board is without the copper layer. Polylactic Acid (PLA) and Polyethylene Terephthalate Glycol (PET-G) are common materials for 3D printing.

Material	Magnetic Susceptibility, $X_{mass} [10^{-8}m^3kg^{-1}]$
Copper (Cu)	-0.108
Aluminum (Al)	0.768
Silver (Ag)	-0.227
Tin (Sn)	-0.396
Lead (Pb)	-0.139
Water (H ₂ O)	-0.904
PLA	-0.678
FR-2 PCB board	-0.748
PET-G	-0.580

The gradient coils responsible for spatial encoding of the Field Of View (FOV) are also part of the MRI machine [28]. These coils create a gradually increasing field strength along each of the three defined axes of the coordinate system. Three pairs of coils with current running in opposite directions create a magnetic field between them with a linear increment from negative to positive in the central region. Imaging with a higher resolution requires smaller voxels that require more change over small distances and more power in the gradient coils.

An RF coil must also be part of the system, positioned to create B_1 perpendicular to B_0 . Most MRI machines have a body RF coil inside the big solenoid resonating at the hydrogen frequency of the system [45]. This coil is used for transmitting the signal in most clinical situations because it provides a homogeneous transmit RF pulse in a large region of the scanner bore [30].

In the clinical setting, specialized receiver coils often perform the reception of the RF signals. The receiver RF coils are additional equipment that can be exchanged easily. Choosing the suitable receiver coil impacts the image quality hugely. The built-in body RF coil can theoretically be used for reception, but this would result in an image with lousy resolution because the coil is far away from the object to be imaged, and the received signal will be weak [30].

In research applications, transmit and receive coils can be customized to the experiment. Transmission and reception require specialized coils in multinuclear MRI because the resonance frequency differs from the hydrogen frequency. A transceiver RF coil performs both transmission and reception.

2.1.10 Sodium MRI

^{23}Na is a heavier nucleus than hydrogen and a lower gyromagnetic ratio [45]. ^{23}Na is one of the nuclei in the human body with a gyromagnetic ratio significantly larger than zero and a concentration that makes it interesting for MRI imaging, see Table 2.2. ^{23}Na yields the second largest in vivo NMR signal after hydrogen [60].

A large in vivo NMR signal does not guarantee a good MRI sensitivity in the human body. Even though ^{23}Na abundance is 100% [26], the concentration in the human body limits the available signal because it is many times lower than the hydrogen concentration, which the low ^{23}Na -SNR reflects. Another detail about the ^{23}Na atom is its spin quantum number $s = 3/2$, which results in a visible nuclear quadrupole moment because the possible magnetic quantum numbers are $m_j = -3/2, -1/2, 1/2, 3/2$ which gives four different energy levels according to equation 2.9. The four energy levels are prominent under the influence of an external field like B_0 in an MRI experiment [14]. The non-zero quadrupole moment poses both challenges and advantages with imaging. With specialized MRI sequences, the quadrupole moment can give additional physiological information [61]. However, the quadrupole moment is also a reason for the rapidly decreasing transversal magnetization [14]. One way of increasing the MRI sensitivity of ^{23}Na is to design specialized RF coils, but this alone is not enough.

Specialized MRI sequences can increase the SNR of ^{23}Na -MRI. The first ^{23}Na -MRI image was acquired with a three-dimensional (3D) gradient echo sequence [62], but novel techniques have been developed. A short TE is beneficial for the rapid decrease of transversal magnetization and could be achieved by starting the acquisition from the center of k-space and moving out radially [14]. One such method is a three-dimensional trajectory called 3D cones (CN), with acquisition lines twisting around one of the axes in a cone shape with its tip in the center of the FOV. This sequence was initially developed by Gurney et al. [63]. Figure 2.10 explains the CN sequence's k-space trajectory in a 3D plot, and Figure 2.9 shows the sequence diagram for a CN sequence. This method improves the point spread function of the acquisition method given enough different cone surfaces [63] and has proven advantageous for identifying small region ^{23}Na concentration changes in the brain [64]. The CN Ultra-short Echo Time (UTE) sequence can be used in an undersampled version to increase the temporal resolution in dynamically repeated ^{23}Na -MRI [64]. The sequence is defined by FOV, resolution, fraction of k-space sampling, Repetition Time (TR), and the total scan time. The fraction of k-space sampling is the ratio of acquired samples to the number of samples required to fulfill the Nyquist-Shannon sampling theorem [65].

Some example images from ^{23}Na -MRI brain scans are shown in Figure 2.11. These ^{23}Na -MRI scans were acquired with a three-dimensional radial gradient-echo sequence with a short TE at 3T [66]. Comparing the ^{23}Na -MRI (top row) to the T_2 -weighted

images (bottom row), it is clear that the resolution is lower in the sodium scan, and the highlighted areas are different. The TSC maps (middle row) show a clear difference between the healthy control and the patients with MS.

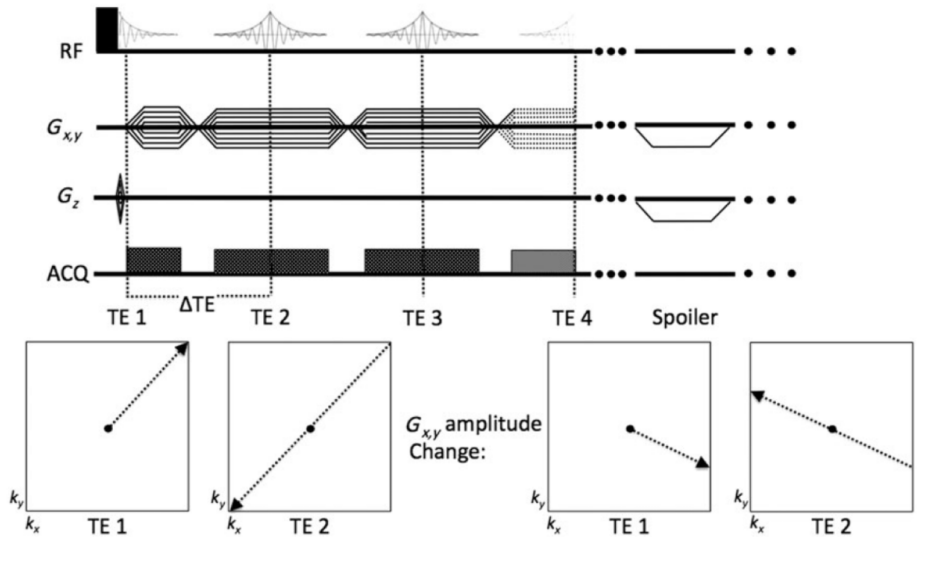


Figure 2.9: *Sequence diagram of a radial 3D cones UTE sequence* – A sequence diagram for ^{23}Na -MRI. Courtesy of Frank Riemer

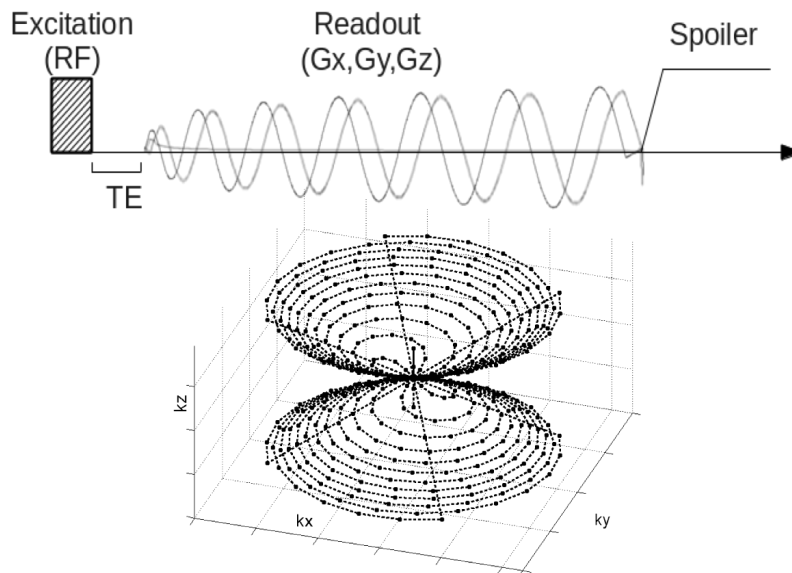


Figure 2.10: *K-space trajectory of a radial 3D cones UTE sequence* – An MRI sequence for ^{23}Na -MRI. Courtesy of Frank Riemer

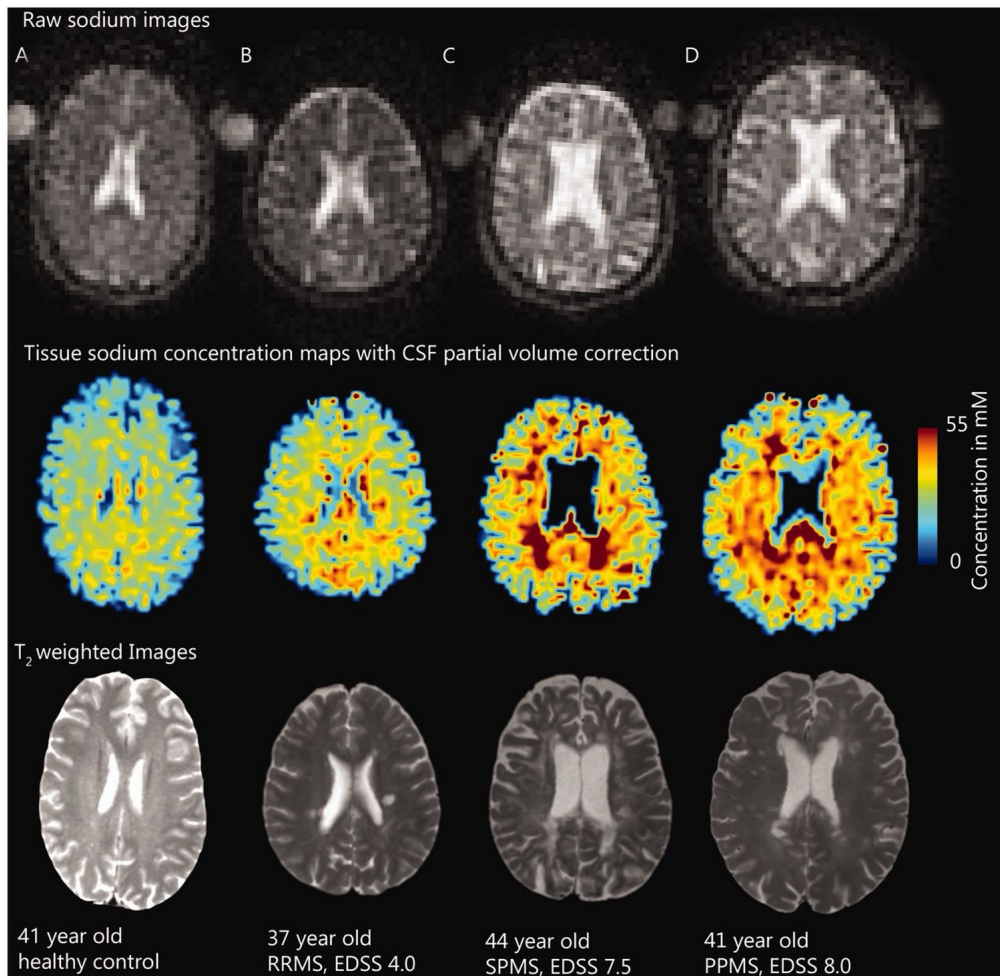


Figure 2.11: *Example images from ^{23}Na -MRI scans.* – The different scans show raw sodium images in sodium space (top row), tissue sodium concentration maps with partial volume correction (middle), and T2-weighted hydrogen MRI. This figure was reproduced from Paling et al. [66]

2.2 Electromagnetic fields

MRI examinations depend heavily on electromagnetic theory. Thus, any scientist working within MRI must know the origin and nature of electric and magnetic forces and fields.

2.2.1 Electric fields

The electric field around a wire arises from the electrons flowing in the wire. The force exerted on one point charge by another is expressed by Coulomb's law in equation 2.35 [67]. Where q_1 and q_2 refer to the electric charge magnitudes, R is the minimum distance between the charges, and ϵ_{p0} symbolizes the permittivity in vacuum. The vacuum permittivity is the electric constant from Table 2.1.

$$\vec{F}_{1,2} = \frac{q_1 q_2}{4\pi\epsilon_{p0}R^2} \quad (2.35)$$

The electric field around a point charge is defined by $\vec{E} = \frac{\vec{F}}{q}$, and the force of the electric field is measured in Newtons per Coulomb, N/C . From Coulomb's law, it can be noted that a factor of square distance reduces the electric field.

A group of charges produces a surrounding electric field, a sum of all the individual electric fields. This summation is allowed through the principle of superposition, which applies to Coulomb's law [68]. For a volume with a continuous charge distribution, integration is the most efficient way of calculating the field intensity at a specific point outside the volume. Integrating over a volume becomes more challenging with increased shape complexity. However, Carl Friedrich Gauss showed that the formula for the electrical field outside a sphere with continuous charge distribution is the same as for a point charge with a magnitude equal to the total charge of the sphere placed at the sphere center [68]. This observation hints at Gauss' law, which relates the electric field intensity to the net electric flux through a closed surface in equation 2.36.

$$\Phi_E = \oint_{\mathcal{C}} \vec{E} \cdot d\vec{A} = \frac{Q_{encl}}{\epsilon_{p0}} \quad (2.36)$$

In equation 2.36, Φ_E refers to net electric flux, \vec{E} refers to the electrical vector field, ϵ_{p0} to the electromagnetic constant (permittivity of vacuum), and $d\vec{A}$ to the surface vector normal to the surface at any point [68]. Electrical fields can be described by either E or $D = \epsilon_p E$ where D describes electric flux density independent of the medium, while E describes field intensity and direction [67].

2.2.2 Magnetic fields

Static magnetic fields have descriptors similar to the static electrical field, namely magnetic field strength H and magnetic flux density $B = \mu_p H$ where μ_p symbolize permeability [67]. The static magnetic force originates from electric charges moving at a constant velocity, meaning that a static magnetic field is produced from a constant flow of electric current through a wire [67]. The magnetic field intensity at a specific point outside a wire conducting electric current can be characterized using the Biot-Savart equation in 2.37, where $d\vec{l}$ is the directional vector of an infinitesimally small element of current, I is the current measured in amperes, and r describes the distance between the measuring point and the current leading wire. The integral sums over the entire current path, curve \mathcal{C} , assuming it is an ordered row of point charges. For each position in space, the magnetic field will be a vector quantity, meaning that it will have both a magnitude and a direction. The measuring unit for magnetic flux density is tesla, $T = \frac{N \cdot s}{C \cdot m}$, where N is Newton, s is seconds, C is Coulomb, and m is meter.

$$\vec{B} = \frac{\mu_0 I}{4\pi} \oint_{\mathcal{C}} \frac{d\vec{l} \times \vec{r}}{|r^3|} \quad (2.37)$$

The definition of Biot-Savart's equation here assumes an infinite current element,

which is never true in practice. However, it is ok to assume an infinite element as long as the point where the magnetic field is measured is close enough to the finite wire creating the field.

Both magnetic and electric forces depend on particles with an electric charge. The electric force, $\vec{F}_e = q\vec{E}$, and the magnetic force, $\vec{F}_m = q\vec{v} \times \vec{B}$, have a significant difference, the magnetic force is dependant of charge velocity (\vec{v}). In contrast, the electric force can work on a still charge, so if the charge is not moving, only the electric force can work. Moving charges can be part of a current-leading element. As a result, two current-leading wires will affect each other through their individually produced magnetic fields [67].

2.2.3 Induction and alternating current

From the Faraday induction law presented in equation 2.29, the induced ε in a wire loop requires a change of magnetic flux, ϕ_B [8, 9]. A change of flux can arise from a change in the size of the area or a change in the magnetic flux density. A field with constantly changing flux density will induce a constantly changing current in a wire experiencing the field. The unit for magnetic flux is called Weber $Wb = T \cdot m^2$, and induction can be described by Henry (H), $H = Wb/A$, showing that the inductance (L) increases with the flux per area [69].

Magnetic coupling between inductors or current-leading wires happens because a magnetic field change outside the wire affects the current running through the wire [70]. Magnetic interaction between different wire elements is called mutual inductance and can arise between parallel wires, wire loops, or inductors. It also arises within a wire loop between different wire elements.

When AC-current runs in a wire, it is essential to notice that the velocity distribution is not equal through the cross-section of the cylinder-shaped wire because of the skin effect [71]. The current flows more freely towards the outer shell of the wire, while the electrons in the middle of the wire cross-section stay in the same place. The reduced mobility of charges is a source of resistance affecting the induction properties of a wire configuration, and the resistance increases with the frequency of the AC.

2.3 RF electronics

Resonance is an exciting topic in many areas of technology, e.g., electronics, mechanics, and acoustics. AC circuits are resonators, with the current changing direction all the time, and the relation between current and voltage is not dependent on resistance R , but impedance Z [72]. Ohms law describing this relation is given in equation 2.38 where V stands for voltage and I for current.

$$V = Z \cdot I \quad (2.38)$$

Impedance describes both resistance and reactance in the system, indicating that the circuit contains both resistive and reactive components, like inductors and capacitors. These reactive components change impedance with the applied AC current's frequency, and when both inductance (L) and capacitance (C) are present, the circuit is a resonance system.

From the Larmor equation (Eq. 2.7), the precessional frequency for spin systems under the influence of a specific main magnetic field flux density (B_0) is given, and to fulfill the resonance condition, an RF coil also needs to resonate at the same frequency [73]. It is crucial to keep track of all the impedances to make the ideal electric resonator. The frequency response of the RF coil, i.e., its behavior at different frequencies, can directly influence the images through spatial modulation [28].

2.3.1 Passive components in RF circuits

Passive components in RF-circuits are resistors, inductors, capacitors, and other components not requiring power to function as they should. Conductors or wires must not be forgotten as they carry the current, creating the magnetic field that interacts with the spins of the sample in an MRI experiment [73].

Inductors and conductive wires

All components and wires have resistive losses. The dominating resistance in an RF circuit is assumed to come from the inductors and not the capacitors, so many circuit drawings and models include a small resistance right next to the inductor [71]. The long wire formed into an inductor introduces resistive loss because the electrons have to travel a long way in the metal.

The symbol for inductance is L , and the measuring unit is H , which can be defined by amperes, volts, and seconds, $[L] = H = \frac{V \cdot s}{A}$. From this, it is apparent that if the electric current through an inductor with an inductance of one henry changes at the rate of one ampere per second, it results in an electromotive force of one volt [72]. Mathematically, this looks like $V(t) = L \frac{dI}{dt}$.

Equation 2.39 describes the impedance of a pure inductor, with X_L indicating the reactance [72]. Suppose several inductors are connected in series or parallel. In that case, the rules for calculating the overall inductance are shown in equation 2.40 for series connected and equation 2.41 for parallel connected components.

$$Z_L = jX_L = j\omega L \quad (2.39)$$

$$L_{series} = L_1 + L_2 + \dots + L_N \quad (2.40)$$

$$\frac{1}{L_{parallel}} = \frac{1}{L_1} + \frac{1}{L_2} + \dots + \frac{1}{L_N} \quad (2.41)$$

The resistance of a wire or an inductor arises partly because a magnetic field is created around a wire when it carries current, which is a way of storing energy. Equation 2.42 [58] describes the induction properties of a conductive wire (L_{wire}) by the length (l_{wire}) and cross-section diameter (d_{wire}) in addition to the μ_p of the material and the skin depth (δ) at the given frequency. The skin depth accounts for the skin effect.

$$L_{wire} = 0.2 \cdot l_{wire} \cdot \left(\log \left(\frac{4l_{wire}}{d_{wire}} \right) - 1 + \mu_p \delta \right) \quad (2.42)$$

The inductance of a wire loop, including the mutual inductance between different wire segments of the loop, can be calculated using equation 2.43 [58]. A wire folded into a square will have similar inductance properties. The induction of a wire square can be calculated using equation 2.44, where (l_{side}) is the side length of the square [74]. However, the inductance of a loop of any shape can be estimated by the inductance of a circular loop with the same area [30]. Figure 2.12 shows the magnetic field around a circular loop with a diameter of 15 cm and a square loop with an equal area as the circle. Both loops have 400 amperes of current running through their wires. Notice the very similar patterns of field lines and magnitude. The basis for this figure is Biot Savart's equation (2.37) implemented in the Magpylib software [75].

$$L_{loop} = \frac{\pi}{5} \cdot D_{loop} \cdot \left(\log \left(\frac{8D_{loop}}{d_{wire}} \right) - 2 + \mu_p \delta \right) \quad (2.43)$$

$$L_{square} = 0.8 \cdot l_{side} \cdot \left(\log \left(\frac{2l_{side}}{d_{wire}} \right) + \frac{d_{wire}}{2l_{side}} - 0.774 \right) \quad (2.44)$$

Winding a wire in several turns close to each other forms a solenoid coil. The induction depends on the number of windings, the spacing between them, the wire thickness, and the diameter of each winding [30]. Equation 2.45 shows how to calculate the inductance in nano Henrys from the mean radius of the windings, r_m , the outer radius, r_{ext} , the thickness of the windings, e , and the length of the coil, l , all quantities given in millimeters. Induction of a solenoid coil can be decreased by increasing the space between the windings or lengthening the legs.

$$L_{solenoid} = 0.4\pi^2 n^2 \frac{r_m^2}{l + e + r_{ext}} \cdot A \cdot B \quad (2.45)$$

$$A = \frac{10l + 12e + 2r_{ext}}{10l + 10e + 1.4r_{ext}}, B = 0.5 \log_{10} \left[100 + \frac{14r_{ext}}{2l + 3e} \right]$$

The impedance of a solenoid coil also includes capacitance between the windings and the terminals. This capacitance between the windings leads to the Self Resonance (SR) of the coil [30]. The capacitance cancels the inductance at SR, and the component behaves like a capacitor for higher frequencies.

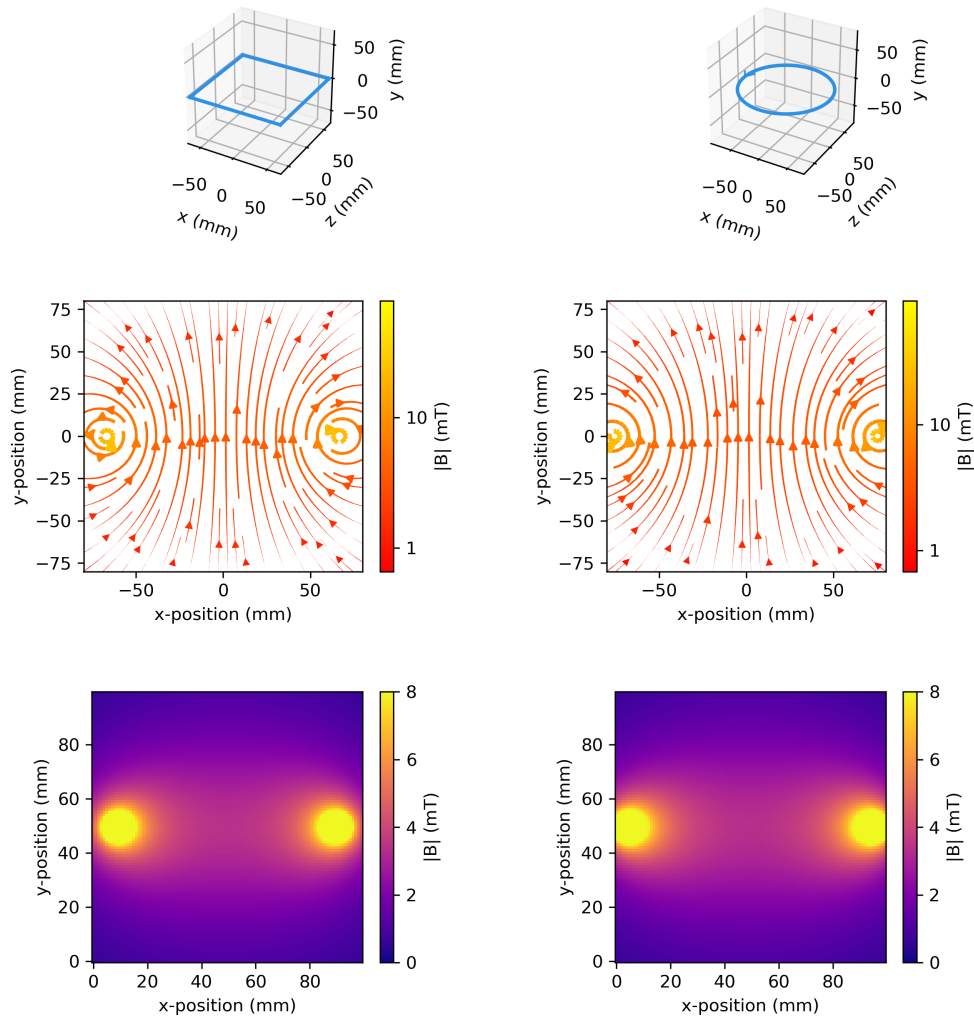


Figure 2.12: *Comparing square and circular loops enclosing areas of equal size* – The circular loop has a diameter of 15 cm. All figures to the left belong to the square loop, and all figures to the right belong to the circular loop. Both loops are shown in 3D with their magnetic field lines in $z=0$ and the magnitude of magnetic flux in slice $z=0$.

All inductors will be subjected to unwanted magnetic and electrical couplings with the surroundings, modifying their electromagnetic characteristics. Mutual inductance between wires leads to induced currents and modified inductance of the coil [76]. Electric coupling with surrounding wires leads to stray capacitances.

Capacitors

A capacitor blocks the Volts of Direct Current (VDC) signal. The impedance of a capacitor is characterized by equation 2.46 where X_C indicates the reactance [72]. Extending the fraction in this equation with j lets the impedance be positively defined. Capacitance influences a circuit's impedance inversely to inductance.

$$Z_C = -jX_C = -\frac{j}{\omega C} = \frac{1}{j\omega C} \quad (2.46)$$

SR is also a capacitor problem and must be specified by the vendor. If the frequency is too high, overcoming the SR frequency, the capacitor will behave as an inductor [71]. The small inductance in a capacitor arises from the connectors needed to place the capacitor in a circuit. As a rule of thumb, the larger the size of the capacitor, the larger its inductance, resulting in a lower SR frequency.

Capacitors connected in parallel add together like equation 2.49 shows. N capacitors connected in series reduce the overall capacitance like equation 2.47 show, and for $N = 2$ this can be rewritten to equation 2.48.

$$\frac{1}{C_{series}} = \frac{1}{C_1} + \frac{1}{C_2} + \dots + \frac{1}{C_N} \quad (2.47)$$

$$C_{series,2} = \frac{C_1 \cdot C_2}{C_1 + C_2} \quad (2.48)$$

$$C_{parallel} = C_1 + C_2 + \dots + C_N \quad (2.49)$$

Diodes

Passive diodes block the current in one direction but allow the current to flow in the other direction and are often referred to as current rectifiers. In an RF circuit, the current changes direction rapidly, and a diode will work against the direction change by only allowing the current to flow in one direction. Active diodes open only when additional voltage is applied, but these will not be discussed here.

The inner components of a passive diode are made of semiconductor material, creating a single PN-junction [77]. A semiconductor material with positive impurities, a p-material, is missing some electrons. Similarly, if it has negative impurities, i.e., having excess electrons, it is called an n-material. When a p-material and an n-material are placed close together, the transition region is called the p-n-junction or depletion region because electrons from the n-material have jumped over into the nearest holes of the p-material. The slight difference in electrical potential between the two materials is connected by charge movements in the junction, creating an electric field pointing from the n-material to the p-material. The current (I) through the diode is a function of the voltage (V) across the terminals. This function is presented in equation 2.50.

$$I(V) = I_0(e^{\frac{qV}{kT}} - 1) \quad (2.50)$$

Suppose the voltage is applied across the terminals with the positive pole to the p-material and the negative to the n-material. In that case, the electrical field between the materials increases, resulting in a net current through the junction, and the diode

is under forward bias conditions [77]. If the connections are reversed, reverse bias conditions result, and the applied voltage opposes the electrical field between the two sides. Some current will flow, but the saturation current is low. Figure 2.13 shows a plot of equation 2.50 with a saturation current $I_0 = 0.5A$.

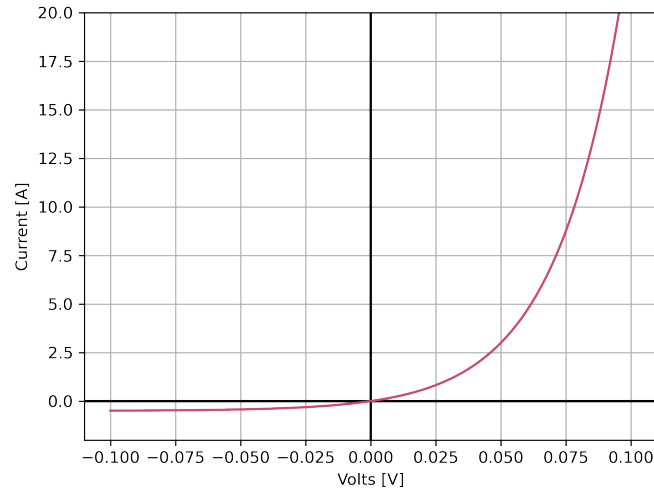
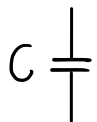


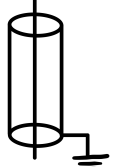



Figure 2.13: *The current flow through a p-n junction* – A simple model of current flow through a p-n junction, the functional part of a diode, inspired by Figure 42.29 by Young and Freedman [77].

Overview of passive components

An overview of the components typically used in RF circuits is provided in Table 2.4.

Table 2.4: *Overview of relevant passive components used in RF circuits* – The passive components used in this thesis are presented with their impedances.

Overview of passive components	Symbol	Impedance
Capacitor		$Z_C = \frac{1}{j\omega C}$, equation 2.46
Inductor		$Z_L = j\omega L$, equation 2.39 Induction of a solenoid, $L_{solenoid}$, is detailed in equation 2.45
Conductive wire		$Z_{\text{straight wire}} = j\omega L_{\text{wire}}$ with L_{wire} from equation 2.42
		$Z_{\text{wire loop}} = j\omega L_{\text{loop}}$ with L_{loop} from equation 2.43
		$Z_{\text{wire square}} = j\omega L_{\text{square}}$ with L_{square} from equation 2.44
Transmission line		$Z_0 = \frac{V}{I} = 50\Omega$ (Characteristic impedance)
Diode		Current is a function of voltage: $I(V) = I_0(e^{\frac{qV}{kT}} - 1)$

2.3.2 Electric resonators

RF circuits with capacitors, inductors, and connecting wires form a resonator with a resonance frequency[70]. The RF oscillations arise from energy being transferred back and forth between the capacitor and the inductor. The impedance of these components changes with frequency, following equations 2.39 and 2.46. At the resonance

frequency, the reactive parts complement each other, and the maximum current is only determined by the resistive part, which is the combined resistance of the imperfections of the circuit components and other fixed resistors. A pure resistance generates no phase shift, so the current and voltage are perfectly in phase at resonance. The cancellation happens within the circuit, meaning the voltage across the capacitor and the inductor can be higher than the voltage across the entire circuit. No electric system is perfect, and oscillations in an RF circuit will be damped over time because of resistance in the system.

The series resonant circuit

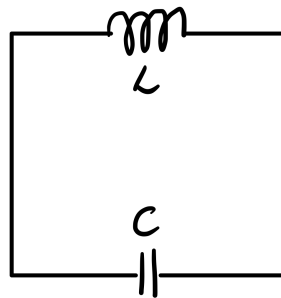


Figure 2.14: *The simplest version of a perfect electric resonator.*

Starting with a charged capacitor in series with an inductor, like in Figure 2.14, the electrons will flow from the capacitor to the inductor [70]. When the current through the inductor increases, more energy is stored in its magnetic field until the maximum current flow is reached. The capacitor will now begin to charge on the opposite side, and the current in the inductor will decrease until the charge on the capacitor reaches its maximum. At this point, the current through and the inductor's magnetic field have zero magnitudes. When the capacitor discharges again, the current will flow in the opposite direction, and the inductor's magnetic field will have the opposite orientation. This process will repeat itself forever if there is no loss, but this is not the case in real life.

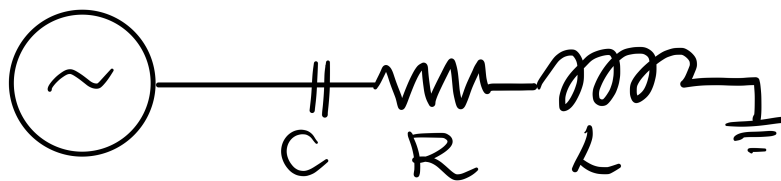


Figure 2.15: *A schematic representation of a series RLC circuit*

Another way of representing a series RLC circuit, i.e., a circuit with a resistor, a capacitor, and an inductor, is shown in Figure 2.15. The input impedance seen by the source is given in equation 2.51 [72]. The resonance frequency of the circuit is when $Z_L = Z_C$. Inserting equation 2.46 and 2.39 for Z_C and Z_L , and solving for f , the expression for the resonance frequency f_0 in equation 2.52 is found. The impedance of a circuit like this can be plotted with its magnitude and phase and will behave differently for different values of capacitance and inductance as shown in Figure 2.16 [72].

$$Z_s = Z_L + R + Z_C = j2\pi fL + R + j\frac{1}{2\pi fC} \quad (2.51)$$

$$f_0 = \frac{1}{2\pi\sqrt{LC}} \quad (2.52)$$

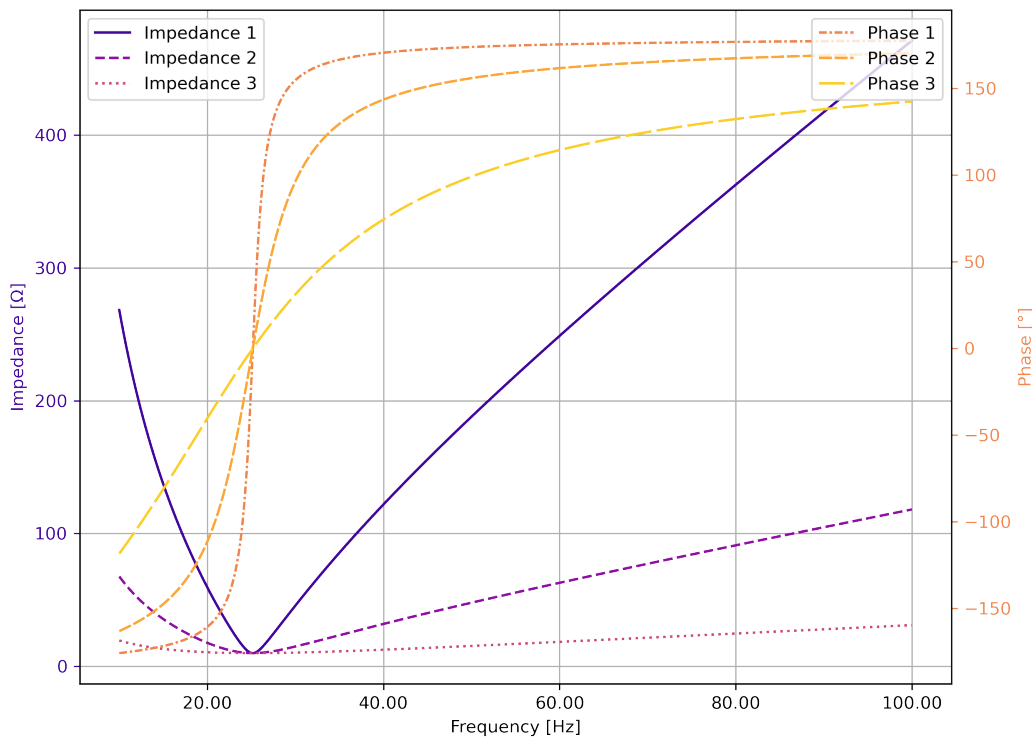


Figure 2.16: *The complex impedance of a series RLC circuit* – The frequency-dependent complex impedance of a series RLC circuit plotted with magnitude and phase. Three different circuits are shown; One with ($R=10.0\Omega$, $L=800\text{mH}$, $C=50\mu\text{F}$ with $Q=12.6$), Two with ($R=10.0\Omega$, $L=200\text{mH}$, $C=200\mu\text{F}$ with $Q=3.2$), and Three with ($R=10.0\Omega$, $L=50\text{mH}$, $C=800\mu\text{F}$ with $Q=0.8$)

The impedance of a series resonator circuit is lowest at the resonant frequency. By ohms law, equation 2.38, this means that the current running in the circuit will be at its highest at resonance [72]. For lower frequencies, the capacitor dominates, so the phase difference is -90° because the current is leading the voltage in a circuit with dominating capacitance. At resonance frequency, the two reactances cancel each other, resulting in zero phase difference. The inductor dominates for frequencies above the resonance frequency, and the phase is $+90^\circ$, i.e., the current lags behind the voltage. The impedance magnitude decreases when capacitance dominates because the impedance is proportional to the inverse of the frequency, as equation 2.46 shows. The phase of the total impedance in the circuit is -180° when the capacitor dominates and $+180^\circ$ when the inductor dominates, see Figure 2.16 [72]. When the inductor dominates, the impedance increases with the frequency because of the impedance being proportional to the fre-

quency in equation 2.39.

The Q factor of a resonator determines frequency selectivity. For the series resonator circuit in Figure 2.15, Q can be defined by either the capacitor's or the inductor's reactance at resonance divided by the series resistance R , see equation 2.53 [30]. Inserting the reactance of an inductor from equation 2.39 and the resonance frequency from equation 2.52 leads to the last part of equation 2.53. The Q factor is very important because it determines how steep the phase slope is at the zero crossing and, hence, the resonator's quality. If the Q -value changes for a resonator with fixed reactance, the change is caused by a change in the system's resistance.

$$Q = \frac{X}{R} = \frac{1}{R} \sqrt{\frac{L}{C}} \quad (2.53)$$

Parallel resonant circuit

A parallel RLC circuit can be drawn as shown in Figure 2.17. The input impedance seen by the voltage source is given by equation 2.54. The resonating frequency is where the capacitor's reactance cancels the inductor's reactance. The result is identical to the result for the series resonant circuit in equation 2.52 [72]. However, in a parallel resonant circuit, the impedance is at its highest at resonance. Figure 2.18 shows the increasing impedance when the inductor dominates until resonance and then a decrease when the capacitor dominates.

$$Z = \frac{1}{\frac{1}{R} + \frac{1}{Z_C} + \frac{1}{Z_L}} = \frac{1}{\frac{1}{R} + jC\omega + \frac{1}{j\omega L}} \quad (2.54)$$

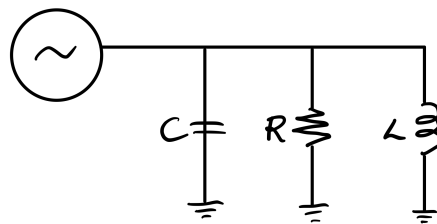


Figure 2.17: A schematic representation of a parallel RLC circuit.

For a parallel resonator circuit, Q is more easily defined using admittance Y than inductance because the admittance of components connected in parallel adds together like the impedance of components connected in series [30]. Impedance was defined as $Z = R + jX$, and similarly, admittance is defined as $Y = G + jB$, where G is called conductance and B is called susceptance. Equation 2.55 shows how these quantities can be used for calculating Q .

$$Q = \frac{B}{G} \quad (2.55)$$

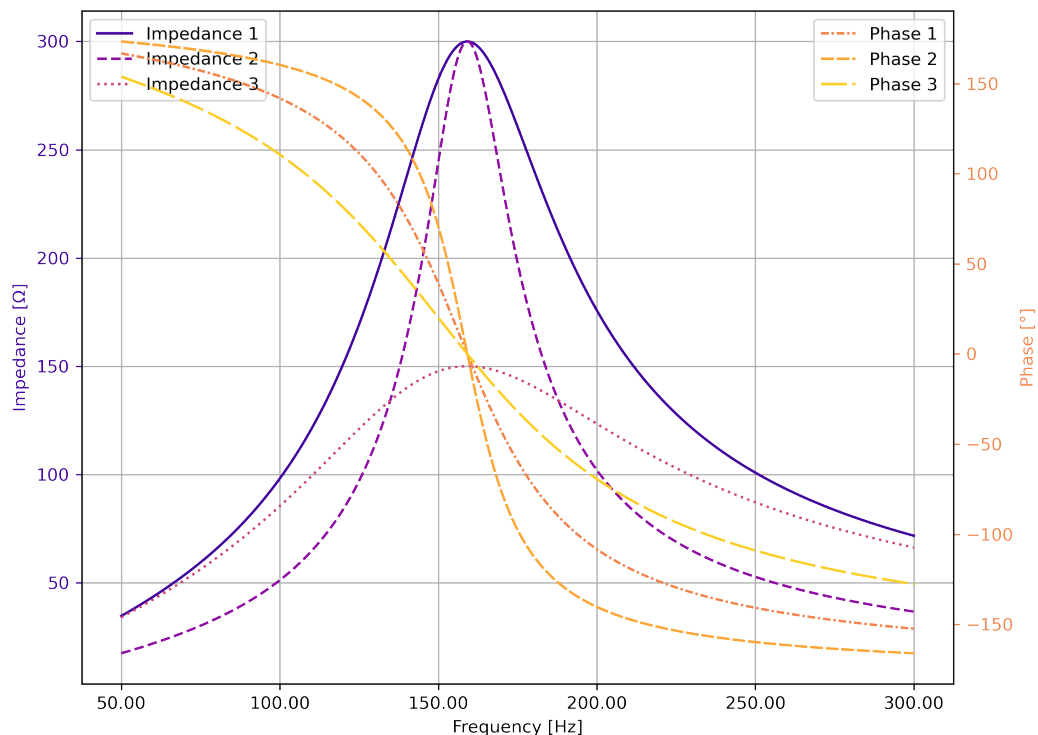


Figure 2.18: *The complex impedance of a parallel RLC circuit* – The frequency-dependent complex impedance of a parallel RLC circuit plotted with magnitude and phase. Three different circuits are shown; One with ($R=300.0\Omega$, $L=100\text{mH}$, $C=10\mu\text{F}$ with $Q=3.0$), Two with ($R=300.0\Omega$, $L=50\text{mH}$, $C=20\mu\text{F}$ with $Q=6.0$), and Three with ($R=150.0\Omega$, $L=100\text{mH}$, $C=10\mu\text{F}$ with $Q=1.5$)

2.3.3 Transmission lines

Transmission lines, for example, coaxial cables, are often used in RF circuits to carry the signal [78]. A transmission line has two parallel wires, usually one connected to the electrical ground while the other conducts the current. The two lines are separated by a substance providing a fixed impedance between the conducting wire and the ground. This impedance value is the characteristic impedance (Z_0) of the transmission line. In a coaxial cable, an outer layer of metal surrounds a dielectric material enclosing the inner wire. The outer layer of the cable is usually connected to the ground. The transmission line can be modeled by a lumped element circuit, i.e., a circuit of capacitors and inductors connected by lossless wires. Figure 2.19 shows the lumped element circuit of a transmission line, also called the pi-network [30]. Sometimes, several pi-networks in series are used to describe the transmission line.

Suppose a power source provides an incident AC voltage at one end of the transmission line. In that case, the signal will be transmitted to the other side of the transmission line or reflected to the source, depending on the source impedance relative to the transmission line's characteristic impedance [30]. Once the signal reaches the other end of the line, it will meet some load and be transmitted through it or reflected into the

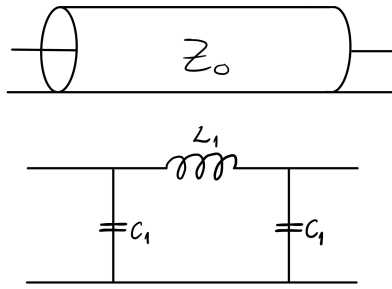


Figure 2.19: Lumped element circuit model of a transmission line.

transmission line. A reflected signal will coexist with the original signal, resulting in a standing wave. The current phase exiting the line will depend on the length of the transmission line. If all impedances are equal, no signal is reflected, and the incident signal travels through the transmission line before it is entirely absorbed in the terminating load. The reflection coefficient measures the match between the impedances and can be expressed as in equation 2.56. The reflection coefficient is zero with a perfect match between the impedances, while a complete mismatch like an open or a short circuit has a reflection coefficient of one [78].

$$\Gamma_{in} = \frac{V^-}{V^+} = \frac{Z - Z_0}{Z + Z_0} \quad (2.56)$$

2.3.4 The Smith Chart

Working with the equation in 2.56 repetitively is annoying and time-consuming. To make the work easier, MR. Philip Smith made the "Smith chart" in Figure 2.20 [79], which makes an easy conversion between impedance and reflection coefficient [78]. The easy conversion can be shown through rewriting equation 2.56 into 2.57, normalizing the impedance to the transmission line's characteristic impedance.

$$\Gamma_{in} = \frac{\frac{Z}{Z_0} - 1}{\frac{Z}{Z_0} + 1} \quad (2.57)$$

The real and imaginary axis is often drawn behind the Smith chart, with its center at the middle of the chart, and the complex impedance can be plotted in this coordinate system [79]. These axes are not drawn in the chart used in this thesis (Fig. 2.20). The reflection coefficient of a component is found by drawing a line between the impedance point and the center of the chart. The line's length and the angle between the line and the horizontal line will be the magnitude and phase of the complex reflection coefficient [78], given that the chart is normalized to the desired impedance.

The circles of the Smith chart in Figure 2.20 show the lines of constant resistance. In the center of the chart, the load impedance will be equal to the characteristic impedance of the transmission line Z_0 , in most cases a pure 50Ω resistive load [79].

The resistance will be constant at Z_0 when moving from the center along the intersecting circle, while the imaginary part changes following the numbers at the ends of each intersecting arc. These lines are convenient when adjusting the impedance to a specific value. The impedance of a device can be changed by introducing a capacitor or an inductor in series or parallel. The Smith chart provides a graphic road map to which components will change the device's impedance into the center of the chart [79].

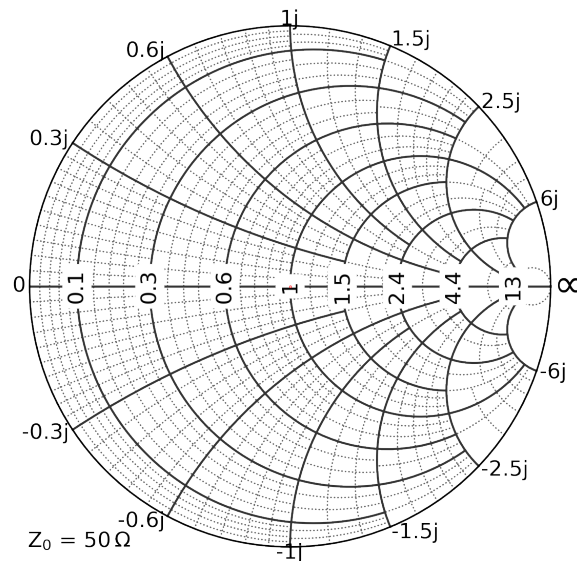


Figure 2.20: An empty Smith chart.

2.3.5 Linear network analysis

Linear network analysis is an essential tool to predict and understand the behavior of RF devices. While the impedance formulas for series and parallel circuits provide an understanding of simple circuits, the mathematics becomes very demanding when the circuit complexity increases. By only considering the output and input waveforms, linear network analysis makes the calculations easier [80]. The output waveform signal of the network is defined as a linear function of the input waveform signal. Several different functions can be used to characterize a network of components. Among them are the impedance matrix, the admittance matrix, the transmission matrix, and the scattering matrix. All of them have a size depending on the network's number of inputs and outputs. They can be used to characterize any network of components connected by transmission lines of a given Z_0 , for example, an antenna transmitter, a receiver, or filters.

The scattering matrix, or S-parameters, describes a network based on ratios of voltage amplitudes of the incident and reflected microwaves at the terminals [80]. The scattering matrix is handy when circuits are connected by transmission lines of given

Z_0 , and the circuit needs to provide a matching impedance. A general scattering matrix of a two-port network is given in equation 2.58 where V_1^-, V_2^- are the output voltage amplitude at each port defined as a linear combination of the input voltage amplitudes at each port, V_1^+, V_2^+ . The scattering matrix defines the linear combination.

$$\begin{pmatrix} V_1^- \\ V_2^- \end{pmatrix} = \begin{bmatrix} S_{11} & S_{12} \\ S_{21} & S_{22} \end{bmatrix} \cdot \begin{pmatrix} V_1^+ \\ V_2^+ \end{pmatrix} \quad (2.58)$$

The mentioned ways of analyzing a network can simulate it before assembling it and analyze its behavior experimentally after assembly [80].

2.3.6 The Vector Network Analyzer

The Vector Network Analyzer (VNA) is an instrument that makes it easy to obtain a network's S-parameters in the laboratory [30]. Ideally, the instrument is connected to all inputs and outputs and can apply voltages of different frequencies within a given range to all ports. The different ports' reflected and transferred power is measured and used to characterize the network. The system's characteristic impedance terminates all unused ports [81]. A high quality VNA provides complete information on relative amplitudes and phases of the incident, reflected, and transmitted wave signals over a wide range of frequencies. Most VNAs can plot the measurements on the Smith chart. Manufacturers of passive components, resistors, capacitors, and inductors often provide expected S-parameter plots in the specifications sheet.

Calibrating the VNA is vital for measurement accuracy because the measurement tends to be affected by connectors, cables, and the components inside the VNA itself [81]. Several possible calibrations with different detail levels and applications exist, such as a 1-port Short-Open-Load (SOL) calibration or a 2-port Short-Open-Load-Through (SOLT) calibration. These calibrations are based on error model methods with different numbers of terms depending on how many independent observations are made from the connected standards [82].

2.4 RF coil design for MRI

The electric design of an RF coil for MRI includes the construction of an electric resonator that resonates at the Larmor frequency of the spin system of interest. Besides the vital resonance frequency, the shape of the current leading wires is critical to which magnetic fields can induce a current in the coil during reception and what shape the magnetic fields will take when an AC current runs in the wires during transmission. The shape of the ROI influences the optimal geometrical shape of the coil [73]. For small ROIs close to the surface, good quality MRI images can be acquired using pretty simple surface coils, while larger ROIs or ROIs placed deeper inside the body are best to examine with volume coils. RF coils can be pure transmit or receive coils or transceivers [28].

In an ideal situation, the RF pulse created for transmission is uniform at any time in the ROI. According to Maxwell's equations, this is impossible because a time-varying magnetic field will vary with spatial position [28]. However, these variations can be ignored for distances shorter than the wavelength [56]. The wavelength of an RF pulse's propagation can be calculated from equation 2.59, where the frequency is denoted by f , the speed of light (c), and ϵ_{pr} is the permittivity of the medium relative to the permittivity in vacuum.

$$\lambda = \frac{f}{c \cdot \epsilon_{pr}} \quad (2.59)$$

By the principle of reciprocity, the flux through the coil and thus the emf produced in the coil during reception depends on the 'receive' field produced by the reception coil, which is proportional to the transmit field [11, 83]. Therefore, when deciding on a particular geometric shape of the coil, both for a transmit coil and a receive coil, it is helpful to calculate the static magnetic field produced by a direct current running through the wires. Static field calculations can be done using Biot Savart's law 2.37. These calculations can estimate the filling factor of the coil, meaning the overlap between the ROI and the coil's sensitive volume [84].

2.4.1 Surface coils

A surface coil is essentially a wire enclosing an area, like the examples provided in Figure 2.12. The reach of a surface coil's magnetic field is usually short, but this is also an advantage if the ROI is close to the imaging object's surface [85]. A smaller reach reduces the amount of tissue contributing with noise to the received signal.

A circular surface coil is straightforward to imagine, but the exact shape is not as important as the size of its enclosed area [85]. More advanced surface coils include several coil elements. Two or more loops can be combined into an array to make the coil's sensitive area cover a wider ROI. A phased array is a series of linearly polarized surface coils added together with spatially dependent weights [86]. Two coil elements can also be operated in quadrature to make a circularly polarized field [35].

2.4.2 Volume coils

Volume coils aim to create a homogeneous field in a large volume. One example is the Helmholtz or clamshell coil, where two wire loops are placed on opposite sides of the object to be imaged and fed with AC current of equal amplitude and a phase difference of 180° [87]. A highly homogeneous field is then created in the center cylinder of the two coils.

Another volume coil is the birdcage coil. Figure 2.21 shows an example of such a coil. The name arises from the shape because two loops are joined together by several legs or rods. Capacitors are placed either along the rods or as part of the circles between the attached rods to create a resonator circuit. The capacitors' placement separates them

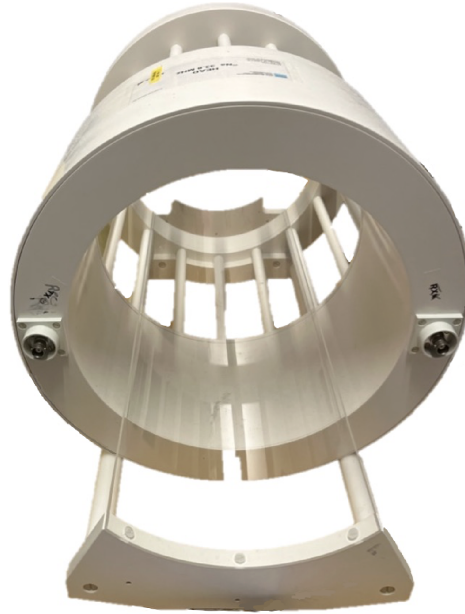
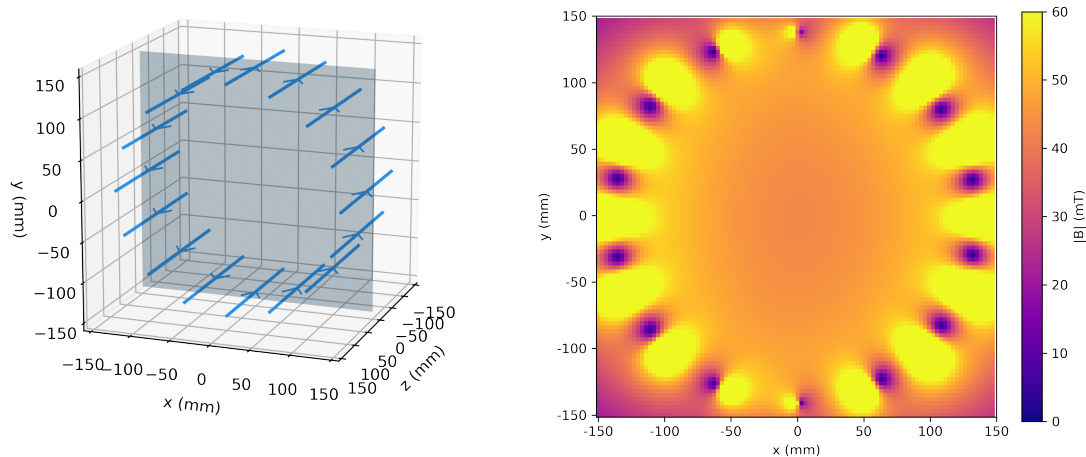


Figure 2.21: *Example picture of a birdcage coil* – Picture of RAPID Biomedical’s dual-tuned head coil for 3T, tuned for hydrogen and sodium.

between two different types, the high-pass and low-pass birdcage coil [87]. The types were named this way because their constructions resemble electrical high-pass and low-pass filters. The current in each rod varies through the array of rods around the circle [87]. The current amplitudes around the circle at a given moment are given by equation 2.60 [88, 89], where N is the number of rods, I_0 is the applied current, ϕ is the phase factor, k is the resonant mode, and n is the specific leg. The ranges of k and n are both 0 to $N - 1$.

$$I_n = I_0 \cos(\pi kn/N + \phi) \quad (2.60)$$

Figure 2.22 shows a static field calculation for a head coil with 16 rods at one specific moment. The magnitude plot of Figure 2.22 b) shows different magnetic flux density distributions surrounding the 16 rods. The different magnetic flux density distributions follow an entire cosine period around the circle because of the different currents running through the rods.



(a) 3D model of birdcage rods.

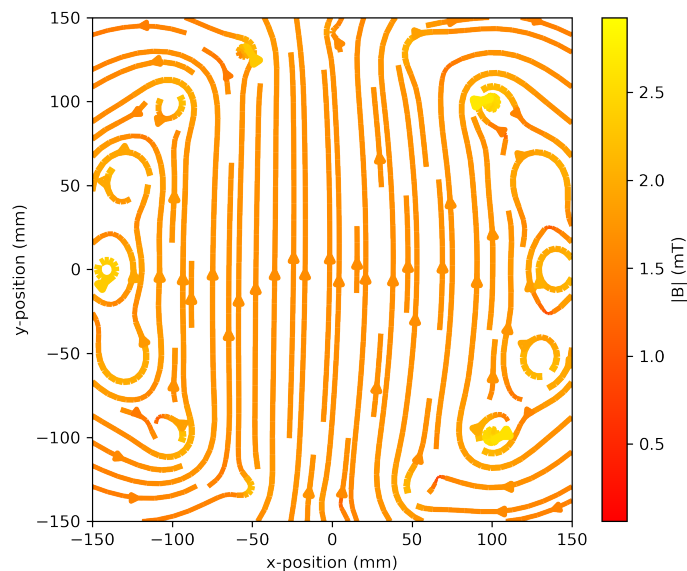
(b) Field magnitude in plane $z=0$.(c) Field lines in plane $z=0$.

Figure 2.22: *The magnetic field inside a birdcage coil* – Static field calculations for a birdcage head coil with 16 rods. The current elements included to simulate the 16-rod birdcage coil are shown in a), including a plane indicating where position $z=0$. The magnitude of magnetic flux density in slice $z=0$ is shown in b), and the field lines of the same slice are shown in c). The source code for creating this illustration is linked in Appendix A.

A birdcage coil can have a linearly or circularly polarized field. A linearly polarized field can be produced in any direction in the x - y -plane by choosing the appropriate phase factor ϕ . Birdcage resonators have many modes, but only one is tuned to the resonance frequency ($k=1$) [87]. Fortunately, the $k=1$ mode of the birdcage coil is intrinsically degenerate, and there is a pair at spatial positions 90 degrees apart [88]. These two degenerates of $k=1$ can be driven in quadrature to create a circularly polarized field [87]. With quadrature driving, the parallel field lines in the center of Figure 2.22 c) will rotate in the x - y plane at the chosen frequency. The field homogeneity is

excellent within a birdcage coil compared to the surface coil and increases with the number of rods. However, the sensitivity is substantially less in a small ROI within a birdcage coil compared to what a surface coil can achieve.

2.5 General concepts of RF coil construction for MRI

The construction of an RF coil requires some special considerations to ensure good functionality during an MRI experiment [30]. The coils must be of non-magnetic material, and a high sensitivity to MRI signal makes them sensitive to noise. With all circuitry connected, variable capacitors can be added to make the resonance frequency variable for imaging different samples [28]. Transmit coils should provide strong B_1 fields to shorten the time required for flipping the spins and good homogeneity over the imaged volume. Receive coils should also have homogeneity, but the most critical parameter is a high SNR.

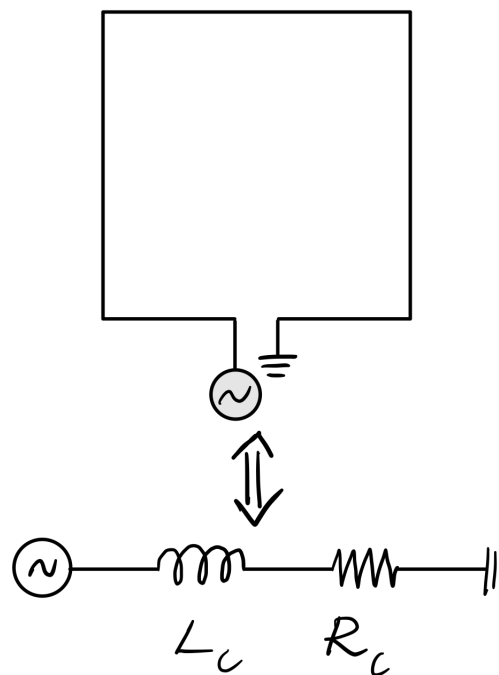


Figure 2.23: *The lumped element circuit of a square loop* – A square loop can be represented by an inductor in an equivalent lumped element circuit.

2.5.1 Matching and tuning

Tuning means to adjust the resonator to the desired frequency. Matching is done to avoid signal reflection when connecting the coil to the scanner through a transmission line. The signal can be reflected both during transmission and reception if the coil does not present with the same input impedance as the characteristic impedance of

the transmission line and the MRI system [90]. Usually, the MRI systems work with $Z_0 = 50\Omega$, so the coil must be seen as a 50Ω load. It is hard to match a circuit of a high-quality factor to a broad frequency band, but fortunately, an NMR probe only needs to be matched at the desired resonance frequency. Connection and adjustment of the matching network affect the properties of the main loop, which requires a new tuning procedure. Under development, tuning and matching circuitry adjustments must be made interchangeably [90].

Tuning and matching of the simple wire configuration of a square loop like the one in Figure 2.23 starts by adding a capacitor to cancel out the reactive component, i.e., the coil inductance, at the desired resonance frequency, creating a resonator [90]. This capacitor can be connected either in series or parallel with the loop. The remaining resistive component must be adjusted to the transmission line's characteristic impedance. Usually, this adjustment introduces a new reactive component that has to be canceled by another reactive component.

There are several ways of designing a matching circuit. The most basic matching network is the L-network [79, 90]. The network resembles the shape of an L and has four different configurations. Two are displayed in Figure 2.24. When developing RF coils, avoiding inductors in the matching network is advantageous because they incorporate more resistive losses than capacitors. Figure 2.25 shows how a parallel and a series resonator can be matched to the characteristic impedance using one of the L-shaped matching networks in Figure 2.24. Capacitors cancel the inductors of the L-network.

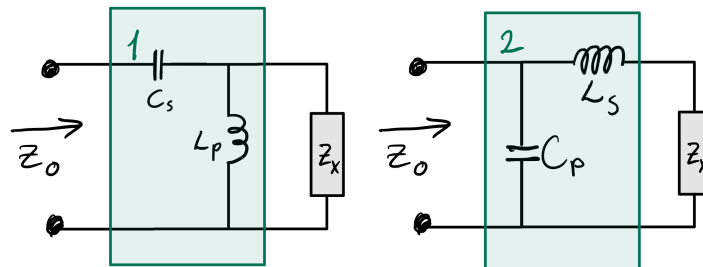


Figure 2.24: *The L-shaped matching network* – Schematic for the L-shaped matching network. There are four different configurations, but only two are displayed here.

The matching capacitor's value C_M in the matched parallel resonator in Figure 2.25 can be calculated from equation 2.61. R_{coil} is calculated in equation 2.62, which is a rewrite of equation 2.53 and makes a rough estimate of coil resistance. The Q required in equation 2.62 should be the loaded Q to ensure the conditions are similar to those inside the MRI during the planned experiment. Without a phantom, the resonance frequency might shift from the desired frequency [90].

$$C_m = C \cdot \sqrt{\frac{R_{coil}}{Z_0}} \quad (2.61)$$

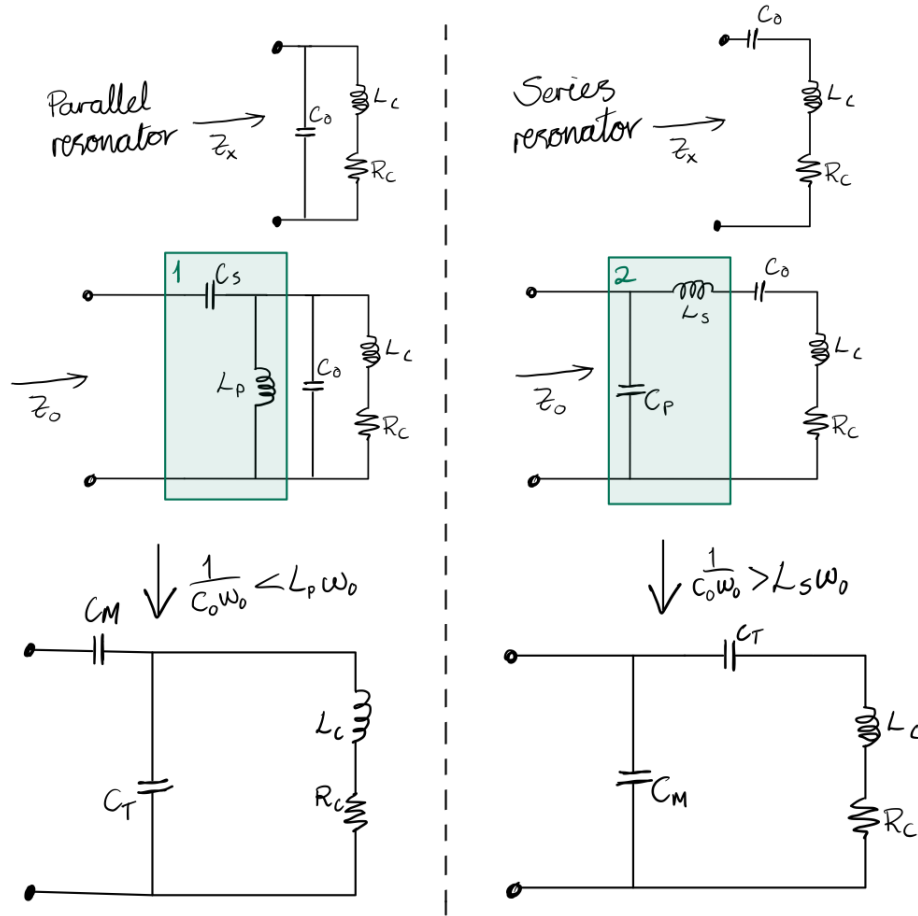


Figure 2.25: Illustration of a matching procedure for simple resonators – A parallel and a series resonator are matched to the characteristic impedance Z_0 of a transmission line using the L-shaped matching network.

$$R_{coil} = \frac{\omega L}{Q} \tag{2.62}$$

The simplest series matching circuit makes the matching unbalanced; see the final circuit for the matched parallel resonator in Figure 2.25. An unbalanced design is vulnerable to minor changes in the cable configuration because parasitic capacitance is allowed to influence the signal. A balanced matching circuit will avoid these problems and can be achieved by adding another capacitor on the other side of the resonator [91]. The two matching capacitors are connected in series, so their capacitances must be C_m doubled. The second capacitor blocks common-mode current, i.e., parallel current flow along the coaxial cable’s two lines. Both capacitors could be variable to adjust the matching, but the voltage across them will be significant. If a variable capacitor is placed between the current line and ground, variation is made possible simultaneously as the voltage across this variable capacitor will be small.

A resonator can be matched inductively by an additional loop or small solenoid coil. The mutual inductance between these loops is matched to 50 Ohm by changing the additional loop/solenoid coil’s induction value [90]. Hardly anyone uses inductive

matching in RF coils for MRI. However, the concept is helpful when measuring the resonance frequency and Q -value for a coil without a transmission line connected.

Transmission lines can also be used for matching. The lumped element model of a transmission line, i.e., the pi network, is a standard matching network [79]. The transmission line is used as a phase shifter or impedance transformer. However, for MRI applications, transmission line matching can become too bulky depending on the desired frequency [90].

2.5.2 Capacitor distribution

Depending on the nuclei and the field of the MRI scanner, a distribution of capacitors around a surface loop might be a good idea [85]. The distribution will reduce possible interferences and the maximum voltage over each capacitor, allowing for simpler, more available components. For lower-frequency experiments, the reduced voltage across the components is the dominant reason for distributing the capacitance. With several capacitors in the system, one can be variable to enable tuning. For higher frequencies, the dominant reason for distributing capacitors is to reduce the electrical length of the coils.

2.5.3 Quality measurement

The two main quality measurements of an MRI probe are the Q ratio and the SNR [81]. The Q ratio defines the electrical quality of the probe while the SNR characterizes the quality of the MRI image.

The Q ratio

The Q ratio reflects the coil performance by comparing the loaded and unloaded Q factor; see equation 2.63. Maximizing a coil's Q ratio minimizes the coil's electric losses because the difference between a loaded and an unloaded coil only depends on resistive losses in the sample load [81]. Thus, the Q ratio can only be increased by reducing electric losses.

The Q factor of large resonating networks can be determined using S_{11} -parameter measurements [92]. A fundamental definition of the Q factor is given in equation 2.63 where the Larmor frequency (ω_0) is connected to the peak energy stored in either the magnetic or electric field, and the average power dissipated within the network. From this, there is derived an experimental way of determining Q from the complex S_{11} parameters in equation 2.64 where R and a numerical calculation of $\frac{\partial X}{\partial \omega}$ are defined in (2.65) and (2.66), respectively.

$$Q = \omega_0 \frac{\text{Peak energy stored}}{\text{Average power dissipated}} = \frac{Q_{\text{loaded}}}{Q_{\text{unloaded}}} \quad (2.63)$$

$$Q = \frac{\omega}{2(R + Z_0)} \frac{\partial X}{\partial \omega} \quad (2.64)$$

$$R = Z_0 \frac{(1 + \text{Re}[S_{11}])(1 - \text{Re}[S_{11}]) - \text{Im}[S_{11}]^2}{(1 - \text{Re}[S_{11}])^2 + \text{Im}[S_{11}]^2} \quad (2.65)$$

$$X = Z_0 \frac{2\text{Im}[S_{11}]}{(1 - \text{Re}[S_{11}])^2 + \text{Im}[S_{11}]^2} \quad (2.66)$$

$$\frac{\partial X}{\partial \omega} \cong \frac{n(\sum \omega X) - (\sum \omega)(\sum X)}{n(\sum \omega^2) - (\sum \omega)^2}$$

An alternative method for determining Q assumes that the resonator has a simple R-L-C circuit equivalent with a single resonant point [92]. Then, the Q factor can be found experimentally using equation 2.67. This method is inaccurate for low Q circuits but can be helpful in comparisons during development.

$$Q = \frac{\omega L}{R_c}, Q = 2 \frac{f_0}{\Delta f} \quad (2.67)$$

The Q ratio is found by taking two measurements of Q , one without a sample present $Q_{unloaded}$, and the other with a sample present Q_{loaded} . The Q ratio is the ratio of Q_{loaded} to $Q_{unloaded}$, see equation 2.68.

$$Q_{ratio} = \frac{Q_{unloaded}}{Q_{loaded}} \quad (2.68)$$

For a hydrogen coil at 3T, a Q ratio of 3-4 is accepted as good enough. By increasing this number, there are no significant advantages to gain. The possible achievable values of the Q ratio are lower if the wanted resonance frequency is low enough that the RF loss in the sample is increased. The sample losses cannot be reduced [73].

Signal to Noise Ratio

The SNR is often measured from an MRI image of a phantom with a known concentration of the given atomic spins but can also be measured in an image of, e.g., the brain. SNR is the ratio of signal to noise, a division of a signal measurement in the light region by a background noise measurement. A percentage of the achievable SNR for a coil compared to a perfect coil with no electric losses can be approximated by equation 2.69 based on the coil's Q ratio [36].

$$\frac{SNR_{approx}}{SNR_{perfect}} = \sqrt{1 - Q_{ratio}} \quad (2.69)$$

SNR can be measured in several ways, but some methods are considered stan-

dards. The National Electrical Manufacturers Association (NEMA) has summarized some standard methods of calculating the SNR in the report called "Determination of Signal-to-Noise Ratio and Image Uniformity for Single-Channel Non-Volume Coils in Diagnostic MR Imaging" [93]. The method of measuring SNR described in section 2.5 of this report defines two regions of a single image, one for the signal measurement and one for the noise measurement. The signal measurement should be in the Measurement Region of Interest (MROI), i.e., where the coil is intended to be able to sense a signal. The average pixel value of a square of 7x7 pixels in this area is the measured signal (S). The noise measurement (NS) is a standard deviation of a square of 11x11 pixels in an area free of signal and artifacts. From these two measurements, the SNR can be calculated using equation 2.70. The factor 0.655 relates the probability distributions of the two measurements [93].

$$SNR = 0.655 \cdot S/NS \quad (2.70)$$

NEMA's description of SNR measurements also states that when only one image is used to measure the SNR of a surface coil, it must be of a slice in one of the central areas of the coil.

2.5.4 Noise

Electrical components and the sample itself contribute to noise in the signal. Equations 2.71 and 2.72 show how the resistance in the coil (R_{coil}), electronic components ($R_{electronics}$), and the sample (R_{sample}) affect the noise in the coil signal [28]. The noise depends on the bandwidth (Δf) of the coil's frequency response and the coil temperature T_{coil} , as well as Boltzmann's constant (k). Electrical noise from imperfect solder connections, impurities in components, or poor matching are minimized by maximizing the Q ratio [30]. The sample is expected to be the dominating noise contributor, and the resistance from the sample is proportional to the distance between the coil and the ROI. If the geometry of the imaging ROI is used to reduce the coil's effective imaging volume to a minimum, then SNR will increase because there are fewer noise contributors [28].

$$noise \propto \sqrt{4kT_{coil}\Delta f R_{eff}} \quad (2.71)$$

$$R_{eff} = R_{coil} + R_{sample} + R_{electronics} \approx R_{sample} \quad (2.72)$$

Studies of MRI noise have shown that the noise follows the Rician distribution [94]. This distribution is reduced to a Rayleigh distribution for low signal values, which will be the case in the noise measurement. In contrast, it is reduced to a Gaussian distribution in regions of solid signal values.

The rapidly changing fields of the gradient coils result in rapidly changing flux through all parts of the MRI system. All current leading material will produce fields

to oppose the external field changes, and the opposing field originates from induced currents, usually called Eddy currents [28]. The eddy currents induced in the RF coils and shielding of the main magnet can result in variations in magnetic flux density, which appear as phase errors, distortion, and chemical shift artifacts in the resulting images [28].

2.5.5 Phantom properties

Phantoms for MRI can be made with many different purposes. A phantom can be specialized concerning anatomical accuracy, tissue-mimicking materials, or tissue relaxation times [95]. Most tissues in the human body are composed of more than two-thirds of water [96], making water bottles an adequate MRI phantom. However, human tissues' electromagnetic properties strongly depend on the remaining non-water part of the tissue. These include ions, amino acids, enzymes, and other particles affecting the solution's electromagnetic properties and relaxation times [95]. Changing phantoms or switching from a phantom to a human might cause the resonance frequency to shift if the phantom does not resemble the body's dielectric properties [90].

2.5.6 Interaction and coupling between several coil elements

If two RF coils similar to the ones in Figure 2.12 resonating at the same frequency are brought close together, they will interact through mutual inductance and become one system [85]. This new system is not a sum of the two previous single modes but a new one with two new modes. The two modes can be explained by considering the different paths the current can take. The first path is around the outer perimeter. In a sense, this is equivalent to a single surface coil with a larger area. The other mode is if the two wires in the middle carry current in opposite directions; this is often called a figure eight configuration. The two coil elements must be decoupled to make the two modes resonate at the same frequency. Most decoupling methods can be divided into inductive and capacitive [97].

Inductive decoupling for two surface coils can be done by overlapping the area of the two loops. If the overlap becomes too large, the modes will split again [85]. Another way to decouple them inductively is to make a transformer between them. Such a transformer is two small inductors, one in series with each coil. These are then overlapped to give the same effect as the method with the overlapping loop area, but the required space is significantly smaller because each inductor has many windings.

2.5.7 Detuning circuits

There are advantages to having different transmit and receive coils [85]. A parallel resonance circuit might be introduced to make a coil inactive during transmission. Passive or active diodes can be forward biased when the detuning should be active [85]. The parallel reactive components will change the resonance frequency significantly, resulting in minimal current at the Larmor frequency. Passive diodes with a threshold value

above the voltage level induced by the spins during reception activate the parallel reactive components only during transmission and detune the coil. Whatever the purpose of introducing a detuning circuit, it implies the addition of several components to the circuit, and a new round of tuning and matching must be performed.

2.5.8 Connecting coils to the MRI

To connect a transceiver RF coil to the MRI machine, a T/R switch is needed [90]. T stands for transmit, and R for receive. The transmission part of the MRI system contains current sources and huge amplifiers to make the alternating current strong enough when it reaches the RF coil. The reception part is a very sensitive preamplifier that amplifies the received signal and makes it possible to read for the MRI system. An RF coil intended for both transmission and reception must be connected to the right system at the right time, and the switch between the two connections must be done quickly. During transmission, the reception system's preamplifier must be shielded from the transmission system [90].

2.5.9 Quadrature driving

To drive two coils in quadrature is a very effective way of transmitting and receiving signal in the MRI setting because all of the applied power is used to create a circularly polarized B_1 -field during transmission and the SNR is increased during reception by adding two signals received simultaneously [50, 35]. Quadrature driving requires two coil elements driven with currents of phase difference 90° . The two coil elements produce orthogonal magnetic field components, which are added together by the principle of superposition. Such a circularly polarized field is illustrated in Figure 2.26 by equation 2.24 rewritten to only include cosines: $\vec{B}_1^{circ} = B_1(\hat{x}\cos(\omega t) - \hat{y}(\cos\omega t + \pi/2))$. The illustration applies the resonance frequency of ^{23}Na at 3T. A phase delay of exactly 90° between the orthogonal fields yields an RF pulse following the colored arrows in Figure 2.26, while a phase delay of 85° yields the grey arrows. The geometry and the phase delay employed in the experiment are essential in a setup with two coils operated in quadrature [50].

The power splitter and combiner

A Hybrid is a four-port symmetric device that splits the power into two outputs with a phase shift between them in one direction and adds two inputs applying the inverse phase shift in the other direction [50]. Two coils operated in quadrature require two power sources with equal amplitude and a 90° phase shift between them. The symmetry of a 90° Hybrid makes it possible to create either a left-polarized circular field like the ones described with equation 2.24 or a right-polarized circular field, depending on which port is used as the input port [50]. The illustration in figure 2.27 explains the principle of driving an NMR probe in quadrature with a Hybrid 90° .

A quadrature Hybrid can be designed in several ways [50]. Figure 2.28 presents the lumped element circuit of the $\lambda/8$ quadrature Hybrid. The different component values

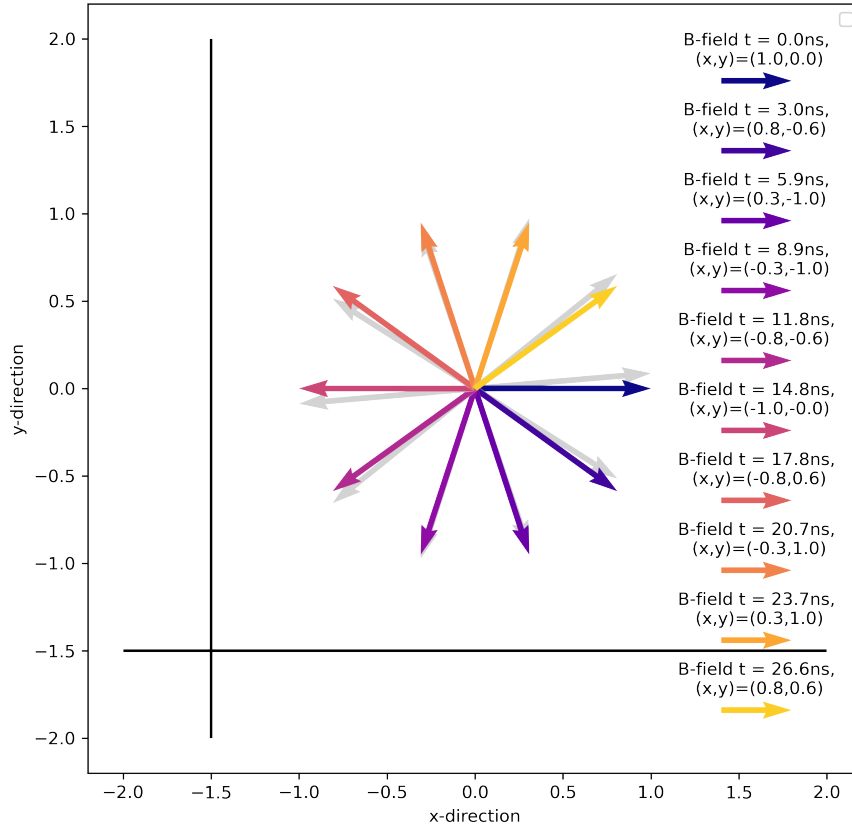


Figure 2.26: Illustration of a circularly polarized field. – B-field vectors throughout the rotational period at the point where two coil’s (the black lines) field lines meet at 90°. The coils are fed currents 90° out of phase. The grey lines illustrate the field lines meeting at 85°.

can be calculated from equations 2.73, 2.74, 2.75. ω_0 refers to the operating frequency, which is the same as the resonant frequency when working with RF coils. The applied phase shift can be designed by changing the component values.

$$C_p = \frac{1}{Z_0 \omega_0} \tag{2.73}$$

$$C_G = \frac{\sqrt{2} - 1}{Z_0 \omega_0} \tag{2.74}$$

$$L = \frac{Z_0 \sqrt{2}}{2 \omega_0} \tag{2.75}$$

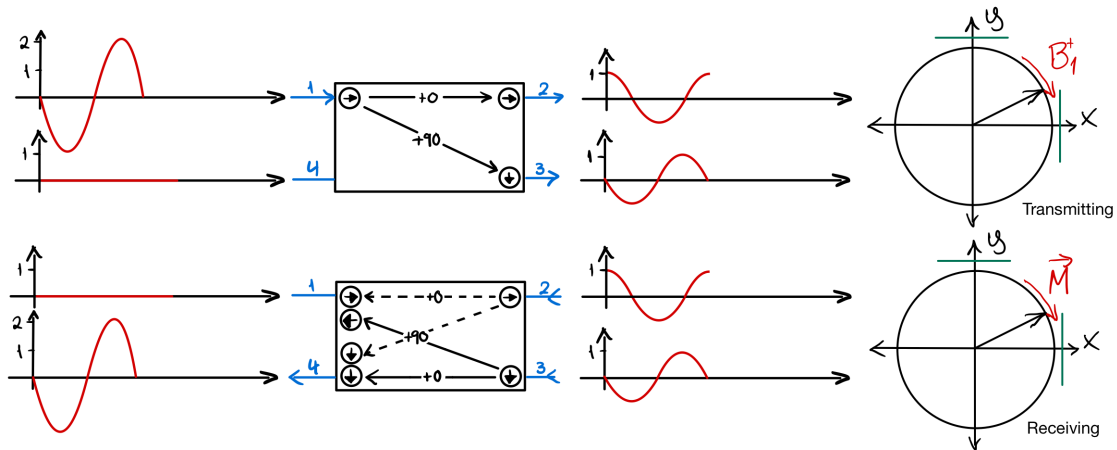


Figure 2.27: *The working principle of a 90° Hybrid.* – The working principle of a 90° Hybrid, upper part during transmission and the lower part during reception. Strongly inspired from Figure 5.1 in [50].

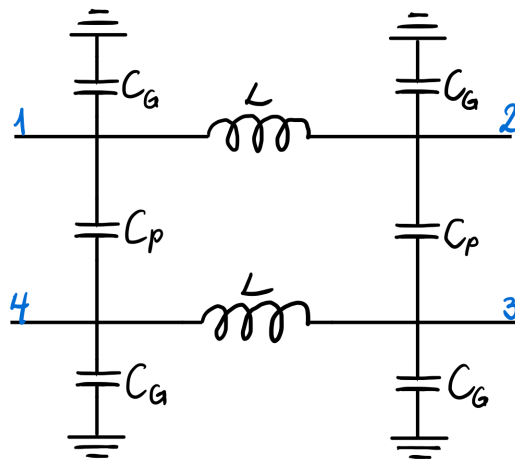


Figure 2.28: *The lumped element circuit for a $\lambda/8$ Hybrid* – Inputs and outputs are numbered in the same as in Figure 2.27.

2.6 Current knowledge

RF coil design for other nuclei than 1H is not as simple as changing the resonance frequency of the design. For example, the phased array is a typical design for a hydrogen RF coil, which achieves SNR values similar to a single surface coil but over a larger area. In a phased array, several wire loops are close to each other and decoupled so that signals can be gathered simultaneously and added together with weights depending on the sensitivity of the given voxels [86]. The realization of the high sensitivity of phased arrays for other nuclei than hydrogen is very challenging at magnetic fields of 3T and lower [13]. The challenges arise because lower gyromagnetic ratios result in lower resonance frequencies and hence higher RF losses in the sample, increasing the loaded Q-value and limiting the achievable Q ratio and sensitivity.

One approach to increase the sensitivity of a surface coil is to customize the shape of the wires to fit as closely as possible to the object being imaged [36]. Surface coils

provide a high SNR in the regions immediately adjacent to the coil and increase with a decreased coil radius. At the same time, the SNR of the surface coil falls off with distance from the coil, and this fall-off is steeper for smaller radii.

Surface coils produce an inhomogeneous B_1 field, but inhomogeneous fields can be corrected through image processing. A blurred version of the acquired MRI image can be divided into the original image to reduce the effects of an inhomogeneous B_1 field [98]. A more detailed mapping of the B_1 field can be established by using the Double-Angle Method (DAM) [99, 100]. DAM is a method for finding the flip angle of each voxel from two MRI images acquired with different flip angles. Adapting this method to imaging sequences with shorter TE makes it more applicable [101]. The field angle map can then correct for B_1 field inhomogeneities.

Taking advantage of a volume coil's circularly polarized magnetic field can increase the available signal for reception. This advantage is regularly used for hydrogen MRI with receive-only coils [85]. Phased array coils for hydrogen MRI are often placed inside birdcage coils decoupled during transmission, and this can also be done for ^{23}Na -MRI [13].

Using passive coil elements to enhance the magnetic field of a larger coil has been done with success in several MRI applications [102, 37]. The smaller coils can be called passive elements or secondary resonators because they are not directly connected to the power source of the MRI but inductively coupled to the other coil or coils in the experiment. A smaller secondary resonator was used to increase the sensitivity and homogeneity of a phased array coil inside a birdcage coil at 300 MHz [37]. The secondary resonator was decoupled during transmission to avoid negatively affecting the homogeneity of the transmit field.

Many RF coils for ^{23}Na -MRI are dually tuned because this allows more accurate co-registration [13]. A dually tuned coil can transmit and receive at the resonance frequency of ^{23}Na and the resonance frequency of hydrogen at a given field strength. In many applications, it is desired to have a hydrogen MRI scan as a reference image to the acquired ^{23}Na -MRI, and the most convenient way to do this would be to avoid an exchange of coils during the imaging procedure. However, the dual-tuning limits the possible coil sensitivity because the two resonators must work together [13].

2.7 Thesis motivation and aim

The potential applications of ^{23}Na -MRI are many but require more research. The possible spatial resolution of the available equipment determines the success rate of practical studies. Higher spatial or temporal resolution can be achieved with RF coils with a higher ^{23}Na -MRI sensitivity, but the available coils for typical ^{23}Na -MRI systems are limited.

This project aims to develop three single-tuned surface coils with increased sensitivity for ^{23}Na -MRI scans of a small volume in the back head, i.e., the visual cortex. These three coils have three different approaches to increasing the sensitivity:

- A single-loop coil - a single quadratic loop with two bent sides to fit the head shape. The favorable shape should result in an increased sensitivity [36, 103].
- An enhancing coil - a single quadratic loop with two bent sides like the single loop coil to fit the human head. This loop will be a secondary resonator placed inside a birdcage coil to enhance the magnetic field in the visual cortex during the reception. This enhancement during reception is expected to increase sensitivity [37, 38].
- A quadrature coil - two quadratic loops with two bent sides, each loop resembling the single-loop coil, operated in quadrature. A circularly polarized magnetic field and the favorable shape are expected to increase the SNR by a factor of $\sqrt{2}$ [35].

These coils will be compared with two general-purpose surface coils and a birdcage coil. The developed coils will be compared to each other and the available coils through laboratory evaluations and MRI scans using a uniform phantom.

Chapter 3

Methods

In order to design and evaluate the feasibility of the three proposed technical developments, it is helpful to calculate the magnetic fields around the RF coils and simulate the electrical properties of an RF-circuit. The coil designs were restricted by the MRI gantry, and appropriate holders to mount the coils needed to be developed. This chapter describes various coil designs and the laboratory and MRI settings used to evaluate them.

3.1 3D printed coil holders

The software Fusion 360 (v.2.0.18719, Autodesk, San Francisco, USA) [104], is an integrated cloud software platform for Computer Aided Design (CAD), Computer Aided Manufacturing (CAM), Computer Aided Engineering (CAE), and Printed Circuit Board (PCB). This tool aided in creating digital models of three-dimensional objects through CAD design. The models were exported as Stereolithography (STL) files for 3D printing. The three coils (described below) required two different coil holder designs. The enhancing loop holder needed to fit inside the birdcage coil, while the stand-alone coil holders for the single-loop and the quadrature coils needed support structures to stand alone on the MRI table. Both designs needed to be comfortable for the patient's head.

The inner diameter of the birdcage coil was measured with a ruler and used to create the initial sketch of the enhancing holder in Fusion 360. A ball to indicate the size of a head was also sketched. The holder was made hollow and high enough to make room for a reasonably thick material and the coil components underneath a head. Support was added in the middle and along the sides of the coil holder to make it stable enough to support the weight of a human head.

The holder for the single loop coil and the quadrature coil required fitting to the MRI table and comfort for the patient. The curvature of the MRI table was found by using the 3D scanner app called Scaniverse to scan the underside of a hydrogen receive coil for the MRI system "Discovery MR750" from GE. The resulting 3D model, a 3D

mesh covering the surface underneath the RF coil, was imported to Fusion 360 as shown in Figure 3.1, and the curve of the MRI table was sketched from this mesh. The neck support of the coil was designed by measuring the distance between a person's neck and the ground while resting on the ground. The underside where the coil components were to be attached had to be smooth curves to avoid inflicting strain on wires and cables. For a durable coil, it is essential not to damage the wire tubing.

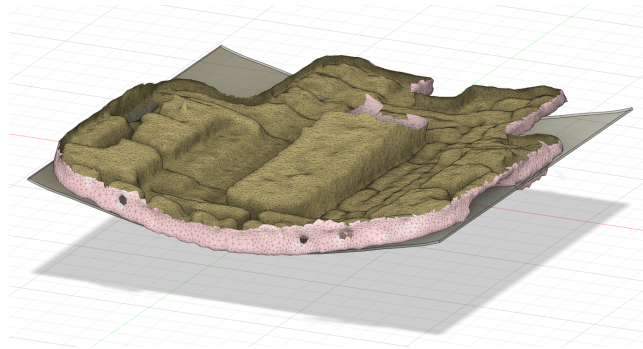


Figure 3.1: 3D scan of a GE coil's underside imported to Fusion 360 – Screenshot from Fusion 360 of a 3D mesh (pink) of an MRI receive coil turned upside down. The mesh was created by the 3D scanner application Scaniverse and imported into Fusion 360.

3.2 Magnetic field calculations

A Python package called Magpylib [75] was used to calculate the static magnetic fields around the coil wires. This package integrates the Biot Savart equation (Eq. 2.37) and provides vector field visualizations through various Python libraries. It was developed to aid magnetic system design processes [105]. As part of this thesis, a customized Python class called "MRIcoil" was created; see Appendix A. Nevertheless, due to reduced computational requirements, many of the final plots in the results section were generated using Magpylib directly. The MRIcoil class was instrumental in getting an overview of the immediate field properties of a design in the early stages of this project.

Different approaches for mimicking the curvature underneath the coil holder were investigated. In the early stages, only flat coils were considered. With finished 3D-modeled coil holders, the enhancing coil holder was imported from an STL-file as a 3D mesh in Python. To extract coordinates of the holder's undersurface proved computationally heavy and was later aborted. Mimicking the curve by calculating the 2D coordinates of a quarter circle with the same radius used in the 3D designs required far less computational time. These points in 2D were first defined in the first quadrant and then rotated to the center of the third and fourth quadrants. The curves of both holders were mimicked in this way. Different shapes for the single loop coil were constructed by defining lines in 3D coordinates and feeding them to Magpylib as current lines.

The idea for the enhancing coil was to have the same field of view as for the single loop coil, so the simulation for this alone is the same. The head coil available for the GE scanner is a dual-tuned 16-rod birdcage coil from RAPID Biomedical with approximately the same radius as the one simulated in the static magnetic field calculation in

Figure 2.22. Figure 2.21 shows an image of this coil. The circularly polarized field produced from the birdcage coil will induce a current in the enhancing coil. As the field rotates, the component perpendicular to the enhancing coil changes from increasing to decreasing, changing the current direction in the enhancing coil. The change of magnetic flux through the enhancing coil area was calculated approximately and used to calculate the induced current in the enhancing loop using Faraday's induction law (Eq. 2.29). The currents in the rods of a birdcage coil were set according to equation 2.60. The rotational field lines were simulated by changing the phase factor from 0 to 2π in 10 steps. The field component perpendicular to the enhancing coil along a central line was averaged and stored. The derivative of the magnetic flux Φ_B and hence the induced emf (Eq. 2.29) was calculated by dividing the difference in perpendicular field components between two consecutive moments with the time between moments. The calculated emf was used to define a current in the enhancing coil, and then Magpylib calculated the magnetic field of the birdcage coil and the enhancing coil.

For the quadrature coil, the curve mimicking the underside of the coil holder was parted into two arrays overlapping in the middle. Two squares with arcs at two sides were constructed along the curvature. These two traces of square loops were modeled in Magpylib and simulated as current lines. The current in the two segments was chosen using a sine function and two angles separated by 90° . By choosing eight such pairs of current amplitude from a sine wave cycle, it was possible to illustrate the circulating nature of the magnetic field.

3.3 RF circuit simulation

The simulation tool LTspice (17.1, Analog Devices, Wilmington, USA) [106] was used in the early stages of the project to simulate the electric properties of an RF circuit. LTspice is short for Linear Technology with Integrated Circuit Emphasis.

The losses in the coils are challenging to simulate perfectly because they arise from internal losses of the components and losses in soldering connections. Small losses significantly affect RF circuits with resonance modes at high frequencies. However, such simulations can estimate the required capacitance values to make a loop structure resonate at the desired frequency.

Simulations with LTspice were done for a circular single-loop surface coil, but additionally, a more experimental trial-and-error approach was used. The experimental approach was possible because of the wide range of good quality non-magnetic capacitors and other equipment like high quality VNAs were available during a visit to the Max Planck Institute of Clinical Cybernetics in Tübingen, Germany.

3.3.1 Considerations for the Medical Device Regulation

All devices used for medical purposes are regulated by the European Council's directive called the Medical Device Regulation (MDR). These regulations include directions on how a medical device should be documented for marketing and recommended stan-

dards for in-house devices. Article 2 (1) in MDR [107] defines an article intended for human beings with the medical purpose of diagnostics as a medical device. At the same time, Article 5(5) states that "the requirements of this Regulation shall not apply to devices, manufactured and used only within health institutions established in the Union, provided that following conditions are met:..."[107]. These conditions are better described in Annex 1: "General Safety and Performance Requirements".

Additional requirements are listed for electronic equipment interacting with the human body. The MDR specifies in Annex 1 chapter 1(8) that "All known and foreseeable risks, and any undesirable side-effects, shall be minimized..." [107]. When designing an RF coil for MRI examinations of humans, the wires should be adequately shielded from the human skin, and the coil Specific Absorption Rate (SAR) should be assessed. Safety measures should be installed to avoid a SAR exceeding normal limits. Such a safety measure can be a fuse, breaking the circuit at a particular current level. In the current thesis, only results from phantom imaging are presented. In vivo imaging would require risk assessment and ethical approval.

The material used for 3D printing was chosen carefully with the MDR regulations in mind. 3D printed devices in contact with human skin need to be made in a material that can be easily cleaned repeatedly and does not irritate the human skin. Materials like Polylactic Acid (PLA) and Polyethylene Terephthalate Glycol (PET-G), a glucose-moderated PET, are typical material compositions for 3D printer filament. PET-G are especially robust against repeated disinfections, but PLA will also endure many disinfections. 3D printed objects should be stored dry to maintain their strength. The magnetic susceptibility values of these materials are given in Table 2.3 and should not be prone to eddy currents.

3.4 Design 1: Single-loop coil

A circular surface coil was the initial idea, but while it is easy to imagine a circular coil, it is easier to form a square coil from a thick copper wire. The square side length depends on the desired maximum penetration depth and was calculated by comparing a square's area with a circle's area.

Distribution of capacitors is another design choice where the advantages and disadvantages must be balanced. One capacitor is enough to achieve the correct resonance frequency. However, the voltage across each capacitor is lower if the number of capacitors is higher, given that they are distributed equally around the coil wires. A lower voltage in the coil results in a weaker electric field around the wires, limiting losses through electric coupling, which will increase the Q value of the coil. At the same time, several capacitors will introduce more resistance and noise to the circuit as each capacitor comes with an inner resistance, and the connection of another capacitor involves soldering. It was decided to use two capacitors to distribute the voltage.

A matching circuit is required to connect the coil to the MRI system. Inductive solutions were quickly discarded as they are hard to work with under the conditions of an MRI experiment. It was decided to attach a connecting line and ground across

one of the two distributed capacitors in the loop. This results in a parallel resonator, and the L-network for a parallel resonator of figure 2.25 was chosen for the matching circuit. This matching network was chosen to increase the Q-value of the coil [91] and balanced to avoid common mode currents down the transmission line.

Figure 3.2 presents the circuit diagram of the final design, which includes a matching circuit resembling the one presented in Figure 2.25, but now balanced. Notice that the variable tuning capacitor is parallel to the capacitor furthest away from the matching circuitry to limit the two variable capacitors' influence on each other. The matching circuitry also includes a variable capacitor.

A coil was constructed based on this circuit diagram. The first connection of all components was made with an arbitrary but balanced capacitance in the wire gaps. By measuring this prototype's resonance frequency, the wires' inductance was calculated through equation 2.52, rewritten to equation 3.1. Inserting this in another rewrite of the same equation with the desired resonance frequency of the loop approximated the total capacitance needed in the resonator by equation 3.2. To distribute the capacitance equally between two positions, the capacitance required for each capacitor was twice the calculated value; see equation 2.48. A resonance frequency close to 33.78MHz was achieved through trial and error.

$$L = \frac{1}{(2\pi f_0)^2 \cdot C} \quad (3.1)$$

$$C = \frac{1}{(2\pi f_0)^2 \cdot L} \quad (3.2)$$

The loaded Q ratio of the approximately tuned loop was found using equation 2.67 and a double loop pick-up probe connected to a VNA with a phantom placed close to the coil. The Q ratio was used to calculate the resistance of the coil through equation 2.62. Then, all was in place to calculate the capacitor values for the matching circuit through equation 2.61. A variable capacitor was included to make the matching adjustable. When the first capacitive matching components were connected, the S_{11} parameter was measured through a transmission line connected to the VNA. The tuning and matching were changed and monitored from the S_{11} measurement and the input impedance from the Smith chart presented on the VNA. The goal was a resonance frequency of $f_0 = 33.78\text{MHz}$ and an input impedance of $50\Omega = Z_0$ at this frequency under loading.

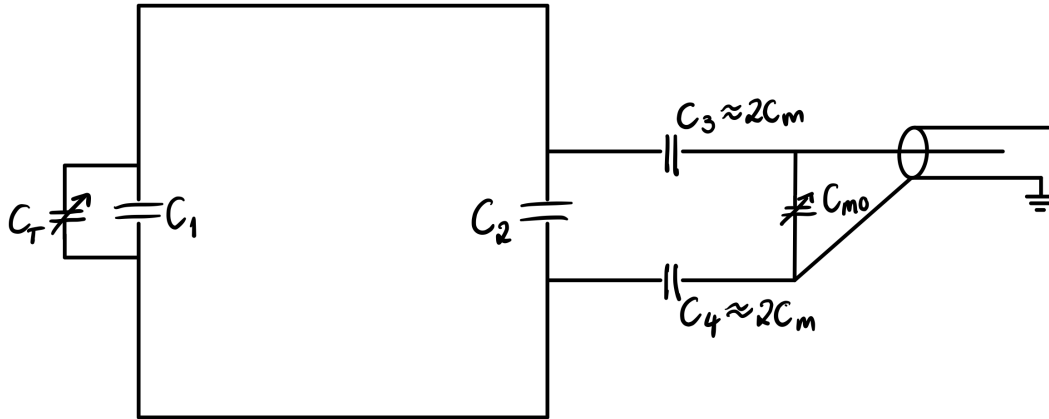


Figure 3.2: *Electronic schematic of the single-loop coil design.*

3.5 Design 2: Enhancing coil

A comparably small secondary resonator inside a volume coil will not interact enough to create new modes for the combined system but enhance the field of the volume coil close to the small coil [37, 38]. The advantage of the circularly polarized, homogeneous field inside the head coil is kept, but a higher image resolution can be achieved in a small ROI.

The smaller coil will be inactive during transmission to maintain the homogeneity of the transmission field. The enhancing coil was detuned at high-induced voltage using crossed diodes with a threshold value higher than the current induced in the coil during reception. The field produced by the head coil during transmission is much stronger than that produced by the magnetized sample during reception. Using the circuit drawing for the single-loop coil as inspiration and adding a parallel resonating circuit with the crossed diodes resulted in the circuit drawing of Figure 3.3.

This coil cannot connect to a VNA, so to measure the resonance frequency, a magnetic field probe can be used to couple inductively to the coil during a frequency sweep with the VNA. A shielded magnetic field probe was made from detailed instructions provided by Oxford professor Douglas C. Smith [108].

The approach for constructing the enhancing coil was the same as for the single-loop coil without the matching circuit. The required inductance for the detuning circuit was calculated from equation 3.1, using the value of capacitor C_{E2} , which will be part of the detuning circuit. An inductor was made by folding a tin-plated copper wire around a drill bit to get a fixed diameter of the turns. A table based on empiric measurements was used to estimate how many turns and how large their diameter should be to arrive at an inductance close to the calculated one. The wire turns were spread to avoid short circuits. The inductance was measured by soldering a capacitor of arbitrary value across the wire ends, measuring the S_{12} across the capacitor, finding the resonance frequency of the RF circuit, and using this frequency in equation 3.1. A detuned coil will resonate at a different frequency than 33.78MHz , i.e., have an S_{11} magnitude of

0dB at 33.78MHz.

The high-power diodes were installed after a proper detuning was established. The diodes were mounted in opposite directions, forming the crossed-diode structure in the detuning circuit. The frequency was measured again using the single-loop probe to see how adding the detuning circuit affected the resonant frequency. Tuning was performed to make the coil resonate close to 33.78MHz when the diodes of the detuning circuit were closed.

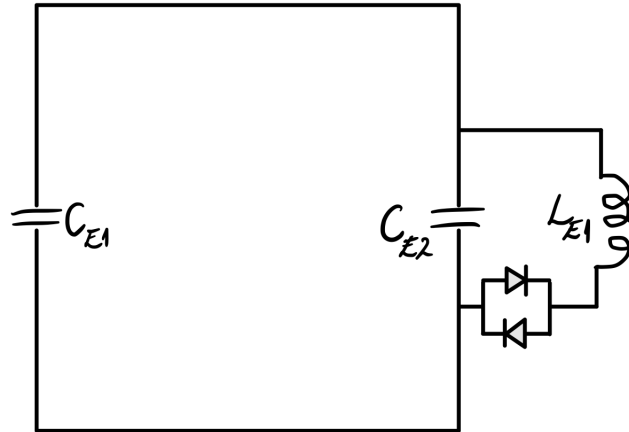


Figure 3.3: *Electronic schematic of the enhancing coil design.*

3.6 Design 3: Quadrature coil

The advantages of quadrature driving can be achieved by combining two surface coils. The quadrature surface coil proposed as part of the current thesis would not be optimized to assure good homogeneity because all the field harmonics are left uncanceled. However, a circularly polarized magnetic field will be produced during transmission for a small region where the field lines from the two coil elements interfere at a 90° angle. An increase in SNR by a factor of $\sqrt{2}$ during signal reception is expected [35]. Bringing two coils similar to the single-loop design close together will lead to interaction through mutual inductance. The coil elements can only be independently tuned if they are decoupled, and overlapping the area of the two coils provides inductive decoupling. A 90° Hybrid, detailed in the next section, was chosen as a power splitter and signal combiner.

By combining the circuit drawing of the single-loop coil in Figure 3.2 and the typical circuit of a Hybrid in Figure 2.28, the circuit in Figure 3.4 were proposed for the quadrature coil. An unnamed inductor between the loops indicates the overlap or inductive decoupling.

Two quadratic loops similar to the single-loop coil were mounted underneath the second stand-alone coil holder, bending with the curvature. The inductive decoupling was assumed to require an overlap of approximately 15% of the side length. Loop

capacitors and matching circuitry were installed in the same manner as for the single-loop. Two of the quadratic loop halves were parted in three pieces of tinned copper wire to allow adjustment of the loop overlap after installation. A strip of PCB glued to the coil holder connected the corners and the straight wires. The width of this PCB strip constrains the possible overlap adjustment. One of the wire corners at the overlap was slid into an isolating plastic tube to avoid a short circuit between the loops. Each loop was tuned and matched separately by removing the straight piece of the overlapping half in the other loop to make it less inductive.

Decoupling the coil elements was done by monitoring the S_{12} and S_{21} while the coils had all their pieces in place, and both coil elements were connected to the VNA. The overlap was adjusted until the lowest through parameter at the desired resonance frequency was found.

The finished coil is a two-port device, and to measure the S-parameters, the two ports of the VNA must be connected to each coil's matching circuit. The Hybrid must be detached for this measurement, and SubMiniature version A (SMA) connectors were installed between the matching circuit and the Hybrid to facilitate this.

3.6.1 The Hybrid

A Hybrid will provide the 90° phase shift between the two current sources. A 90° Hybrid fitted the MRI-system used in this thesis because the T/R switch has an adapter with one coaxial cable for transmission and another for reception.

The components needed for a Hybrid of 90° phase shift at a given frequency can be estimated from equations 2.74, 2.73 and 2.75 [109]. These equations can be expressed more simply by using the known values of angular frequency $\omega_0 = 2\pi \cdot f_0$ and the characteristic impedance $Z_0 = 50\Omega$. By correcting for units, the capacitance of C_p and C_G in pico Farads and the inductance of L in micro Henrys can be found from equations 3.3, 3.4 and 3.5.

$$C_p[pF] = \frac{3183}{f_0} \quad (3.3)$$

$$C_G[pF] = \frac{1318}{f_0} \quad (3.4)$$

$$L[uH] = \frac{5627}{f_0} \quad (3.5)$$

The Hybrid was made on two small plates of PCB stacked with the central part of the top plate connected to the bottom plate defining ground. The top plate has several separate copper-covered parts to facilitate the connections of all Hybrid components. Capacitors with the calculated values and inductors made with calculated inductance were connected to the PCB following the circuit drawing in Figure 2.28.

By interchangeably measuring the isolation between the same side ports and the isolation between ports on opposite sides, the isolation between the same side ports was made as good as possible, aiming for at least $-30dB$, and the through parameter of the opposite side ports was made $\approx -3dB$. These adjustments were done by pushing and pulling the wire turns of the inductors.

Four measurements had to be made to measure the phase difference provided by the Hybrid. During transmission, the transmission line named "Tx" in the circuit drawing of Figure 3.4 is assumed to be connected. The interesting measurements for establishing the phase difference are the through parameter, i.e., S_{12} or S_{21} , when the "Tx" cable is connected to port one of the VNA, and port two, is connected, first to one of the connections on the opposite side of the Hybrid, and then to the other. The difference in measured phase between these two measurements is the phase difference provided by the Hybrid during transmission if the "Tx" connector is used for transmission. Since the Hybrid is a symmetric device, the "Rx" connector could just as well be the one connected to the transmission, so the phase difference provided by this connector was also measured. Which connector should be connected to transmit and which should be connected to receive was found through imaging with the MRI machine.

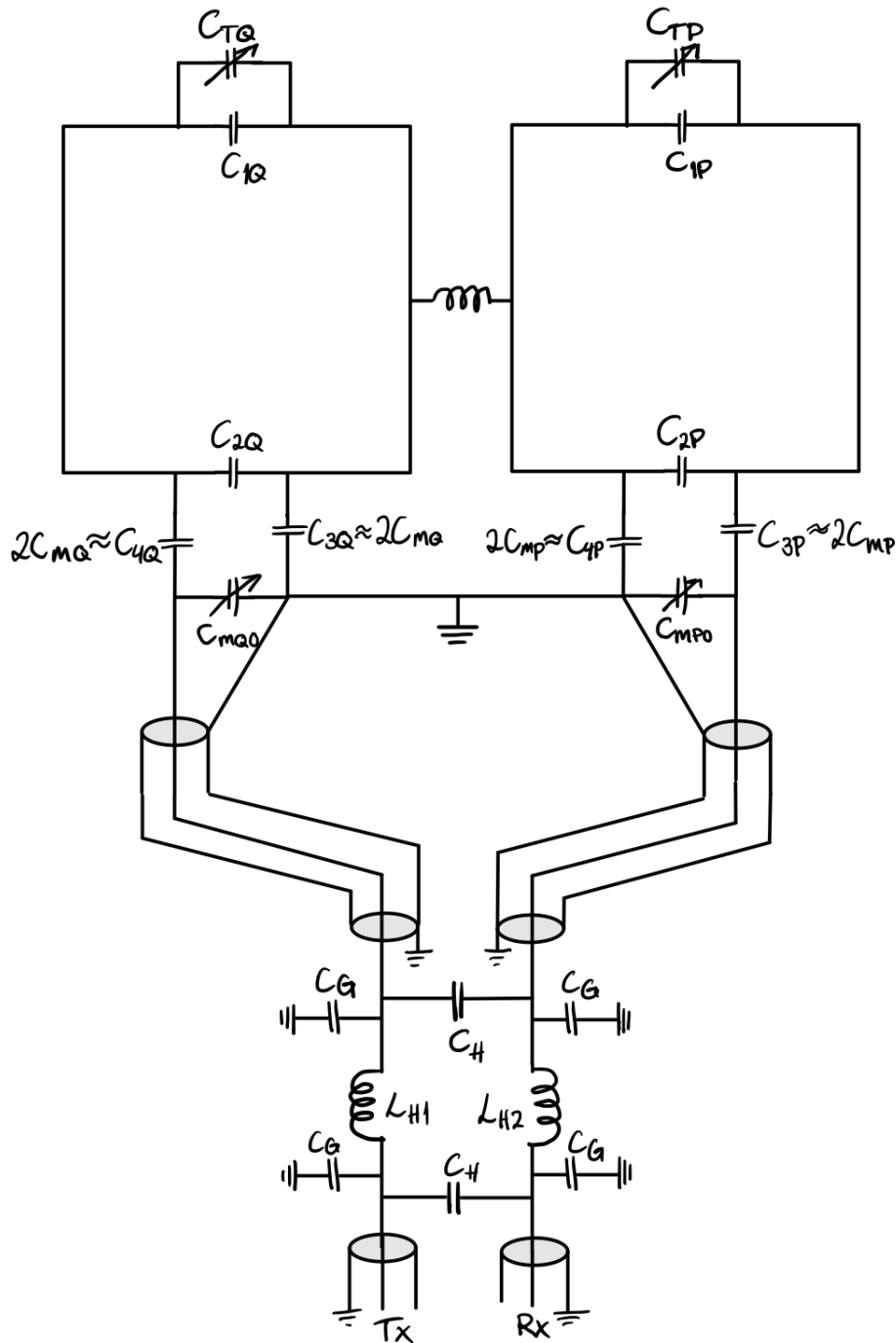


Figure 3.4: Electronic schematic of the quadrature coil design.

3.7 Laboratory evaluations

The final S-parameter measurements were made using a pocketVNA (2.10, pocketVNA, Neubeuern, Germany), and the measurements were stored as touchstone files. S-parameter plots were created by averaging over ten measurement series spanning the $(33.78 \pm 2) \text{ MHz}$ range with 1001 measuring points. The coil was placed on top of a 10 cm thick foam to avoid RF loss in the surroundings. Ten measurement sweeps were

done for all coils under loaded and unloaded conditions. The Q ratios of the coils were found by calculating the coils loaded and unloaded Q factors following equation 2.64 for each of the two measurement conditions. The presented uncertainties are based on the standard deviation of the ten measurement series. Calculations of averages, standard deviations, Q ratio, and impedance were performed using Python. The Python code used for these calculations can be found on GitHub; see Appendix A.

Two available surface coils were included in the project to provide a comparison. One will be called "Prior Design One" and the other "Prior Design Two". These two are presented in Figures 3.5 and 3.6, respectively. Both coils are general-purpose surface coils with a flat circular shape.



Figure 3.5: *Picture of the Prior Design One surface coil*

3.8 Phantoms

Several phantoms were considered before a phantom was chosen for the final measurements. Early in the process, a Hoffman phantom mimicking a human brain shape seemed to be a good choice, which influenced the designs of the 3D coil holders. However, this phantom was not used because of concerns about its weight on the coil holders and the possibility of damaging the phantom using saline water. During the visit to Tübingen, an acrylic container shaped like a cylinder filled with a water solution mimicking the properties of human tissue was used.

After returning from traveling, a phantom had to be found for imaging with the MRI. A phantom of 2% agar gel was made with an agar concentration chosen according to the expected concentration of agarose to produce correct T_2 relaxation times for grey and white matter [110]. Agar and agarose are different, but agar was more readily



Figure 3.6: Picture of the Prior Design Two surface coil

available. This agar gel, edible jello, ketchup, and water were all tried for preliminary measurements but had variable success in mimicking the properties of human tissue. Tubes of agar gel with known ^{23}Na concentrations were also used. Many of these phantoms were small compared to a human head and contained air-filled volumes undesirable in an MRI experiment.

The chosen phantom from Siemens was borrowed from the Radiology department at Haukeland University Hospital. The phantom is a plastic bottle of 1900 ml volume filled with a liquid solution of $3.75\text{g NiSO}_4 \times 6\text{H}_2\text{O} + 5\text{g NaCl}$ per $1000\text{g H}_2\text{O}$. Figure 3.7 provides a picture of the chosen phantom used to load the coil for all laboratory measurements and for imaging with the MRI to evaluate all the coils in this thesis.

3.9 MRI acquisition and image processing

All coils were used to acquire three ^{23}Na -MRI scans with a radial CN UTE sequence. The scans had different combinations of sequence settings concerning the number of readouts, resolution, and k-space sampling. The three pulse sequences' names include the total amount of readouts and are summarized in Table 3.1. The image reconstruction for the CN-197 sequence involved an interpolation from $4.5 \times 4.5 \times 4.5$ mm to $2 \times 2 \times 2$ mm resolution because of the different reconstruction matrices. The MRI images presented in this thesis are absolute magnitude values of the Fourier-transformed signals. For each image, the pixel values are normalized to the maximum pixel value of the specific image.

All MRI images have scanned the selected phantom displayed in figure 3.7. The



Figure 3.7: *Picture of the chosen MRI phantom* – This phantom produced by Siemens Healthineers contains a liquid solution of $3.75\text{g NiSO}_4 \times 6\text{H}_2\text{O} + 5\text{g NaCl}$ per $1000\text{g H}_2\text{O}$ and was used for coil loading during laboratory tests and phantom imaging.

Bloch Siegert optimization method was used to find the correct resonance frequency setting for the scanner [111].

Scans were performed with the birdcage coil to enable comparison. The enhancing coil scans were performed with the phantom centered at the bottom of the curve inside the birdcage coil, with the phantom resting on the enhancing coil. All MRI images acquired with the birdcage coil had a transmit gain set to 50. Scans done without the birdcage coil had a transmit gain set to as low as possible.

Table 3.1: Overview of MRI pulse sequence scanning parameters used in this thesis.

	Readouts	Resolution (mm ³)	k-space sampling	Acquisition time (min:sec)	TR	Recon matrix size
CN-197	197	4.5x4.5x4.5	10%	0:20	100ms	120
CN-1402	1402	3x3x3	12%	2:20	100ms	80
CN-2552	2552	3x3x3	25%	4:15	100ms	80

3.9.1 Correction for B1 field inhomogeneities

Two approaches were attempted to correct for the unavoidable inhomogeneities in the B_1 -field for surface coils. The first one divides the original image by a blurred version of itself [98]. The operation is expressed mathematically in equation 3.6 where "*" indicates convolution, F is a normalized version of the original image, $K_{(3 \times 3)}$ is the blurring kernel of size (3×3) , and J is the blurred version of F . The blurred version enhances regions of weaker signals in the original image. All background pixels turn white by applying the blurred version directly, as the mathematical expressions imply. The blurred version was masked, setting all values below 0.15 to one to avoid the white background. See the implementation in the GitHub repository linked in Appendix A. A circular mask enclosing the entire phantom was tried as a mask of the region where the phantom should be, but the signal acquired by the surface coils did not reach through the entire phantom.

$$F * K_{(3 \times 3)} = J \quad (3.6)$$

$$F/J = F_{corrected}$$

The other inhomogeneity correction method involves mapping the B_1 -field. A simple method for acquiring this B_1 -field map is the Double-Angle Method (DAM) [99]. DAM requires two images with flip angles of α and 2α . The equation for calculating the flip angle map θ is shown in equation 3.7, where S_α and $S_{2\alpha}$ refers to the signal intensity from the image acquired with flip angles α and 2α , respectively. The images should be acquired with a long TR to eliminate the effect of T_1 relaxation, but the ^{23}Na -MRI scans acquired in this study have a short TR. Fortunately, this effect can be corrected by multiplying the image by a correction factor found with equation 3.8 involving the applied flip angle, the TR used in the scan, and the T_1 of the sample matter [101]. The original signal of S_α and $S_{2\alpha}$ was multiplied with the correction factor before the values were put into equation 3.7 to yield the flip angle map called θ . The image was corrected by equation 3.9, where F is the original image, F_{corr} is the corrected image, and θ_{norm} is the flip angle map normalized to $\frac{\pi}{2} \text{rad} = 90^\circ$.

$$\theta = \cos^{-1}\left(\frac{S_{2\alpha}}{2 \cdot S_\alpha}\right) \quad (3.7)$$

$$S_{inf}/S_{TR_x} = \frac{1 - \cos(\alpha) \cdot e^{-\frac{TR_x}{T_1}}}{1 - e^{-\frac{TR_x}{T_1}}} \quad (3.8)$$

$$F_{corr} = F/(1 - \theta_{norm}) \quad (3.9)$$

3.9.2 Data analysis and evaluation

Data from MRI experiments were handled in in-house developed Python code. Magnitude images were created using the "abs" function. The SNR values were calculated based on these magnitude images by defining separate areas of uniform noise and uniform signal in the images according to instructions by National Electrical Manufacturers Association (NEMA) [93]. The pixels from the defined areas were used to find an average signal and a noise standard deviation to put into equation 2.70. The areas with approximately uniform signals were chosen by placing the bottom of a 7x7 pixel square two rows of pixels into the phantom. The areas with approximately uniform noise were chosen by placing the top of an 11x11 pixel square three rows of pixels under the phantom. The phantom limit was found by visual inspection of the MRI images. The sizes of the pixel squares were chosen according to recommendations from NEMA [93].

Three intensity plots of vertical lines from the three different scan settings, CN-197, CN-1442, and CN-2552. The lines are centered in the signal squares used to calculate SNR. Three intensity plots of the central horizontal line in the signal squares were also made. A threshold of 0.4 normalized magnitude was used to align the lines in each plot by marking the entrance of the phantom for all plotted lines. The coils' sensitive region was defined by requiring the signal intensity above 50% of the maximum signal in the imaged slice. This threshold is indicated in all line plots.

Chapter 4

Results

4.1 Designs and visualizations

4.1.1 3D printed coil holders

3D designs of coil holders were made using Fusion 360. The final 3D designs with some reference structures were exported as images and presented in Figures 4.1 and 4.2, where the holders have an orange color. Two identical stand-alone coil holders for the single-loop and quadrature coils were printed using PLA filament, while the enhancing coil holder was printed in PET-G filament. The finished 3D printed enhancing holder is shown in Figure 4.8, and the two copies of the stand-alone coil holder are shown in Figures 4.10, and 4.13.

4.1.2 Visualizations of magnetic field

Visualizations of the static magnetic field calculations performed with Magpylib are shown in Figures 4.3, 4.4, and 4.5, for the enhancing, single-loop and quadrature coils, respectively. All three figures consist of three subfigures: a three-dimensional model of the current line configuration defined in Magpylib (a), a magnitude plot of the magnetic flux density in plane $z=0$ (b), and a field line plot of plane $z=0$ (c).

The field lines of the single-loop coil in Figure 4.3 (c) are most straight in the middle of the coil. The field magnitude around the single-loop coil in Figure 4.3 (b) falls off with distance from the wires.

The circularly polarized field of the quadrature is not evident from the static magnetic field calculation in Figure 4.5. The field magnitude falls off with distance from the coil, and the magnetic field seems less homogeneous than for the single-loop coil judging by the field line plot in figure 4.5 (c). A visualization of the circularly polarized field of a quadrature coil is shown in Figure 4.6. The field line section displayed in Figure 4.6 shows the center square of plane $z=0$ from approximately one centimeter above

the wires to six centimeters above the wires and approximately five centimeters wide. By visual inspection, the field seems homogeneous for a square of two centimeters side length in the middle of this section.

Figure 4.4 (b) and (c) show that the enhancing coil affects the homogeneity of the birdcage coil's magnetic field, which was shown in Figure 2.22. A visualization of the circularly polarized field of the birdcage coil with the enhancing coil inside is shown in Figure 4.7. The coil configuration is the same as in Figure 4.4 (a). The field appears enhanced on one side but weakened on the other side of the enhancing coil. These effects remain at the same respective sides throughout the cycle, except when the field lines inside the coil are oriented vertically. For vertical field lines, the enhancement is symmetric in the lower middle of the volume inside the birdcage coil.

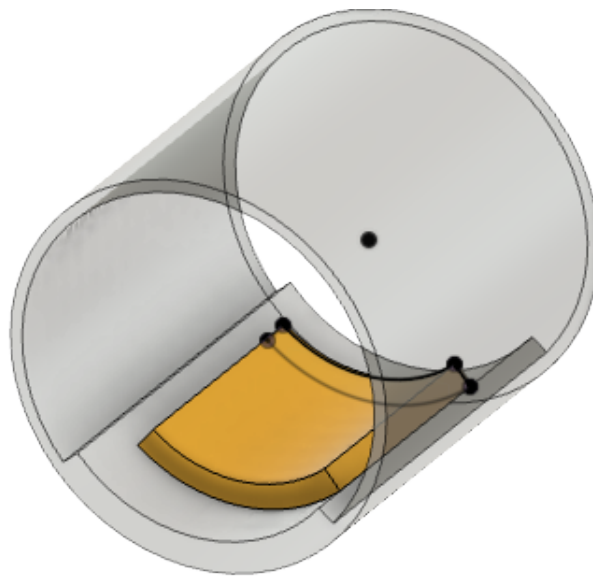


Figure 4.1: *Image of the 3D-designed enhancing coil holder* – This screenshot captured in Fusion 360 shows the Enhancing coil holder designed to fit inside a birdcage coil.

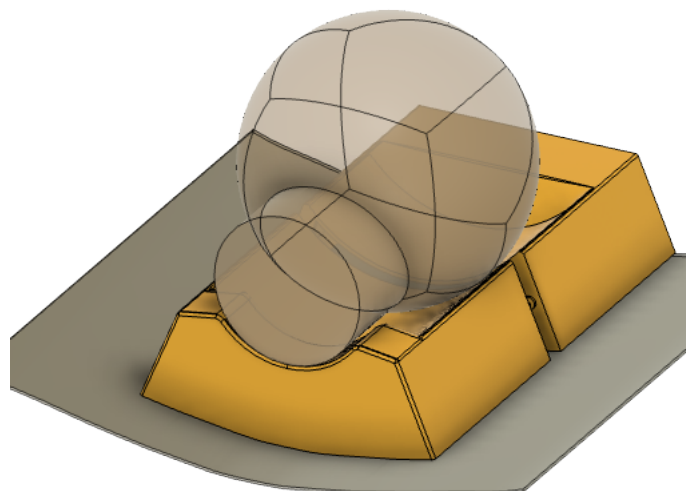
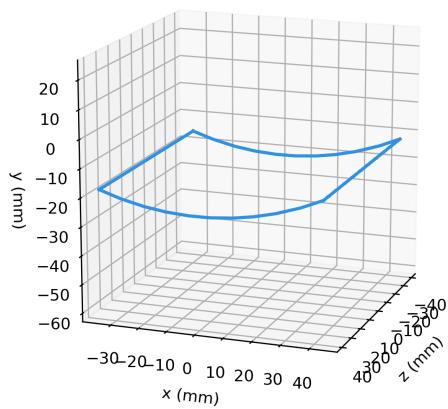


Figure 4.2: *Image of the 3D-designed stand-alone coil holder* – This screenshot was captured in Fusion 360 and shows the coil holder designed to stand alone on the MRI-table and function as a headrest.



(a) Current lines of the single-loop coil.

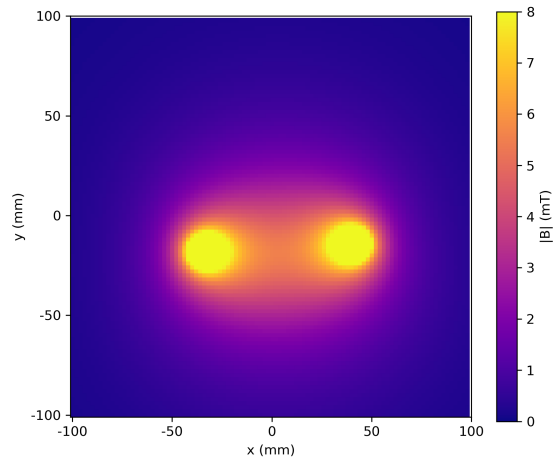
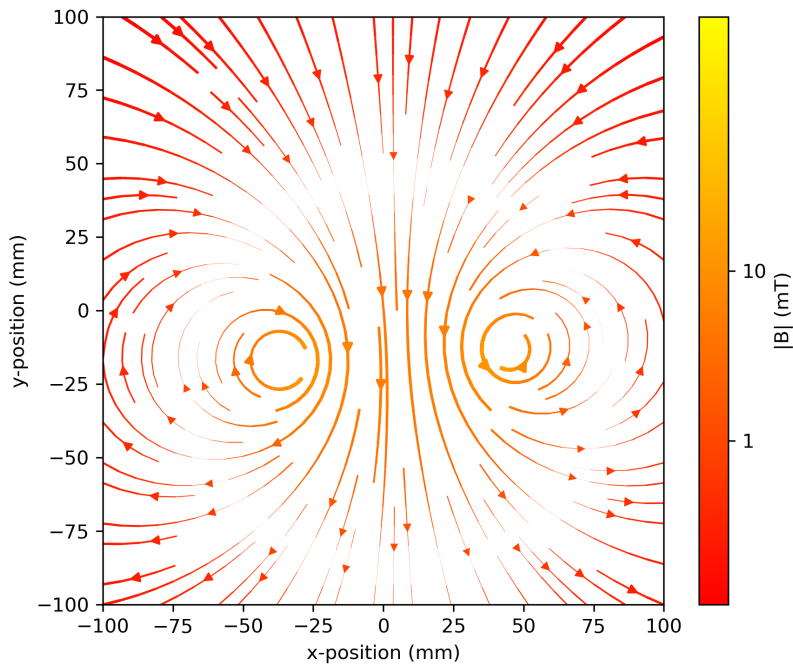
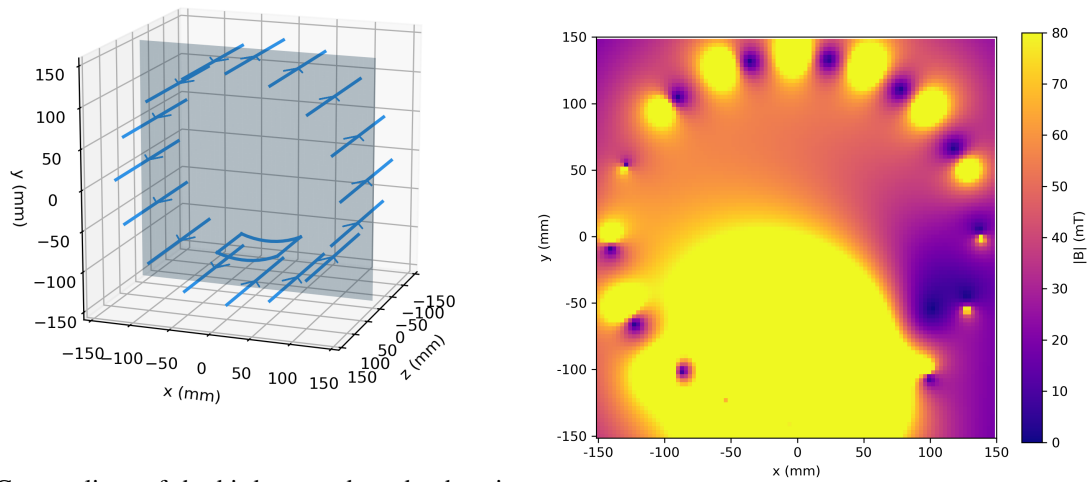
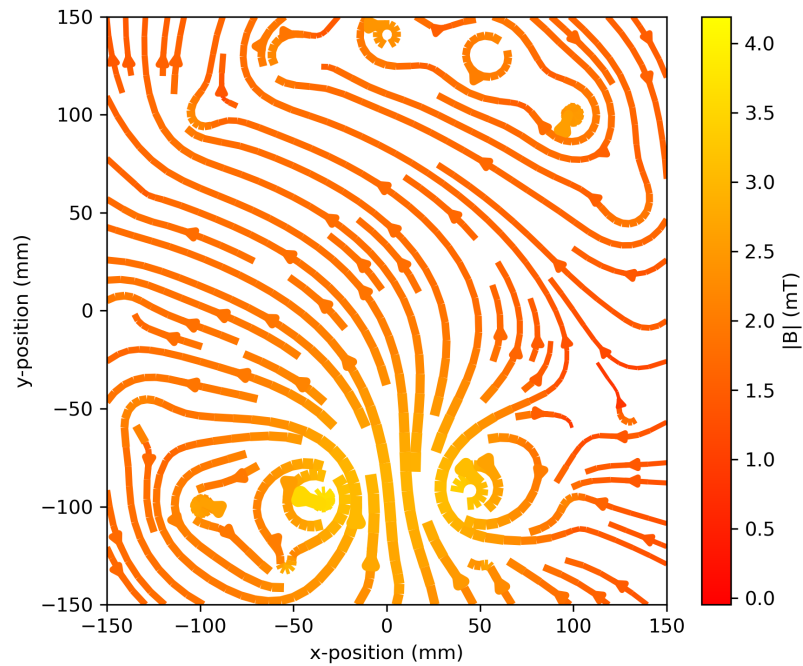
(b) Field magnitude in plane $z=0$.(c) Field lines in plane $z=0$.

Figure 4.3: *Visualization of the magnetic field around the single-loop coil* – Static field calculations for the single-loop coil using the python library Magpylib [75]. The position of the single-loop coil is shown in a), the magnitude of magnetic flux density in plane $z=0$ is shown in b), and the field lines of the same plane are shown in Figure c).



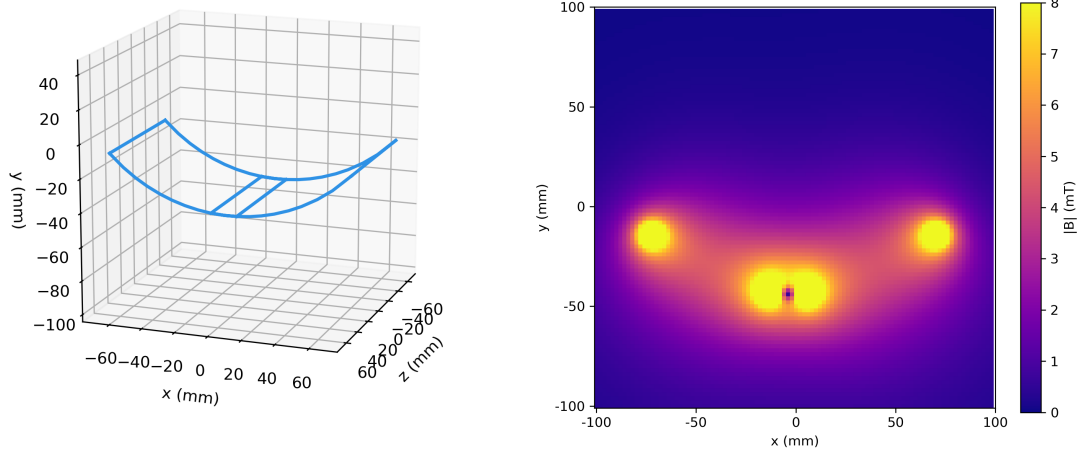
(a) Current lines of the birdcage rods and enhancing coil.

(b) Field magnitude in plane $z=0$.



(c) Field lines in plane $z=0$.

Figure 4.4: Visualization of the magnetic field around the enhancing coil – Static field calculations for a birdcage head coil with 16 rods/legs with the enhancing coil inside using the python library Magpylib [75]. The orientation of the enhancing coil inside the birdcage coil is shown in a), including a plane indicating where position $z=0$. The magnitude of magnetic flux density in plane $z=0$ is shown in b), and the field lines of the same plane are shown in Figure c).



(a) Current lines of the quadrature coil.

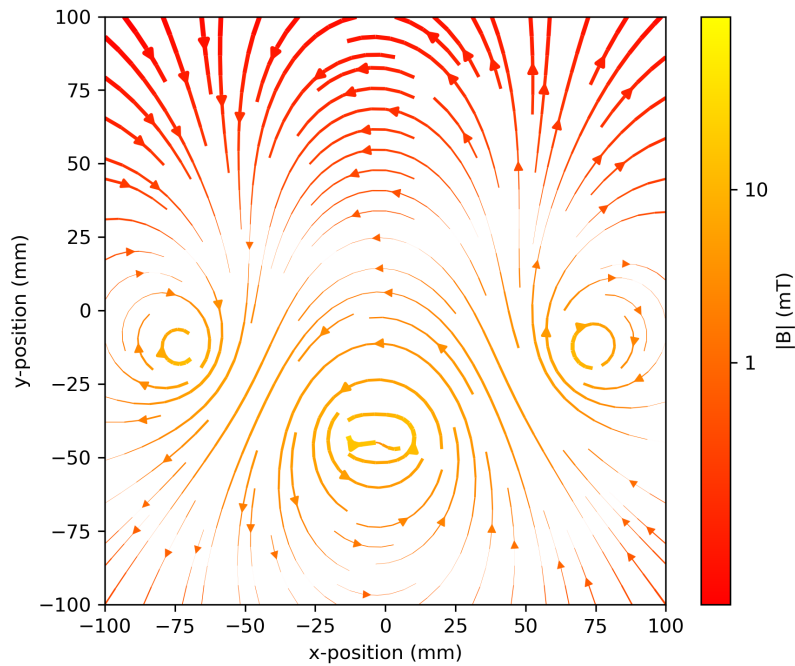
(b) Field magnitude in plane $z=0$.(c) Field lines in plane $z=0$.

Figure 4.5: Visualization of the magnetic field around the quadrature coil – Static field calculations for the quadrature coil using the python library Magpylib [75]. The position of the quadrature coil is shown in a), the magnitude of magnetic flux density in plane $z=0$ is shown in b), and the field lines of the same plane are shown in Figure c).

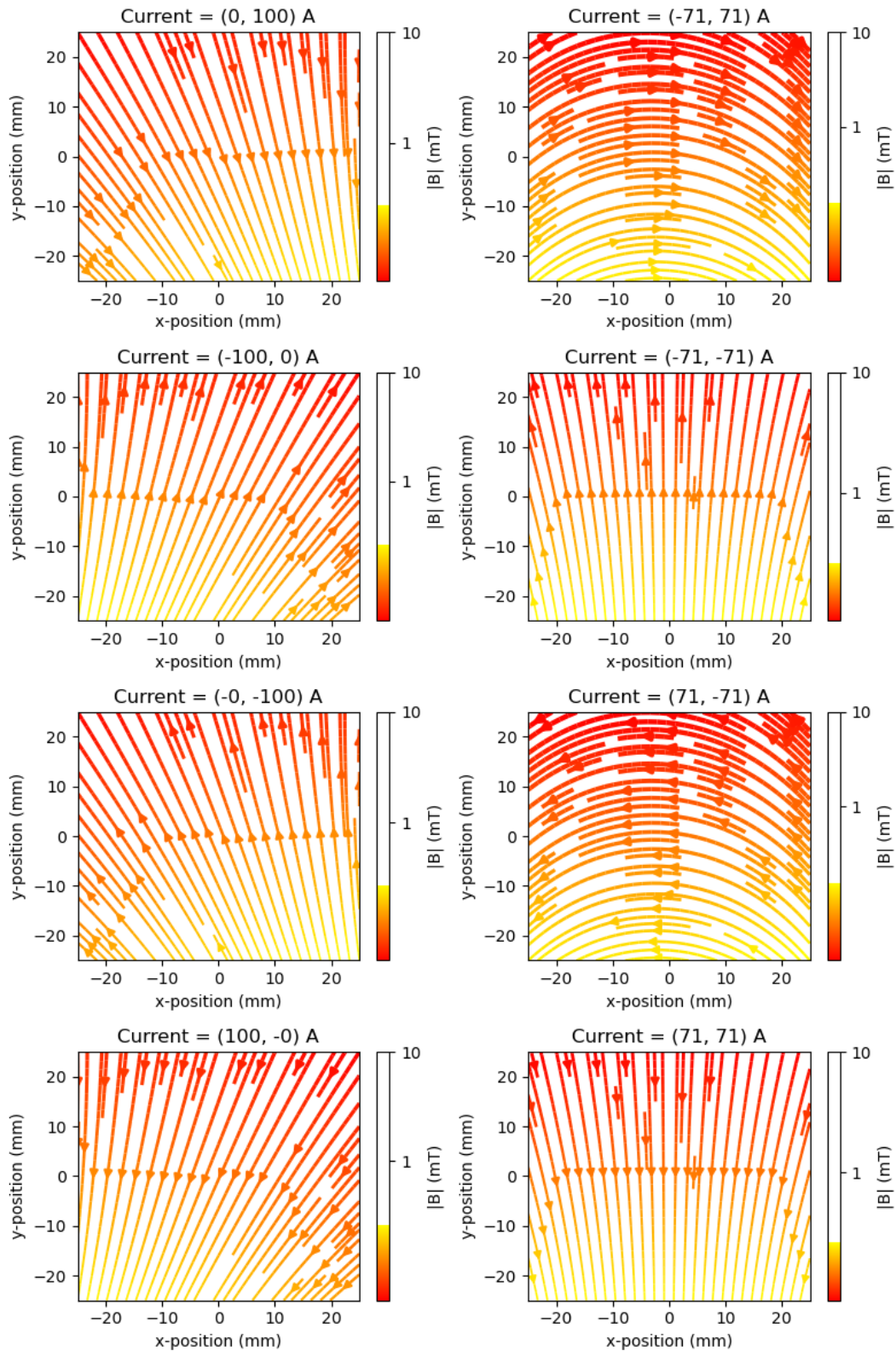


Figure 4.6: *The circularly polarized field of the quadrature coil – Static field calculations for a small volume above the quadrature coil at eight different time points during a period of AC current with a maximum current of 100A. Read from left to right, top to bottom.*

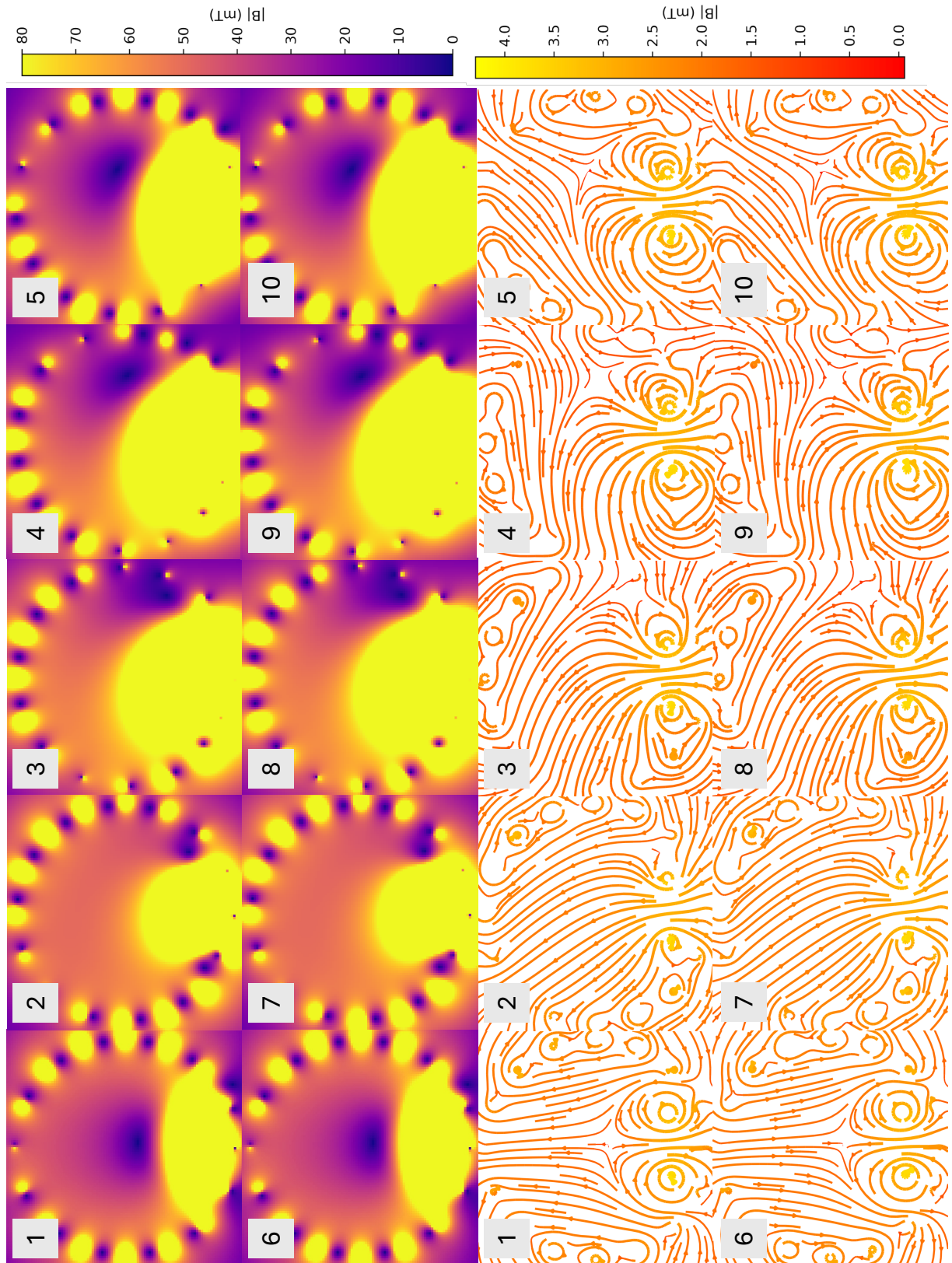


Figure 4.7: *The circularly polarized field of the birdcage and enhancing coil – Static field calculation for the birdcage coil with the enhancing coil inside at ten different time points during a period of AC current with a maximum current of 400A.*

4.2 Laboratory evaluation

Measurements for each coil, both unloaded and loaded with the chosen phantom, are presented graphically in separate figures. Error bars were omitted from the S-parameter plots because they were negligible after averaging.

4.2.1 Design 1: Single-loop coil

A square loop with side lengths 9cm was made out of tinned copper wire [112] with a diameter of 1.5mm and shaped to fit the curve underneath the stand-alone coil holder. The initially calculated capacitance and the capacitance of the finally chosen components are presented in table 4.1 with their names according to the circuit diagram in Figure 3.2. Several capacitors had to be mounted in parallel, adding their capacitance values like in equation 2.49. Figure 4.8 shows the final design.

Fixed capacitors are of Kyocera's series 100C [113] with a working voltage of 2500 VDC. The variable matching capacitor is a non-magnetic trimmer capacitor from Johanson with the part number 55H01, a working voltage of 1000 VDC, and a capacitance range of $[1 - 19]\text{pF}$. The variable tuning capacitor is also from Johnson with the part number 5610, a working voltage of 5000 VDC, and capacitance range $[1 - 7.5]\text{pF}$.

Figure 4.9 shows the S-parameter measurements of the single-loop coil. Under loading conditions, the resonance frequency is $(33.792 \pm 0.004)\text{MHz}$ with a $S_{11} = (-35 \pm 2)\text{dB}$ and an impedance of $(49.19 - i0.30)\Omega$ presented at the ports of the coil. The resonance frequency differs by 0.01MHz from the desired 33.78MHz , but the minimum S_{11} and the impedance at resonance indicate a well-matched coil. The plotted graph in Figure 4.9 shows that the reflection is low at 33.78MHz as well.

Table 4.1: *Components used for the single-loop coil* – Capacitor values calculated and used in practice for the single-loop coil. Further component details can be found in data specification sheets: Kyocera's fixed capacitors from 100C series [113], Johanson's variable trimmer capacitors series 55H and 5610 [114], and the tinned copper wire of 1.5mm diameter [112].

	Calculated	Applied	Tolerance
C_1	150pF	120pF	$\pm 1\%$
C_2	150pF	144pF	$\pm 1\%$
$C_3 \approx 2C_m$	24pF	27pF	$\pm 1\%$
$C_4 \approx 2C_m$	24pF	30pF	$\pm 1\%$
C_{m0}	-	$(1 - 19)\text{pF}$	-
C_T	-	$(1 - 7.5)\text{pF}$	-

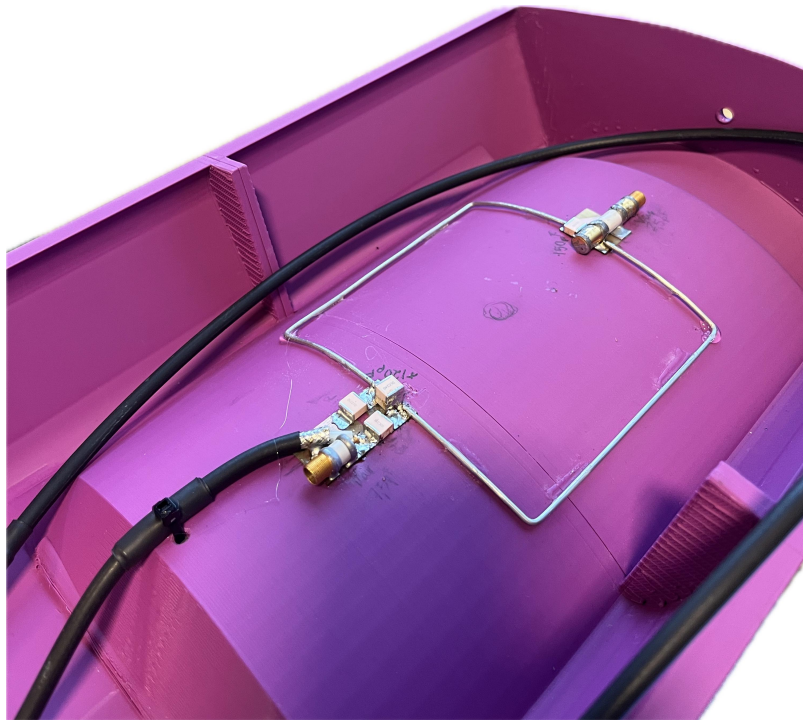


Figure 4.8: Image of the single-loop coil – The final single-loop coil mounted on the 3D printed stand-alone coil holder.

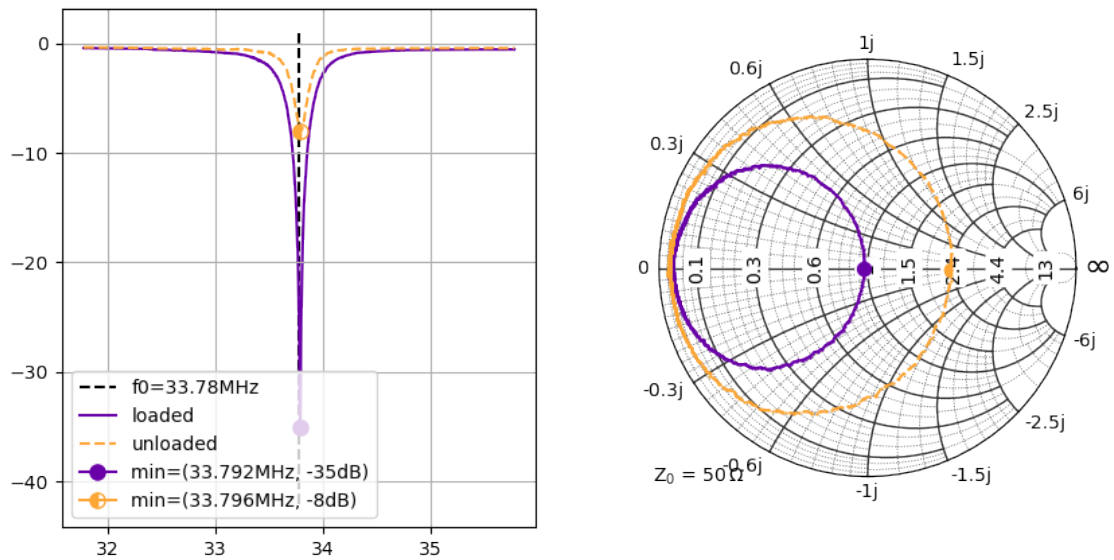


Figure 4.9: Plots of the single-loop coil's laboratory measurements – S_{11} magnitude plot and Smith chart presenting the single-loop coil's laboratory measurements. Two plotted curves for different coil loading, one with no load and the other with the selected phantom.

4.2.2 Design 2: Enhancing coil

Another square loop with side lengths 9cm was made and shaped to fit the curve underneath the enhancing coil holder before capacitors, an inductor, and diodes were connected according to the electronic schematic in Figure 3.3. The homemade inductor was made using a drill bit of 5.5mm diameter, turning the tinned copper wire around it eight times. The wire used was the same as was used for the coil square [112]. The capacitance and inductance of the initially connected components and the finally used components are presented in table 4.2 with their names according to the circuit drawing in Figure 3.3. Figure 4.10 shows the final coil mounted on the holder.

The laboratory measurements presented in Figure 4.12 were performed using the homemade magnetic field probe shown in Figure 4.11. The pick-up probe was kept in the same place for all measurements, aided by masking tape. The S_{11} magnitude plot in Figure 4.12 shows that the enhancing coil has a resonance frequency of 33.72MHz when loaded, which differs from the desired resonance frequency (33.78MHz) by 0.06MHz . However, the S_{11} magnitude is not much higher at 33.78MHz . The resonance frequency shifts slightly from loaded to unloaded conditions. The Smith plots of Figure 4.12 show that the matching with the homemade single-loop probe is far from ideal.

Table 4.2: *Components used for the enhancing coil* – Capacitor and inductor values calculated and used in practice for the enhancing coil. Further component details can be found in data specification sheets: Kyocera’s fixed capacitors from 100C series [113], and the tinned copper wire of 1.5mm diameter [112].

	Calculated	Applied	Tolerance
C_{E1}	150pF	147pF	$\pm 1\%$
C_{E2}	150pF	150pF	$\pm 1\%$
L_{E1}	157nH	$-n\text{H}$	$\pm 1\%$



Figure 4.10: *Image of the enhancing coil* – The final enhancing coil mounted on the 3D printed enhancing holder.



Figure 4.11: *Homemade single-loop probe* – Magnetic field probe made to the specifications of Douglas C. Smith [108], to measure the resonance frequency of the enhancing coil. Components used to make this were a BNC to SMA connector, heat shrink tubes of various sizes, solder, copper snail tape, and tinned copper wire.

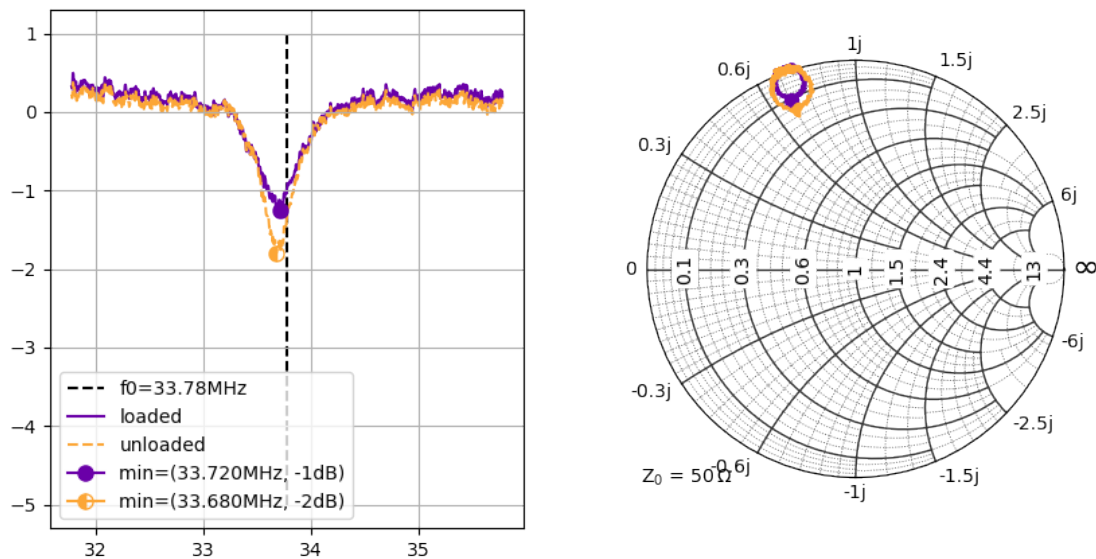


Figure 4.12: Plots of the enhancing coil's laboratory measurements – S_{11} magnitude plot and Smith chart presenting the enhancing coil's laboratory measurements. Two plotted curves for different coil loading, one with no load and one with the selected phantom.

4.2.3 Design 3: Quadrature coil

Two loops of side length 8.5cm were mounted on a second stand-alone coil holder. The side length was the maximum possible underneath the coil holder, assuming a 15% area overlap for decoupling. The component values of the initial prototype and the component values in the finished coil are presented in table 4.3. Figure 4.13 shows the final design.

The S -parameter magnitude plots for the loaded and unloaded coil are shown in figures 4.15 and 4.14, respectively. The resonating frequencies of the loops under loading conditions were $(33.788 \pm 0.004)\text{MHz}$ and $(33.784 \pm 0.004)\text{MHz}$. Their final resonance peaks differ in value with $(-40 \pm 6)\text{dB}$ and $(-27 \pm 3)\text{dB}$, but both values are very low. The decoupling measured by the through parameter between the loaded loops was approximately -17dB at the resonance frequency. The Smith chart in Figure 4.16 shows the difference in matching between the two coils at both loaded and unloaded conditions. The two impedances at resonance under loading are slightly different with $(49.3 \pm i1.6)\Omega$ and $(48.5 \pm i3.2)\Omega$, respectively. The latter inductance is furthest away from a pure 50Ω resistive load, and this loop is the one with the highest S_{11} magnitude at resonance.

Table 4.3: *Components used for the quadrature coil* – Capacitor values initially calculated and the values finally chosen for the quadrature coil. Further component details can be found in data specification sheets: Kyocera’s fixed capacitors from 100C series [113], Johanson’s variable trimmer capacitors series 55H and 5610 [114], and the tinned copper wire of 1.5mm diameter [112].

	Calc.	Applied	Tol		Calc.	Applied	Tol
C_{1Q}	$150pF$	$150pF$	$\pm 1\%$	C_{1P}	$150pF$	$150pF$	$\pm 1\%$
C_{2Q}	$150pF$	$183pF$	$\pm 1\%$	C_{2P}	$150pF$	$197pF$	$\pm 1\%$
$C_{3Q} \approx 2C_m$	$24pF$	$33pF$	$\pm 1\%$	$C_{3P} \approx 2C_m$	$24pF$	$33pF$	$\pm 1\%$
$C_{4Q} \approx 2C_m$	$24pF$	$33pF$	$\pm 1\%$	$C_{4P} \approx 2C_m$	$24pF$	$33pF$	$\pm 1\%$
C_{mq0}	-	$(1 - 19)pF$	-	C_{mp0}	-	$(1 - 19)pF$	-
C_{TQ}	-	$(1 - 7.5)pF$	-	C_{TP}	-	$(1 - 7.5)pF$	-



Figure 4.13: *Image of the quadrature coil* – The final electrical design of the quadrature coil mounted on the 3D printed stand-alone coil holder.

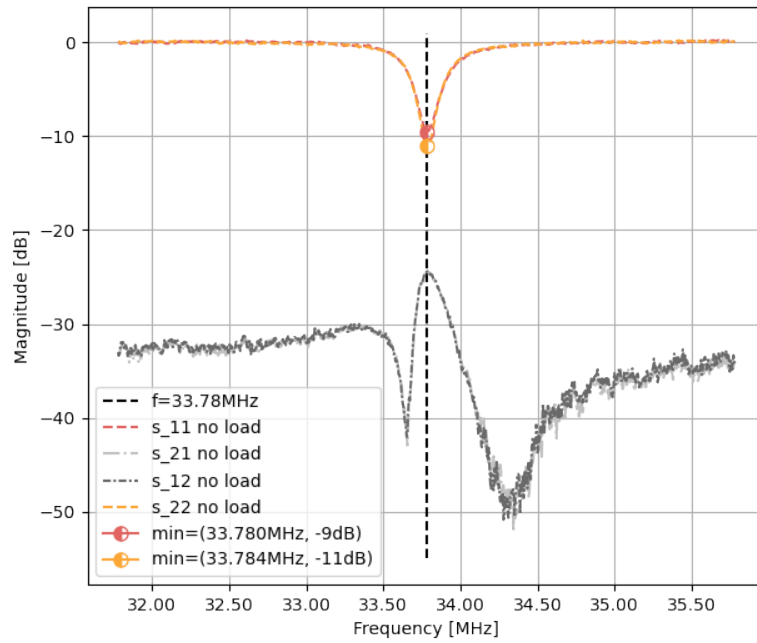


Figure 4.14: *Plot of the quadrature coil's unloaded S-parameter measurements* – Magnitude of S-parameters for the quadrature coil. The coil was not loaded.

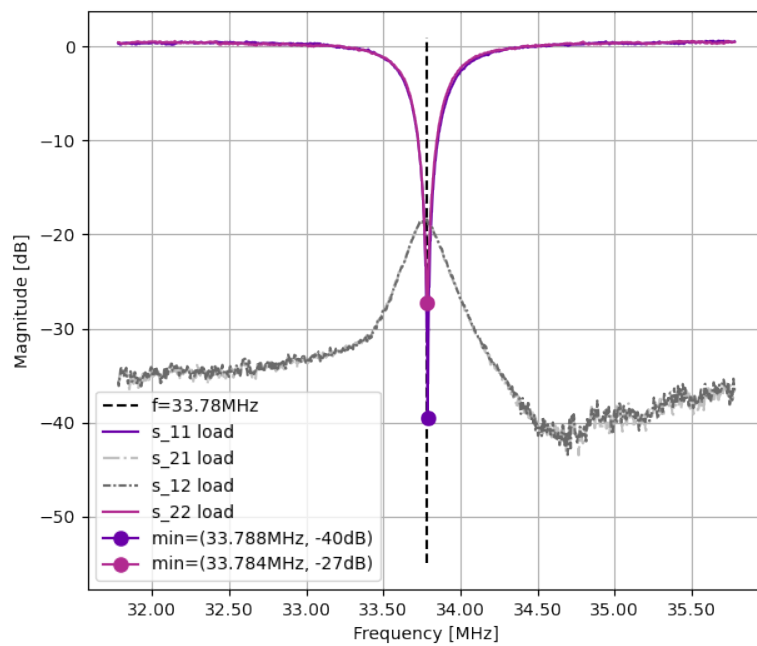


Figure 4.15: *Plot of the quadrature coil's loaded S-parameter measurements* – Magnitude of S-parameters for the quadrature coil. The coil was loaded with the selected phantom.

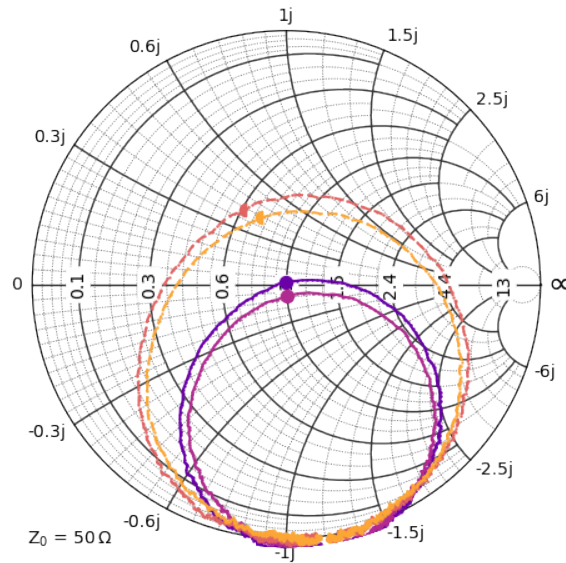


Figure 4.16: *Smith plot of the quadrature coil's S-parameter measurements* – Smith plots for the S_{11} and S_{22} parameters when the coil was loaded (the two small circles) and when the coil was not loaded (the two large circles).

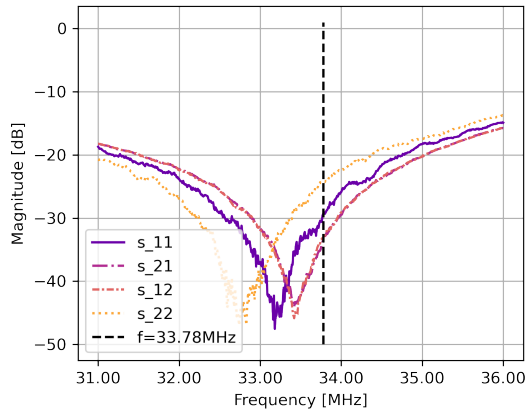
The Hybrid

The Hybrid was attached to the two loops through two coaxial cables; see Figure 4.13. The two remaining Hybrid ports were connected to coaxial cables ready for connection with the T/R switch of the MRI machine. These coaxial cables were labeled with blue and green tape, and MRI imaging established that the blue cable is the transmit (Tx) cable and the green is the reception (Rx) cable.

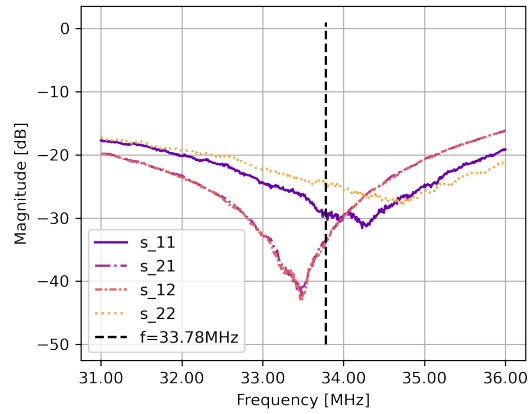
Magnitude plots of four S-parameters for all six possible connections of the Hybrid as a 4-port device to the VNA are presented in Figure 4.17. The measured S-parameters' specific magnitude and phase values at 33.78MHz are shown in Table 4.4. During each measurement, the unconnected ends of the Device Under Test (DUT) were terminated by 50Ω termination resistors. The measured S_{12} and S_{21} parameters between the two ports alongside each other were measured to -33.0dB on the coax side and -33.5dB on the SMA side. These numbers indicate isolation between the ports. Measurements of the S_{12} and S_{21} parameters between the Hybrid's four opposing connectors were around -3.5dB , indicating that the signal will be let through the device with low loss. The plots in Figure 4.17 (c-f) show that a compromise between the reflection parameters S_{11} and S_{22} was found.

The phase difference between the output ports using the Rx cable (green) as input were $(1.486 \pm 0.004)\text{rad} \approx (85.1 \pm 0.2)^\circ$ for the S_{21} parameter and $(1.476 \pm 0.004)\text{rad} \approx (84.6 \pm 0.2)^\circ$ rad for the S_{12} parameter. The phase difference between the output ports using the Tx cable (blue) as input were $(1.486 \pm 0.006)\text{rad} \approx (85.1 \pm 0.3)^\circ$

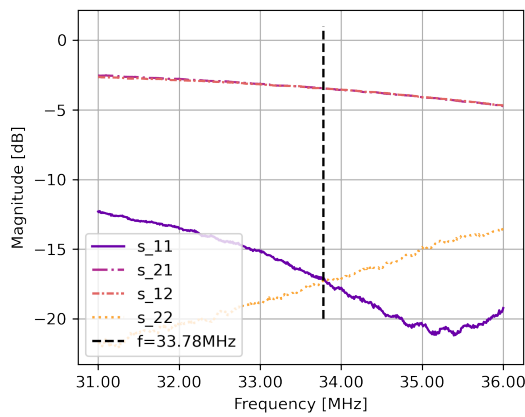
for the S_{21} parameter and $(1.480 \pm 0.006) \text{ rad} \approx (84.8 \pm 0.3)^\circ$ for the S_{12} parameter. The bold numbers in Table 4.4 are associated with the phase differences.



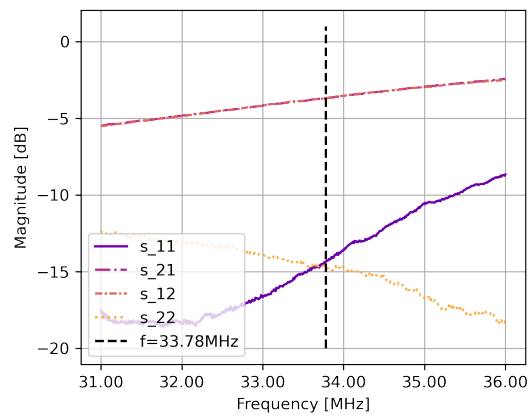
(a) Isolation between SMA connectors



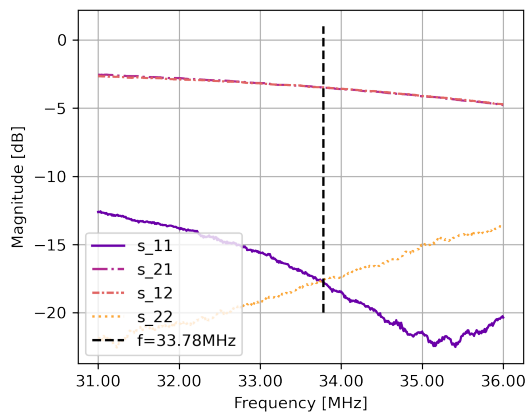
(b) Isolation between green and blue



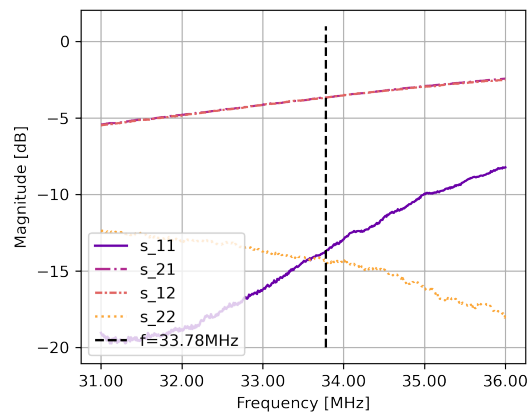
(c) From green through to same side SMA



(d) From green through to opposite side SMA



(e) From blue through to same side SMA



(f) From blue through to opposite side SMA

Figure 4.17: *S*-parameter magnitude plots from the Hybrid – *S*-parameter measurements for the six connections to the Hybrid. Each setup is described underneath the specific plot regarding the colors of the cable labels and the connectors at the end of the cables; see Figure 4.13. Table 4.4 presents exact values at the resonance frequency.

Table 4.4: *S*-parameter measurements of the Hybrid – Scattering parameter measurements of the Hybrid at the resonance frequency of the system (33.78MHz).

		S_{11}	S_{21}	S_{12}	S_{22}
Hybrid, coil coax	Magn [dB]	-29 ± 1	-33.4 ± 0.7	-33.0 ± 0.8	-24 ± 1
	Phase [rad]	-1 ± 1	-1.2 ± 0.9	-1 ± 1	-1.45 ± 0.03
Hybrid, MRI coax	Magn [dB]	-29 ± 1	-33.8 ± 0.7	-33.8 ± 0.7	-24.8 ± 0.7
	Phase [rad]	0 ± 1	-0.6 ± 0.7	-0.45 ± 0.08	0 ± 1
Hybrid through, green to same	Magn [dB]	-17.2 ± 0.2	-3.46 ± 0.02	-3.45 ± 0.01	-17.3 ± 0.3
	Phase [rad]	-0.47 ± 0.04	0.103 ± 0.004	0.098 ± 0.003	-0.30 ± 0.04
Hybrid through, green to opposite	Magn [dB]	-14.4 ± 0.1	-3.68 ± 0.03	-3.68 ± 0.04	-14.7 ± 0.3
	Phase [rad]	-0.76 ± 0.03	-1.383 ± 0.002	-1.378 ± 0.003	-0.90 ± 0.03
Phase difference [rad], input to green		-	1.486 ± 0.004 $= (85.1 \pm 0.2)^\circ$	1.476 ± 0.004 $= (84.6 \pm 0.2)^\circ$	-
Hybrid through, blue to same	Magn [dB]	-17.7 ± 0.2	-3.50 ± 0.02	-3.48 ± 0.02	-17.5 ± 0.1
	Phase [rad]	-0.51 ± 0.04	0.116 ± 0.006	0.112 ± 0.006	-0.32 ± 0.05
Hybrid through, blue to opposite	Magn [dB]	-13.70 ± 0.05	-3.66 ± 0.02	-3.67 ± 0.03	-14.3 ± 0.1
	Phase [rad]	-0.86 ± 0.02	-1.370 ± 0.002	-1.368 ± 0.002	-0.92 ± 0.02
Phase difference [rad], input to blue		-	1.486 ± 0.006 $= (85.1 \pm 0.3)^\circ$	1.480 ± 0.006 $= (84.8 \pm 0.3)^\circ$	-

4.2.4 Prior designs

Laboratory measurements of Prior Design One are shown in Figure 4.18, and measurements of Prior Design Two are shown in Figure 4.19. The Smith charts in these figures indicate that these coils' impedances differ significantly from a pure 50Ω resistive load under loading conditions. The S_{11} magnitude at resonance under loading conditions is $-18dB$ for Prior Design One and $-9dB$ for Prior Design Two, which indicates that these two coils are of different quality, even though they appear similar; see images in Figure 3.5 and Figure 3.6.

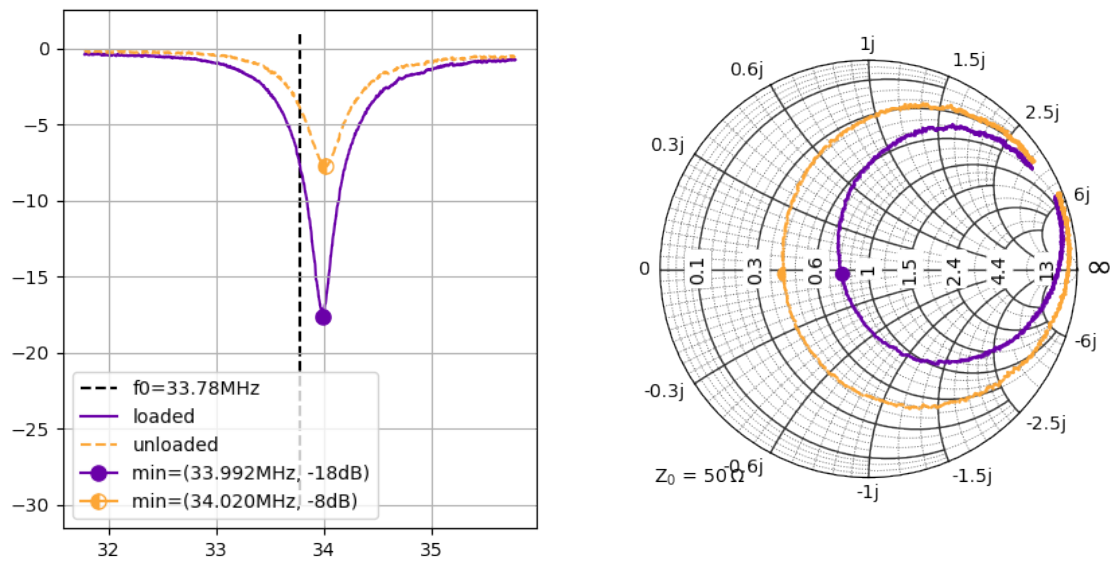


Figure 4.18: Plots of the Prior Design One's laboratory measurements – S_{11} magnitude plot and Smith chart for the Prior Design One. Two plotted curves for different coil loading, one with no load and the other with the selected phantom.

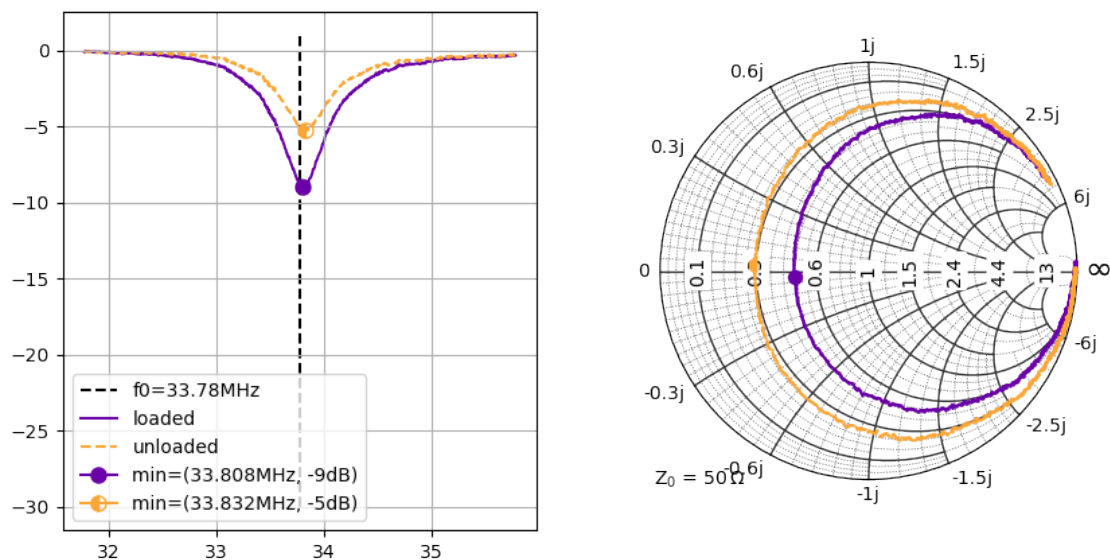


Figure 4.19: Plots of the Prior Design Two's laboratory measurements – S_{11} magnitude plot and Smith chart for Prior Design Two. Two plotted curves for different coil loading, one with no load and the other with the selected phantom.

4.2.5 Summary of laboratory evaluations

A summary of the laboratory measurements performed under loading conditions is provided in Table 4.5, where the resonance frequency, the S_{11} value at resonance, calculated Q-ratio, and the coil impedance at resonance are presented numerically for all coils. The presented numbers are averages and standard deviations of the ten measurement series. The Q-ratio for the quadrature coil was calculated from the average loaded and unloaded Q-value of the two loop elements.

All coils have resonance frequencies close to 33.78MHz , except the enhancing coil, which deviates by 60kHz . The resonance frequency of Prior Design Two is closer to 33.78MHz than that of the single-loop coil. The complex impedance indicates that the prior designs are poorly matched compared to the quadrature and single-loop coils. The single-loop and quadrature coils are well matched to a 50Ω resistive load, reflected by the low S_{11} parameter. The two loops of the quadrature coil seem to have very different minimum S_{11} . However, this difference is minimal considering the decibel measurement and the two coil elements of the quadrature coil present with similar metrics overall. The Q-ratios of the single-loop and quadrature coils are superior to those of the prior designs.

Table 4.5: *Laboratory evaluation of all coils* – Overview of laboratory evaluation parameters for the three developed and the two prior designs under loading conditions. The Q-factor is a dimensionless unit.

Design	Resonance frequency	Q-ratio (2.64)	Minimum S_{11}	Complex impedance
Single-loop coil	$(33.792 \pm 0.004)\text{MHz}$	$\frac{-289.01}{-82.67} = 3.50$	$(-35 \pm 2)\text{dB}$	$(49.19 - i0.30)\Omega$
Enhancing coil	$(33.720 \pm 0.004)\text{MHz}$	–	–	–
Quadrature coil	$(33.788 \pm 0.004)\text{MHz}$ $(33.784 \pm 0.004)\text{MHz}$	$\frac{93.32}{20.66} = 4.52$	$(-40 \pm 7)\text{dB}$ $(-27 \pm 2)\text{dB}$	$(49.93 + i0.50)\Omega$ $(50.12 - i2.22)\Omega$
Prior design One	$(33.992 \pm 0.004)\text{MHz}$	$\frac{49.90}{39.71} = 1.26$	$(-17.6 \pm 0.2)\text{dB}$	$(43.49 - i1.01)\Omega$
Prior design Two	$(33.808 \pm 0.004)\text{MHz}$	$\frac{38.57}{33.36} = 1.16$	$(-8.94 \pm 0.08)\text{dB}$	$(32.19 - i1.36)\Omega$

4.3 MRI performance

All MRI images in this section show a central traversal slice of an imaging volume containing the selected phantom shown in figure 3.7. The selected phantom was placed with its bottleneck pointing the same way the neck of a human would if a human head were resting on the coil holder, see Figure 4.2. The boxes indicated in the MRI images indicate which pixels were used to calculate the SNR values for each coil. Table 3.1 shows an overview of the parameters of the three different radial CN UTE sequences, CN-197, CN-1442, and CN-2552.

4.3.1 Design 1: Single-loop coil

Images from the three acquired scans are shown in figure 4.20 and show an even highlight of the phantom volume close to the single-loop coil. The visible part of the phantom resembles a crescent moon. The phantom seems smaller and has a more blurred edge in scan CN-197 than in scans CN-1442 and CN-2552.

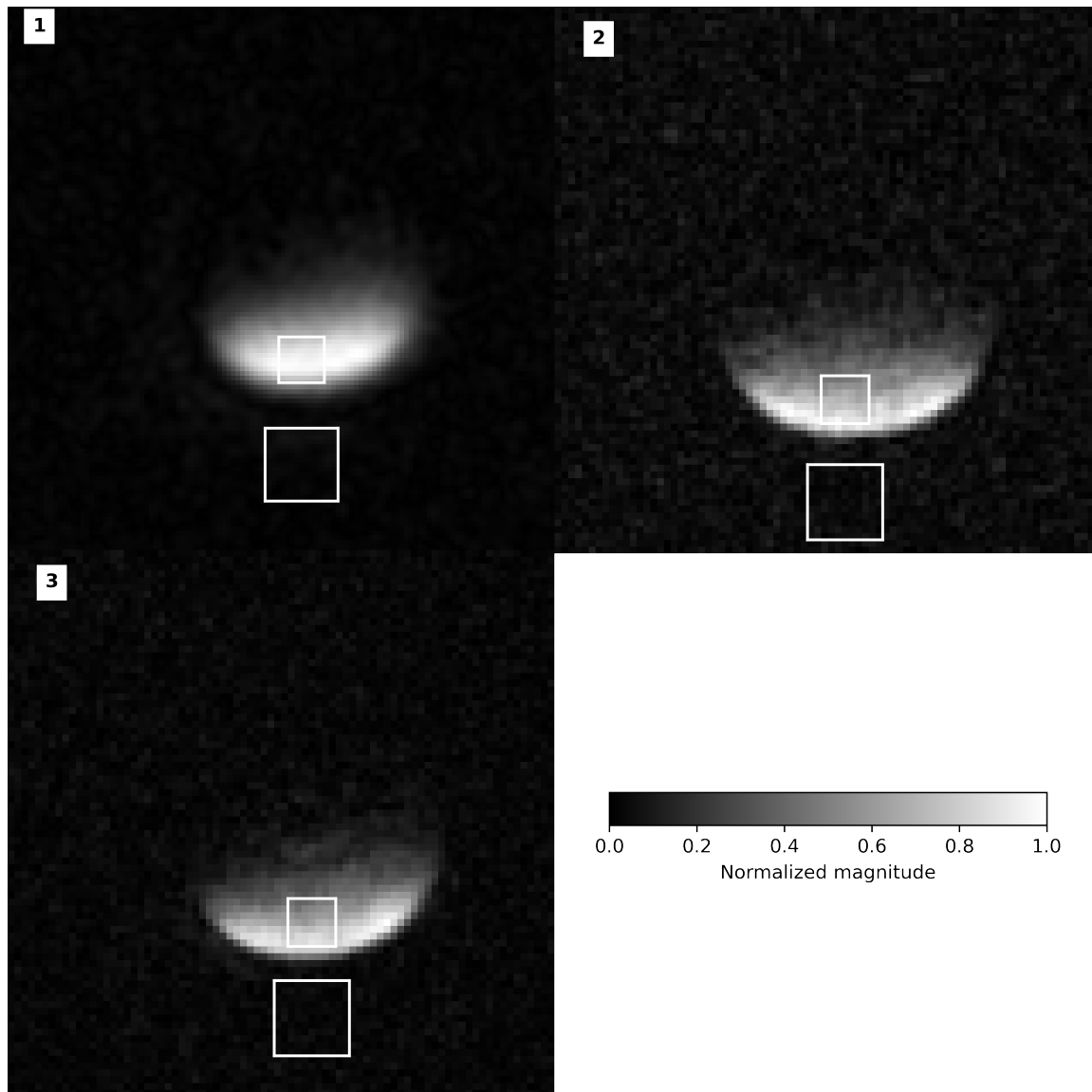


Figure 4.20: *Single-loop MRI, phantom images* – ^{23}Na -MRI scans acquired with the CN-197 (1), CN-1442 (2), and CN-2552 (3) UTE sequences, described in table 3.1, using the single-loop coil.

4.3.2 Design 2: Enhancing coil

The three MRI scans of the selected phantom acquired with the birdcage coil are shown in Figure 4.21. All three scans show an even signal intensity distribution over a circular area, but the area differs slightly in size from the CN-197 scan to the others. The CN-197 scan shows a circle with a very blurry edge, while scans CN-1442 and CN-2552

have sharper edges. Scan CN-1442 exhibits slightly more noise in the background and phantom areas than scan CN-2552.

The three scans acquired with the enhancing coil inside the birdcage coil are shown in Figure 4.22. The signal is no longer evenly distributed over the circular phantom. In these scans, the lower right part of the circle has an enhanced signal intensity relative to the rest of the circular phantom area. The lower left part of the circle exhibits a small area of weakened signal intensity. The enhancement seems skewed to one side of the enhancing coil.

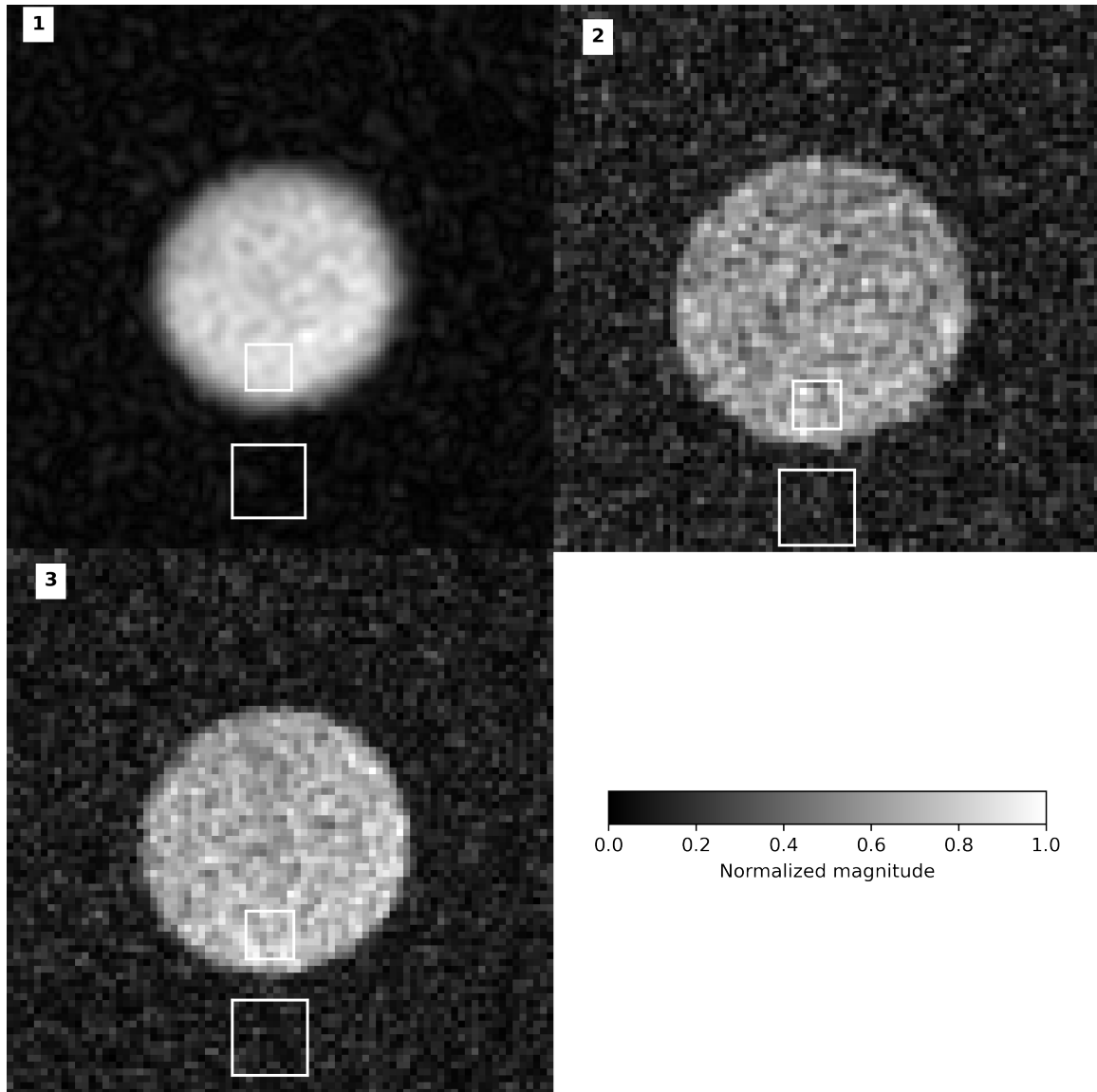


Figure 4.21: *Birdcage MRI, phantom images* – ^{23}Na -MRI scans acquired with the CN-197 (1), CN-1442 (2), and CN-2552 (3) UTE sequences, described in table 3.1, using the birdcage coil.

4.3.3 Design 3: Quadrature coil

The quadrature coil's two cables were connected to the Tx and Rx connectors of the T/R switch. Only when the Tx cable was attached to transmit and the Rx cable to

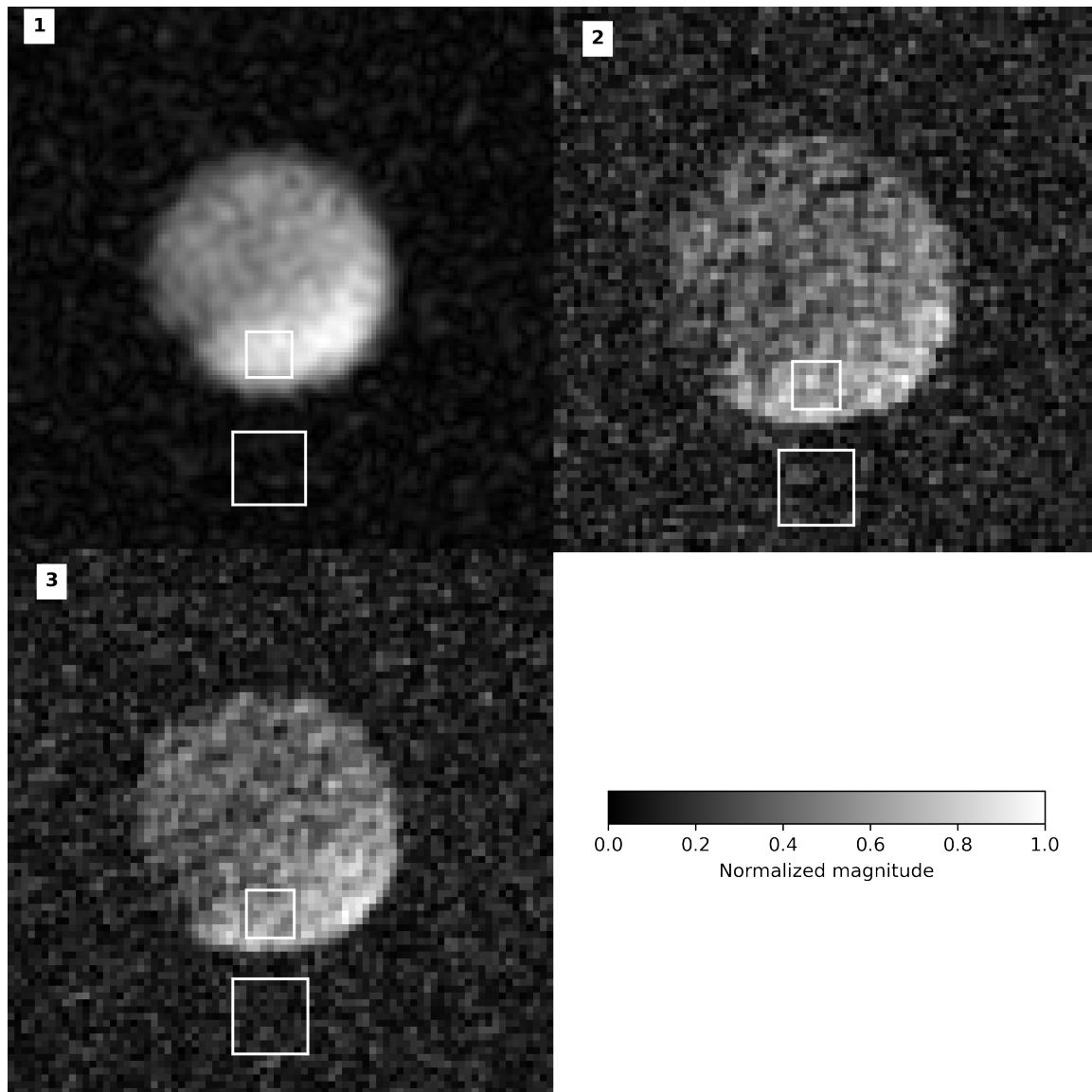


Figure 4.22: *Enhancing coil MRI, phantom images* – ^{23}Na -MRI scans acquired with the CN-197 (1), CN-1442 (2), and CN-2552 (3) UTE sequences, described in table 3.1, using the enhancing coil inside the birdcage coil.

receive MRI scans such as those presented in Figure 4.23 were produced. The opposite connection of the cables to the T/R switch did not produce an image of the phantom. The three acquired images seem similar to those acquired with the single-loop coil, but the highlighted area is more centered at the bottom edge of the phantom. The crescent moon shape is apparent from all scans, but the CN-197 scan is more blurry. Scans CN-1442 and CN-2552 show a more highlighted edge before the signal decreases further into the phantom.

4.3.4 Prior designs

In Figure 4.24, Prior Design One shows the lower third of a circle with an evenly distributed signal intensity, falling off with distance from the coil. The highlighted area

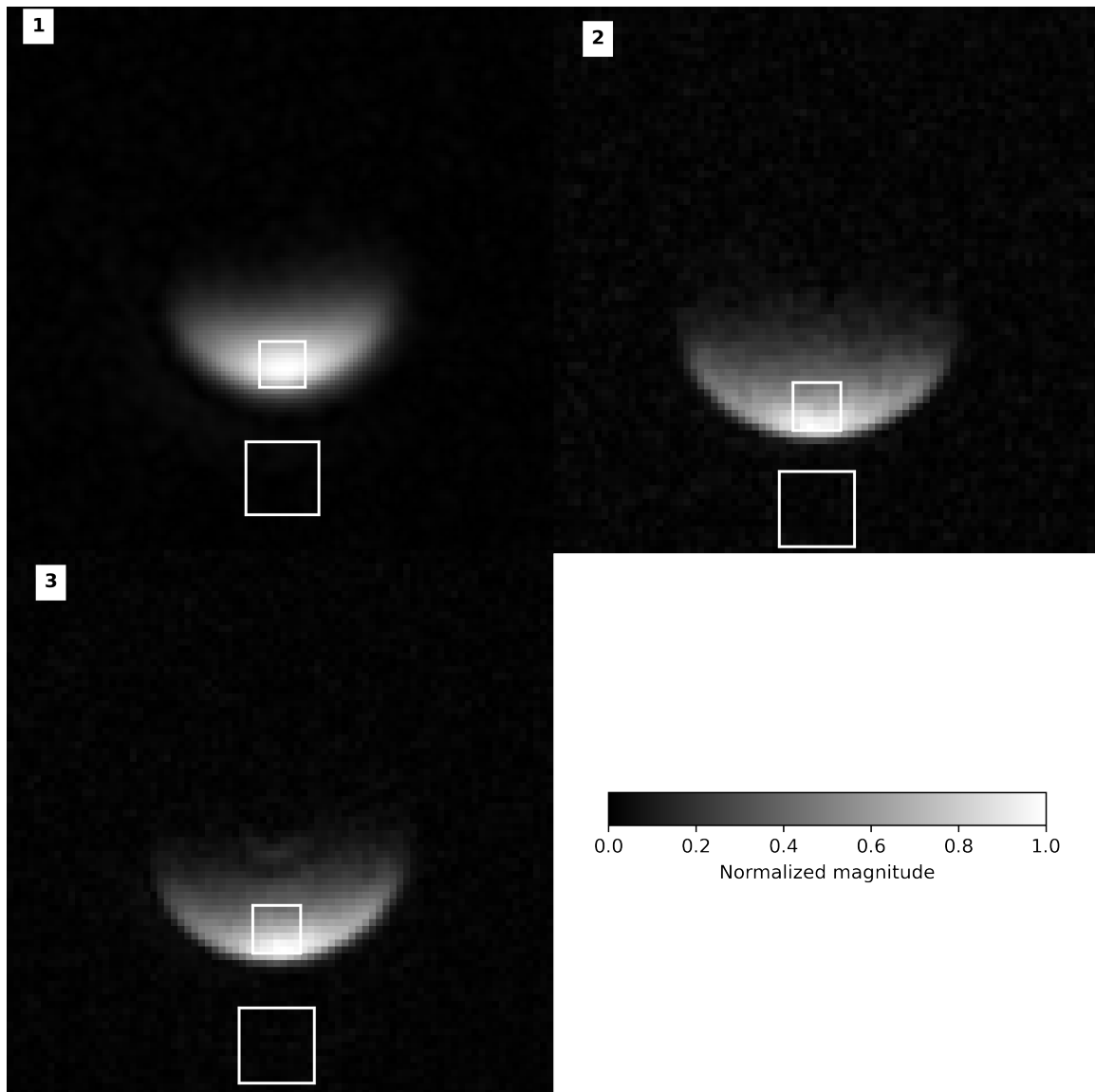


Figure 4.23: *Quadrature coil MRI, phantom images* – ^{23}Na -MRI scans acquired with the CN-197 (1), CN-1442 (2), and CN-2552 (3) UTE sequences, described in table 3.1, using the quadrature coil

does not follow the phantom edge as it did for the single-loop coil. A circular shape can be recognized from scans CN-1442 and CN-2552, but from scan CN-197, it is more challenging.

From the scans acquired with Prior Design Two presented in Figure 4.25, it is challenging to recognize the circular shape of the phantom from any of the scans. The shape is disturbed, and the signal falls off with distance from the coil, but the fall-off is less smooth than in the scans acquired with Prior Design One.

4.3.5 Correction for B1 field inhomogeneities

The B_1 -field inhomogeneity correction method using a blurred version of the image was applied to the images acquired with the CN-197 parameters for all coils. Both the prior designs display a relatively noisy area after this correction; see the result for Prior

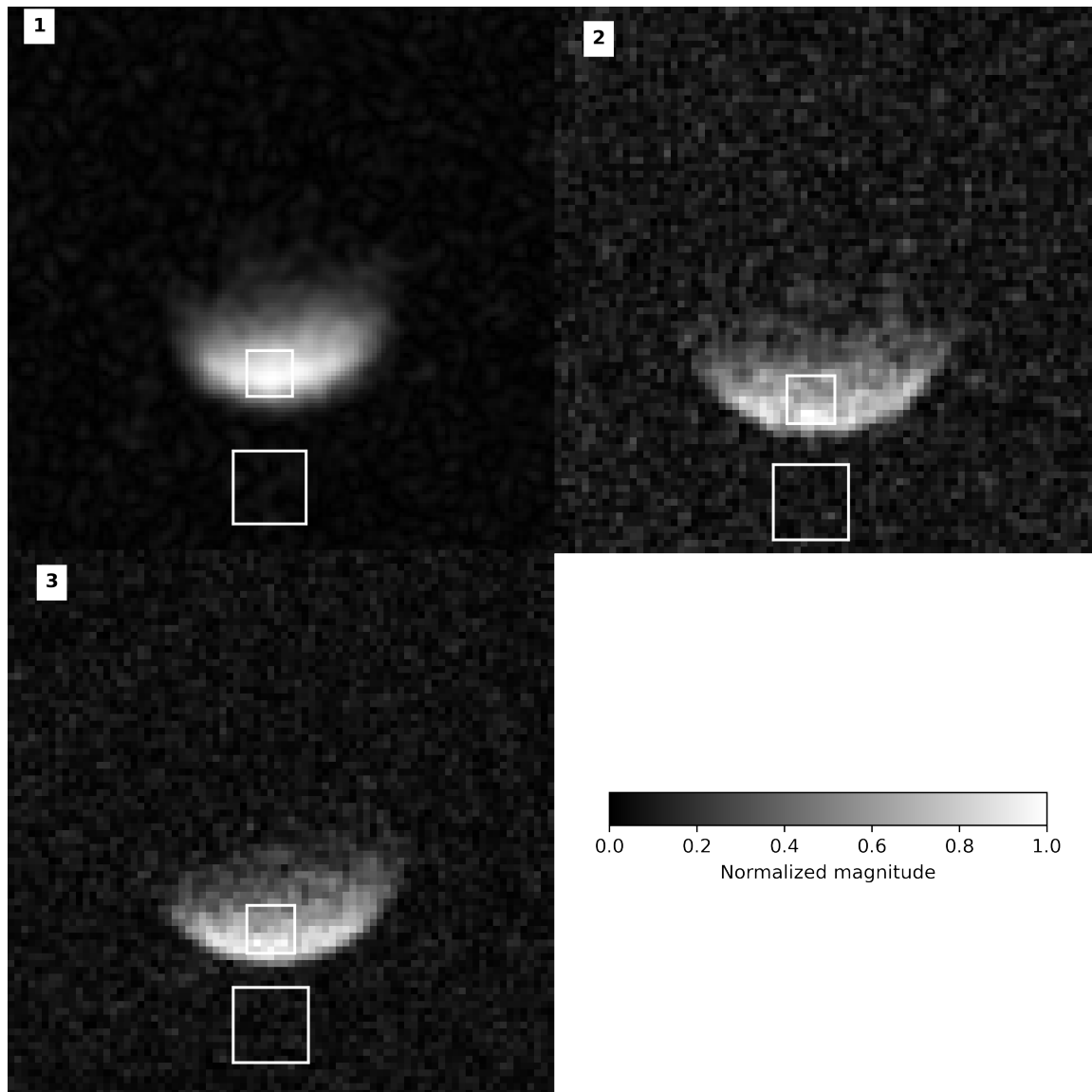


Figure 4.24: *Prior Design One MRI, phantom images* – ^{23}Na -MRI scans acquired with the CN-197 (1), CN-1442 (2), and CN-2552 (3) UTE sequences, described in table 3.1, using the Prior Design One for imaging the selected phantom.

Design One in Figure 4.26 and the result for Prior Design Two in Figure 4.27. The single-loop coil and the quadrature coil, on the other hand, show a more even signal distribution after this correction; see Figure 4.28 for the single-loop results and Figure 4.29 for the quadrature results. The corrected quadrature image displays a half circle.

The blurred inhomogeneity field correction had little effect on the image acquired with the birdcage coil; see Figure 4.30. On the image acquired with the birdcage coil and the enhancing coil, on the other hand, the signal intensity distribution became more even after this correction, see Figure 4.31.

B_1 field inhomogeneity correction using DAM was applied to the images acquired with the CN-197 scan for the quadrature coil and the birdcage coil with the enhancing coil inside. The results are shown in figures 4.32 and 4.33, respectively. The corrected version of the quadrature coil image in Figure 4.32 (3) has a widened area of maximum

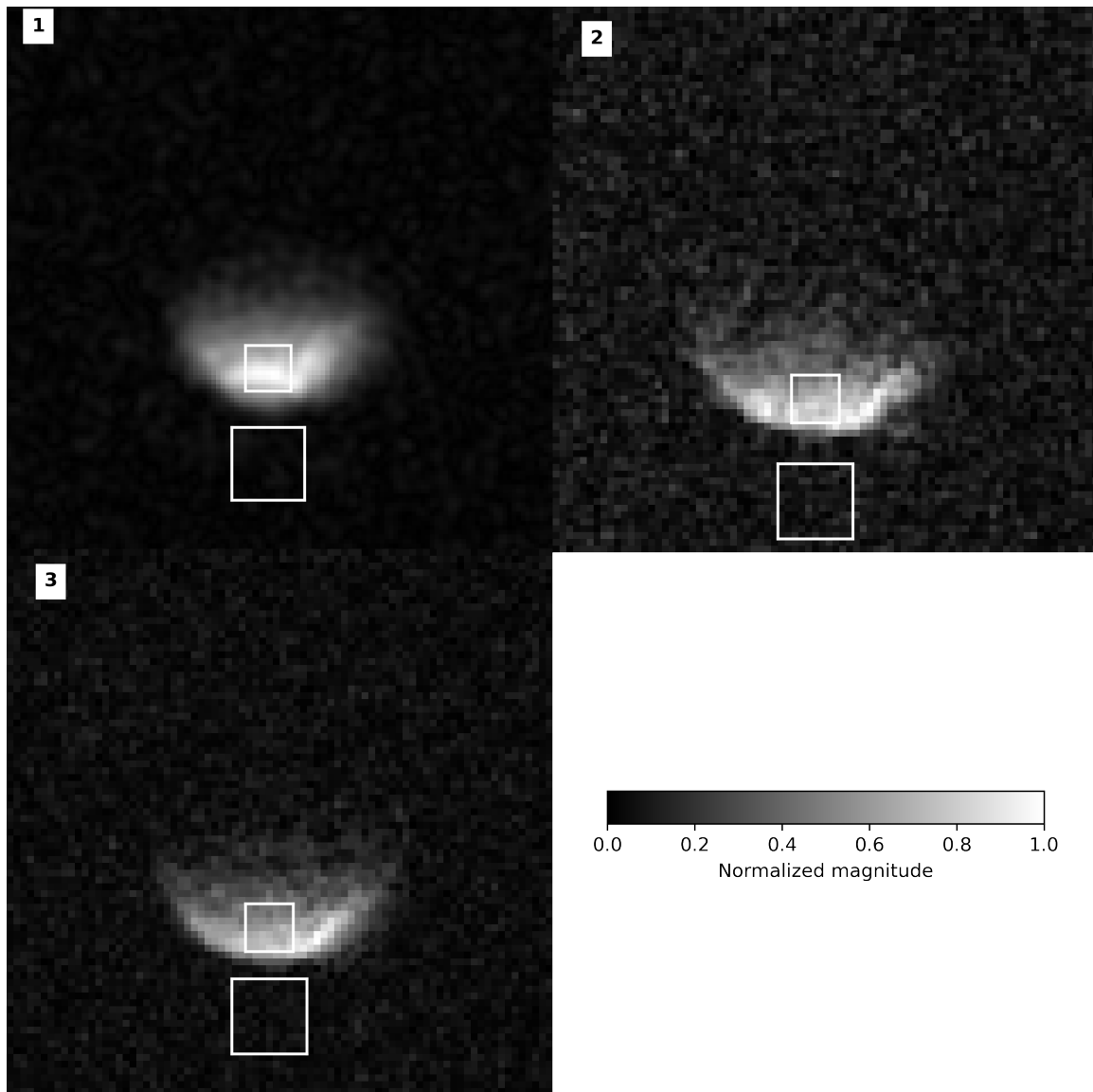


Figure 4.25: *Prior Design Two MRI, phantom images* – ^{23}Na -MRI scans acquired with the CN-197 (1), CN-1442 (2), and CN-2552 (3) UTE sequences, described in table 3.1, using Prior Design Two for imaging the selected phantom.

signal intensity compared to the original image in (2). The correction does not seem to have a good impact on the image acquired with the birdcage coil; see Figure 4.33 (3) compared to (2). The average normalized signal intensity of the corrected image seems to have dropped in magnitude. The field map from the enhancing coil in Figure 4.33 (1) is very noisy in the phantom area compared to the field map from the quadrature coil in Figure 4.32 (1).

4.3.6 Comparison across coil designs

The squares indicated in the MRI images were used to calculate SNR values for all coils and scans. A bar chart in Figure 4.34 shows the results. Following any of the three scans, arranging the coils in decreasing SNR would yield the same sequence of

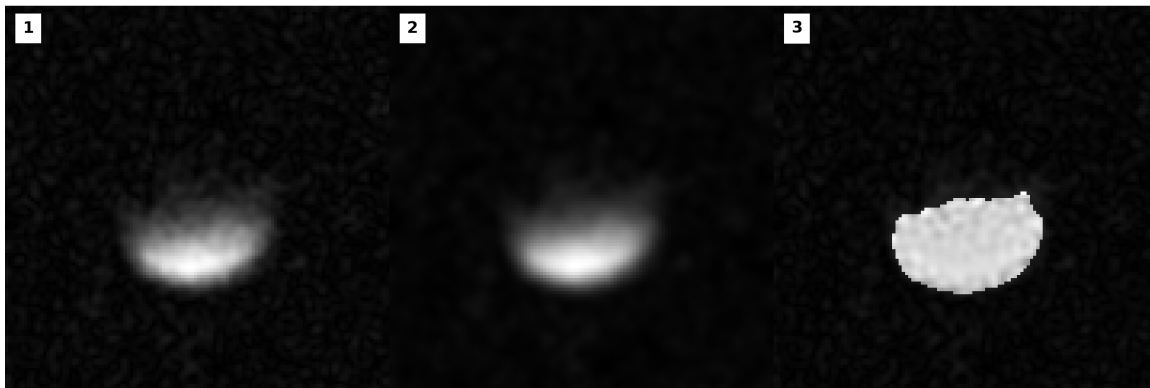


Figure 4.26: *Blurred B1 correction for Prior Design One* – 1) The original image acquired with the CN-197 scan (table 3.1) and the Prior Design One, 2) blurred version of the image using a normalized 3x3 box blur, 3) the corrected image using the blurred image with a threshold of 0.15.

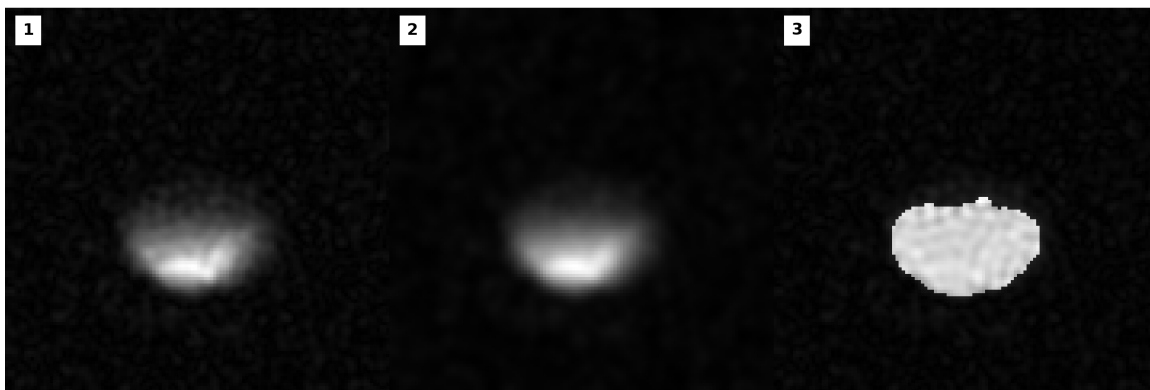


Figure 4.27: *Blurred B1 correction for Prior Design Two* – 1) The original image acquired with the CN-197 scan (table 3.1) and Prior Design Two, 2) blurred version of the image using a normalized 3x3 box blur, 3) the corrected image using the blurred image with a threshold of 0.15.

the coils. The quadrature coil has the superior SNR, while the single-loop coil's SNR is slightly higher than the prior designs'. Compared to the single-loop coil, the quadrature coil's SNR is improved by at least a factor of $\sqrt{2}$ for all scans. With and without the enhancing coil, the birdcage coil has significantly lower SNR than all the others.

The signal squares' central horizontal and vertical lines in the MRI images were plotted separately for the three different scans. The plots for the CN-197 scan also include the lines after correction with the DAM method for the quadrature coil and the enhancing coil inside the birdcage coil. This correction was only done for the CN-197 scan.

Figures 4.35, 4.36, and 4.37 show the vertical line plots for scans CN-197, CN-1442, and CN-2552, respectively. The vertical line plot for the CN-197 sequence shows a narrow peak of the signal intensity, i.e., a limited sensitivity depth, for Prior Design Two compared to the other surface coils, i.e., Prior Design One, the single-loop coil,

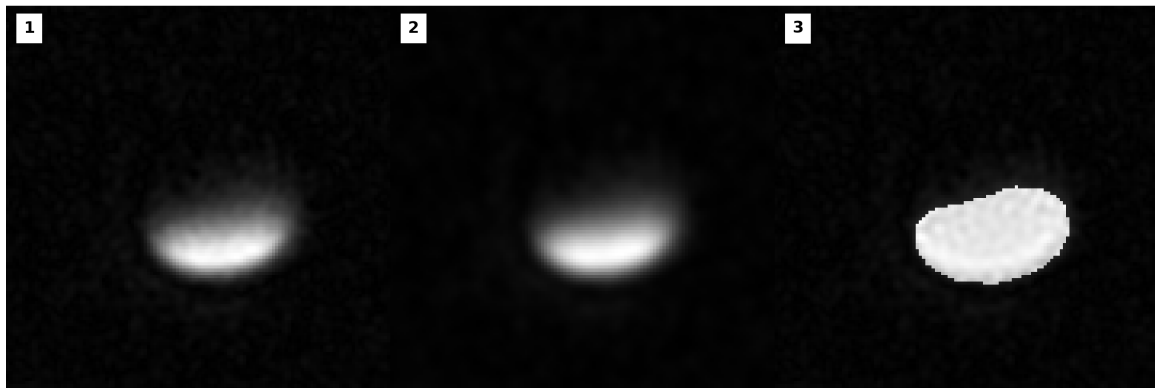


Figure 4.28: *Blurred B1 correction example for the single-loop coil* – 1) The original image acquired with the CN-197 scan (table 3.1) and the single-loop coil 2) blurred version of the image using a normalized 3x3 box blur, 3) the corrected image using the blurred image with a threshold of 0.15.

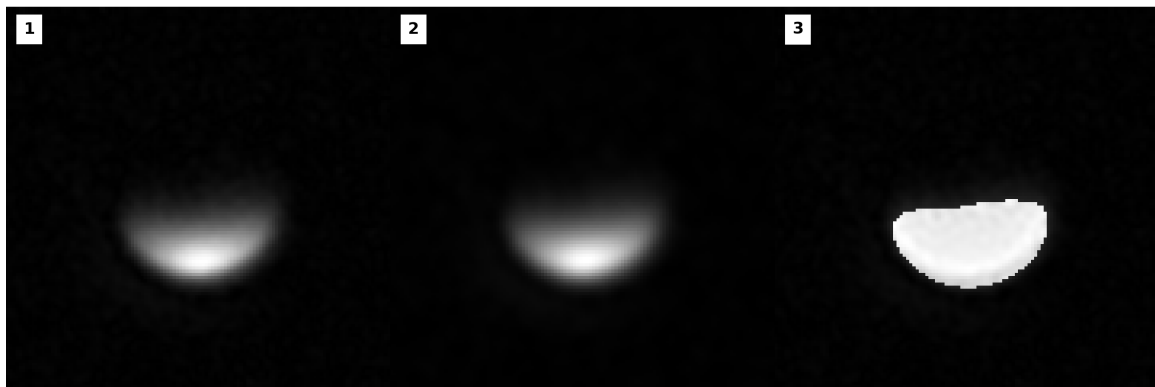


Figure 4.29: *Blurred B1 correction for the quadrature coil* – 1) The original image acquired with the CN-197 scan (table 3.1) and the quadrature coil 2) blurred version of the image using a normalized 3x3 box blur, 3) the corrected image using the blurred image with a threshold of 0.15.

and the quadrature coil. The quadrature coil image corrected by DAM seems to have a slightly larger sensitivity depth. The scans involving the birdcage have received a significant signal from the entire sample volume, and the scans involving the enhancing coil have an increased signal close to the enhancing coil. The same tendencies but less apparent can be found in the vertical line plots for the CN-1442 and the CN-2552 scans.

Figures 4.38, 4.39, and 4.40 show the horizontal lineplots. Each line crosses the center of the SNR signal square, which places the line about three centimeters into the phantom. The desire for a signal strength above 50% is met at this depth for all coils in all three scans, but most clearly in scan CN-197. Prior Design Two and the quadrature coil without correction has the narrowest view in scan CN-197. The DAM corrected quadrature coil has a wider view, and the birdcage coil alone has the widest. The single-loop coil has the steepest fall on both edges and a wide view, only second to the birdcage coil. The DAM-corrected birdcage coil scan with the enhancing coil has a significantly lower signal intensity than all the others, and the intensity increases from

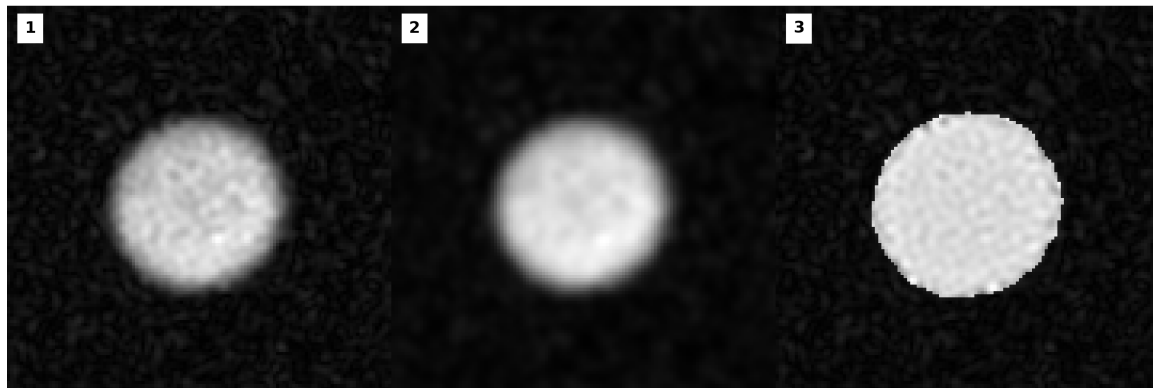


Figure 4.30: *Blurred B1 correction for the birdcage coil* – 1) The original image acquired with the CN-197 scan (table 3.1) and the birdcage coil 2) blurred version of the image using a normalized 3x3 box blur, 3) the corrected image using the blurred image with a threshold of 0.15.

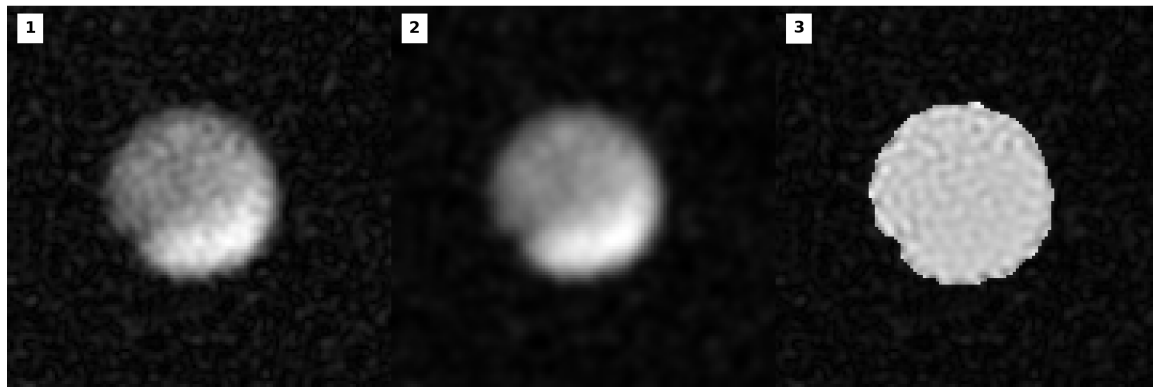


Figure 4.31: *Blurred B1 correction for the enhanced birdcage coil* – 1) The original image acquired with the CN-197 scan (table 3.1) and the enhanced birdcage coil 2) blurred version of the image using a normalized 3x3 box blur, 3) the corrected image using the blurred image with a threshold of 0.15.

right to left. The horizontal line plots for the other two scans, CN-1442 and CN-2552, are noisy but show that all coils can image the entire width of the phantom at this depth.

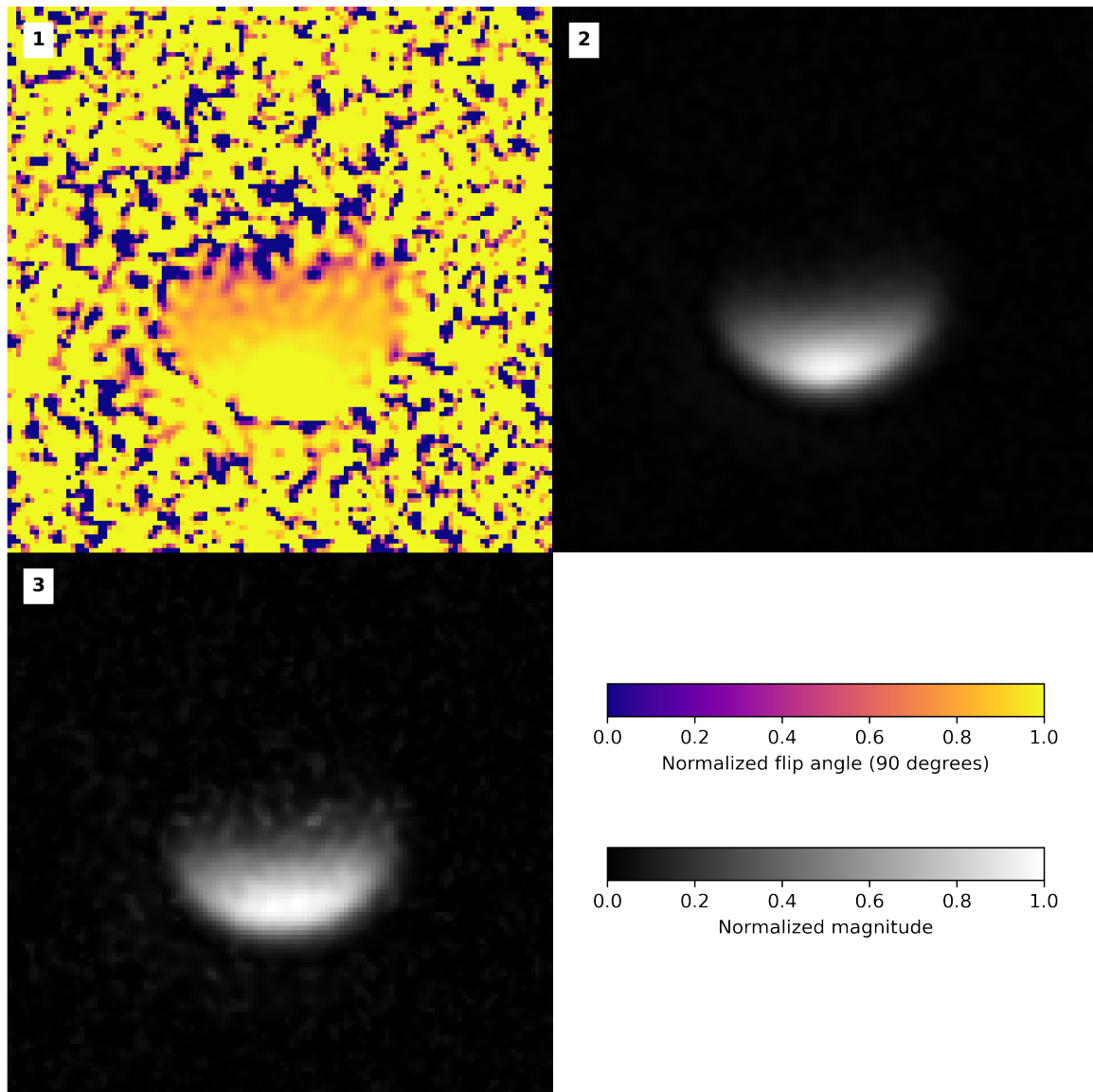


Figure 4.32: *B1* field map correction for the quadrature coil – 1) A flip angle map created with the DAM method, 2) the original image, 3) the corrected image after multiplication with the flip angle map.

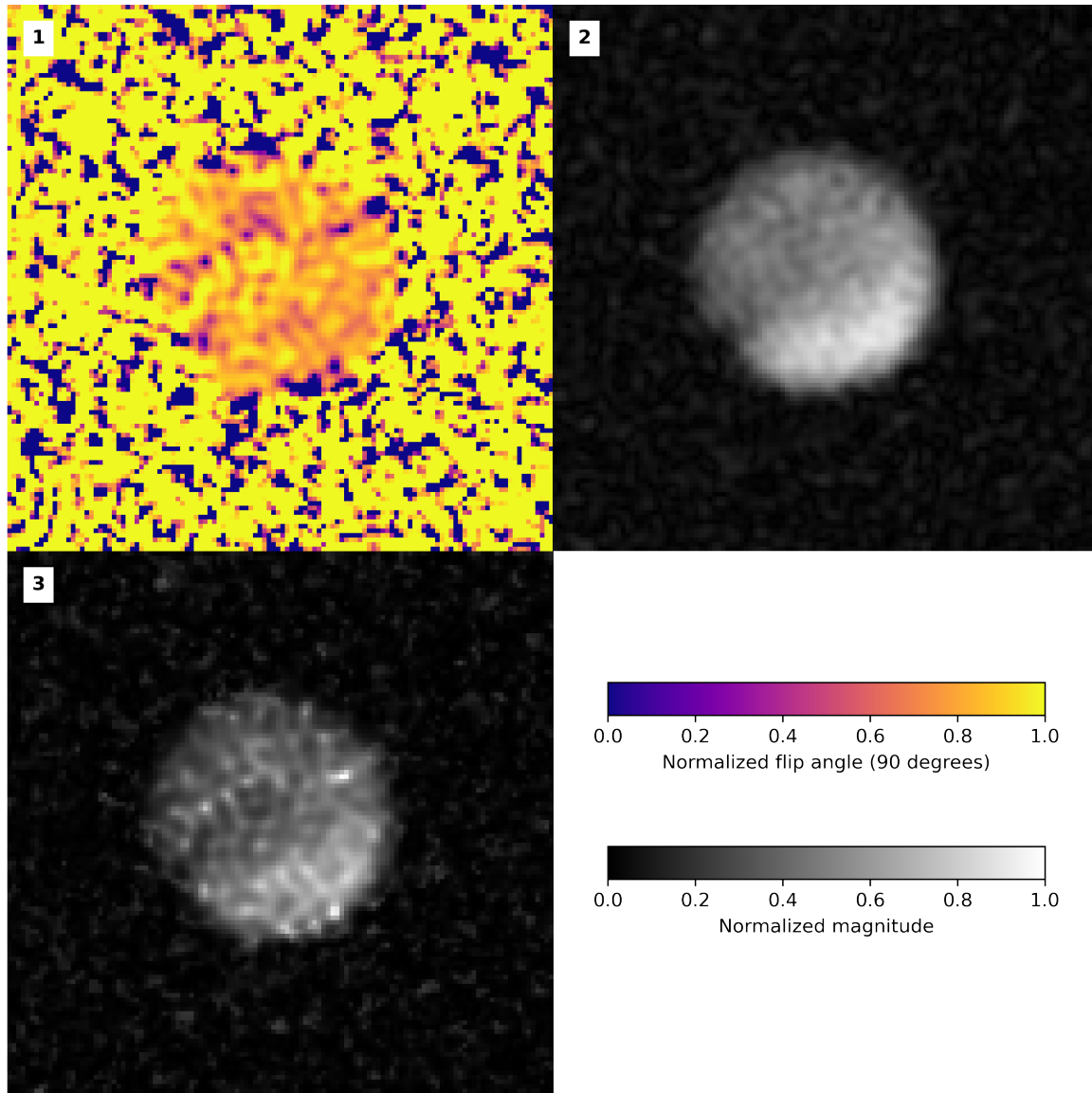


Figure 4.33: *B1 field map correction for the enhanced birdcage coil* – 1) A flip angle map created with the DAM method, 2) the original image, and 3) the corrected image after multiplication with the flip angle map.

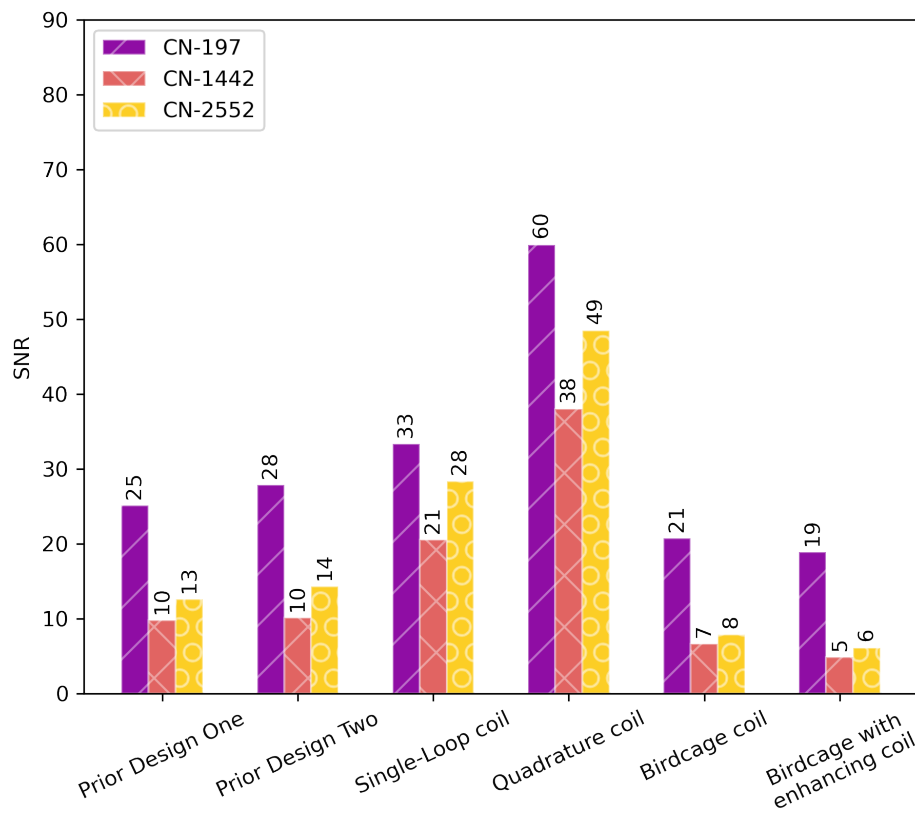


Figure 4.34: *SNR values calculated from phantom images for all coils.* – Calculated SNR values from MRI images of the chosen cylindrical phantom for all coils at the three different sequences (Table 3.1).

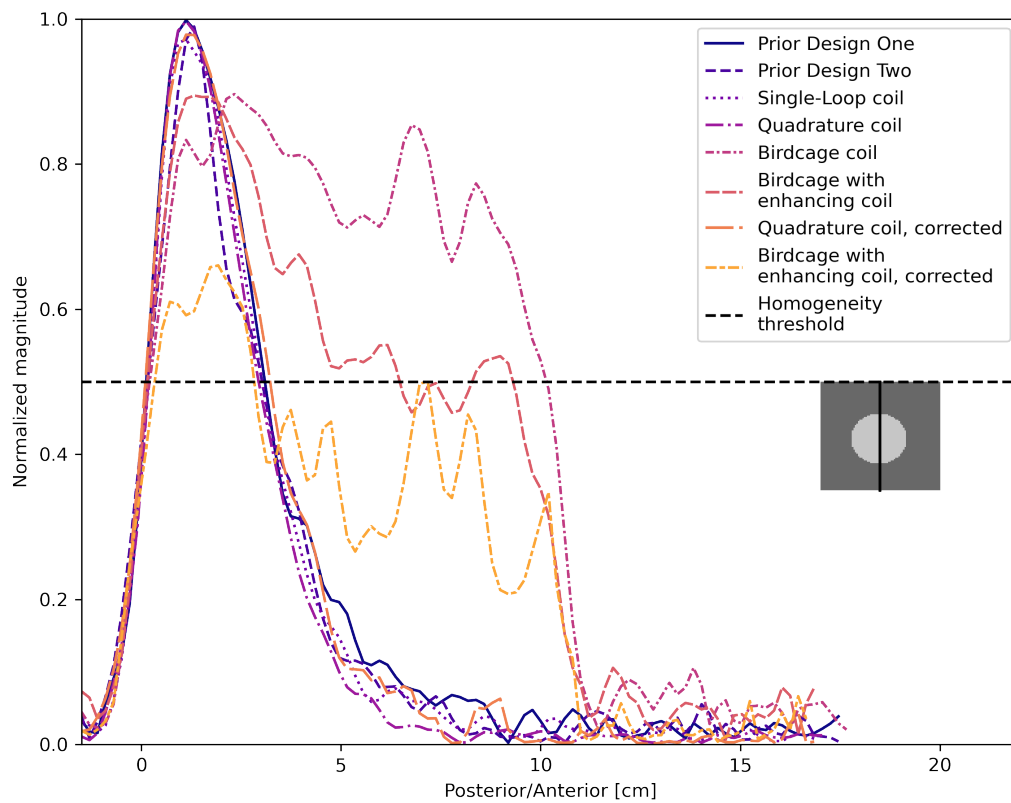


Figure 4.35: *Signal intensity comparison, vertical line plot of the CN-197 scans* – A comparison of the normalized intensity along a vertical line penetrating the phantom center in the CN-197 scan (Table 3.1) for all the tested coils. A black line indicates the plotted values in the small image of the circular phantom in transversal view.

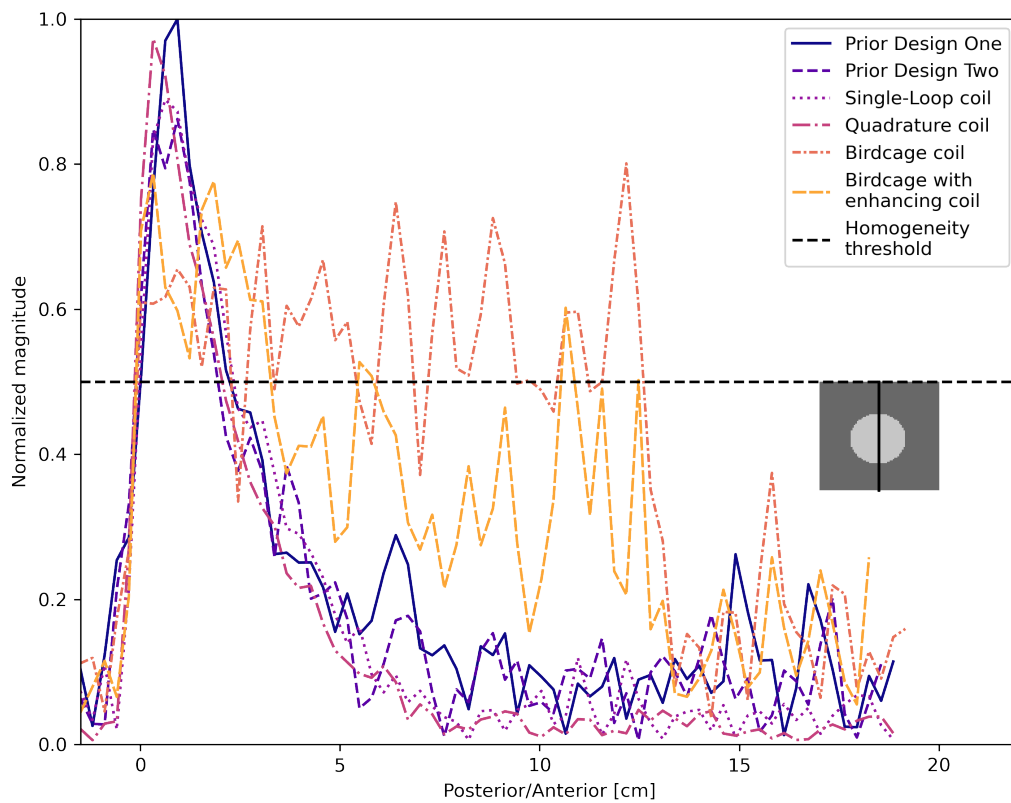


Figure 4.36: *Signal intensity comparison, vertical line plot of the CN-1442 scans* – A comparison of the normalized intensity of a vertical line penetrating the phantom center in the CN-1442 scan (table 3.1) for all the tested coils. A black line indicates the plotted values in the small image of the circular phantom in transversal view.

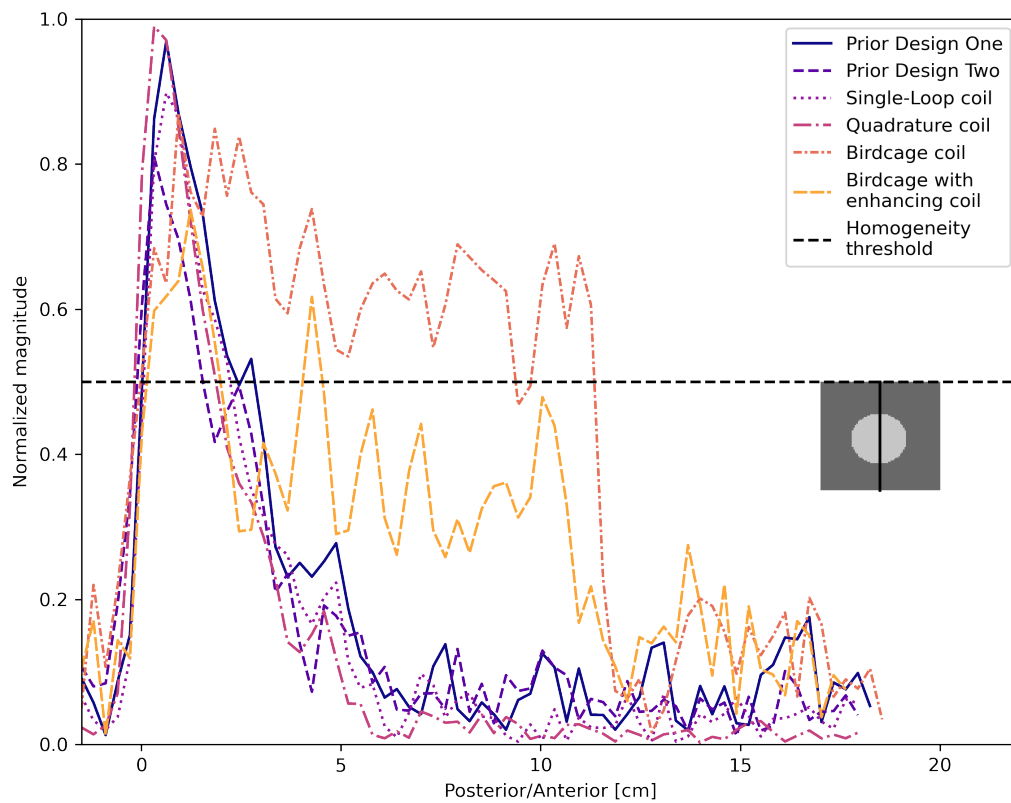


Figure 4.37: *Signal intensity comparison, vertical line plot of the CN-2552 scans* – A comparison of the normalized intensity of a vertical line penetrating the phantom center in the CN-2552 scan (table 3.1) for all the tested coils. A black line indicates the plotted values in the small image of the circular phantom in transversal view.

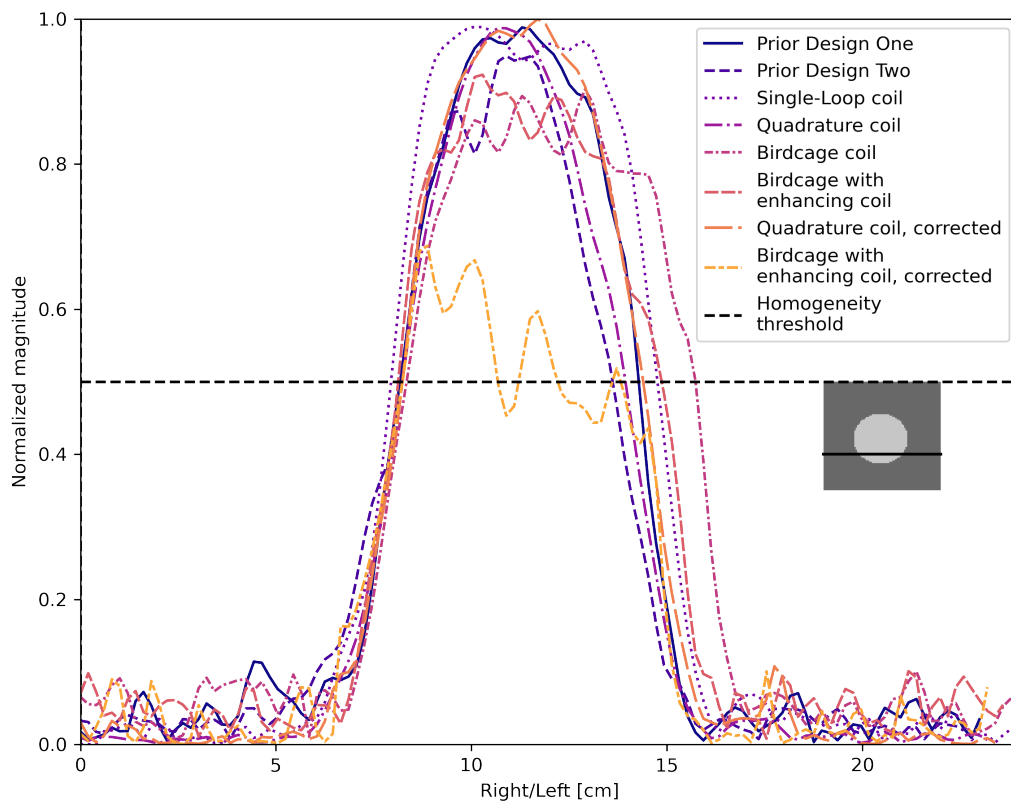


Figure 4.38: *Signal intensity comparison, horizontal line plot of the CN-197 scans* – A comparison of the normalized intensity of a horizontal line approximately three centimeters into the phantom in the CN-197 scan (table 3.1) for all the tested coils. A black line indicates the plotted values in the small image of the circular phantom in transversal view.

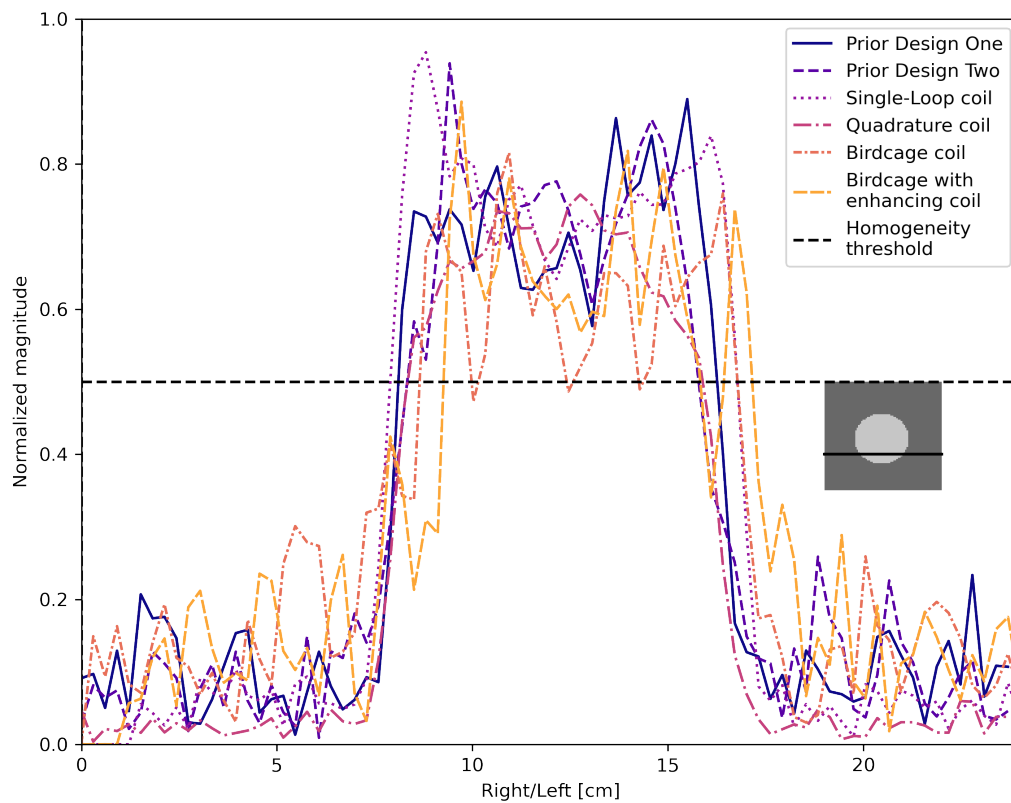


Figure 4.39: *Signal intensity comparison, horizontal line plot of the CN-1442 scans* – A comparison of the normalized intensity of a horizontal line approximately three centimeters into the phantom in the CN-1442 scan (table 3.1) for all the tested coils. A black line indicates the plotted values in the small image of the circular phantom in transversal view.

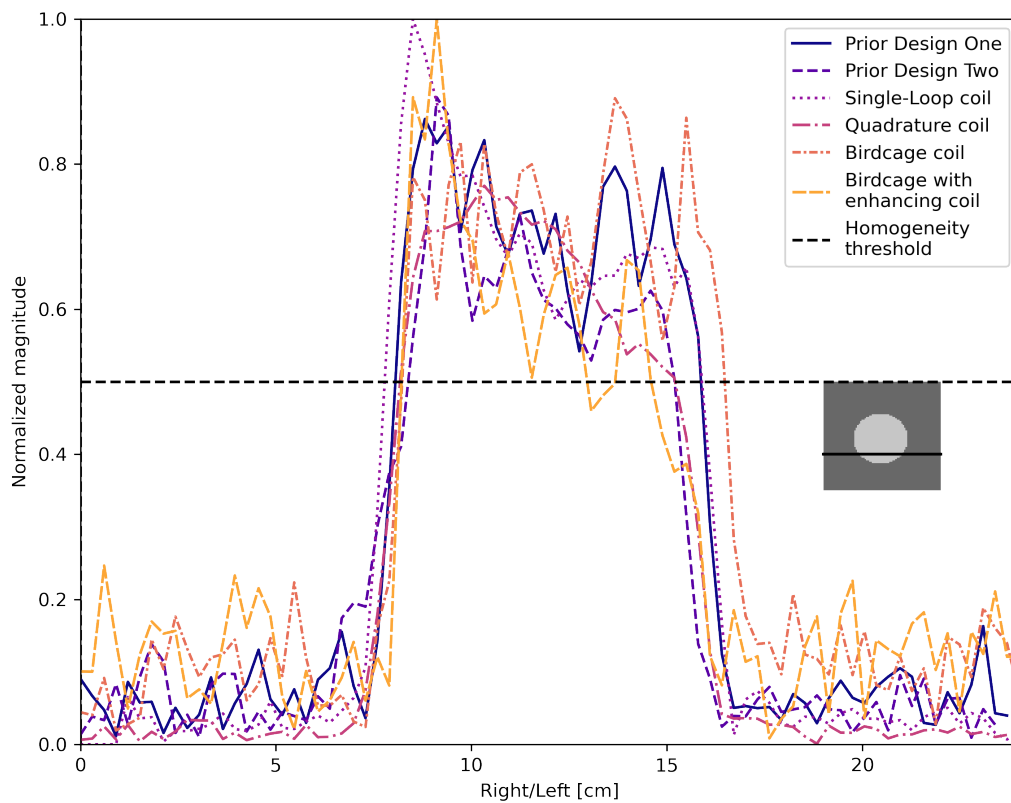


Figure 4.40: *Signal intensity comparison, horizontal line plot of the CN-2552 scans* – A comparison of the normalized intensity of a horizontal line approximately three centimeters into the phantom in the CN-2552 scan (table 3.1) for all the tested coils. A black line indicates the plotted values in the small image of the circular phantom in transversal view.

Chapter 5

Discussion

The main goal of this thesis was to develop three different surface coils for ^{23}Na -MRI with an improved SNR in the region of the visual cortex in the human brain. An improvement in SNR was compared to a commercially available 16-rod double-tuned birdcage coil from RAPID Biomedical and two general-purpose single-tuned surface coils. Two transceiver coils, the single-loop and quadrature coils, were designed, planned, and developed before they were compared to the other coils. A third coil element, the enhancing coil, was developed for enhancing the birdcage coil's reception field in the specified ROI. The two transceiver coils have a significantly improved SNR compared to the birdcage coil, and the quadrature coil also outperformed the general-purpose surface coils. The enhancing coil, however, did not improve the SNR, and the field enhancement occurred in an unexpected area. An explanatory theory of the enhancement was formed through approximate static magnetic field calculations. All coils included in this work, except the birdcage coil, were compared by laboratory measurements. Furthermore, all coils were compared by thoroughly inspecting acquired MRI data. The results indicate that the developed coils will have increased sensitivity for the desired ROI, i.e., the visual cortex a few centimeters into the human brain, and are positive additions to the range of available ^{23}Na -MRI coils. This chapter discusses the development process and the final coils' advantages and limitations.

The three designs were planned and realized through a literature review and collaboration with the Max Planck Institute of Biological Cybernetics in Tübingen, Germany. The 3D-designed coil holders were designed through several rounds of supervisor feedback before a planned trip to Tübingen. At the Max Planck Institute, equipment was made available to test different designs and acquire empirical knowledge of how to engineer an RF coil through trial and error rather than theoretical planning. The preparation for the trip to Tübingen had been challenging for the physics student without a specialization in electronics, needing an introduction to several RF topics before the specific considerations for RF coil development could be introduced. The short visit to Tübingen resulted in a swift realization of the coil designs. During the planning and design of the coil holders, the space needed for overlapping the two loops of the quadrature coil was underestimated, resulting in two squares with side lengths 8.5cm instead of 9.0cm , as was initially planned. A travel report of the visit to Tübingen is

included in Appendix B. The work up to and including the visit to Tübingen was presented as a poster at the MMIV conference in December 2023. The poster is included in Appendix C.

Several obstacles were met in connecting the coils to the MRI scanner. Specifications for the ^{23}Na T/R switch were not found. An adapter with two BNC connectors marked "Rx" and "Tx" was available, but no other hints pointed towards this being an adapter for quadrature driving. Without the specifications available, the decision to build the quadrature coil was based on reading about RF coil development and quadrature driving. The reading left the impression that the adapter was for quadrature driving. Another obstacle was encountered when the coils were to be tested in the MRI for the first time, and none of the ^{23}Na coils would yield any signal, not even the commercially available birdcage coil. This mystery was investigated in a group and through communication with the MRI manufacturer. Fortunately, after two months, the local engineers found a problem with the scanner system, sorted it out, and the coils could be tested in the MRI scanner.

The single-loop and quadrature coils were tuned and matched to the resonance frequency of ^{23}Na . The laboratory measurements investigating the coils' tuning and matching revealed excellent properties and successful designs. The already available coils, Prior Design One and Prior Design Two, had less satisfactory results. The Q-ratio of the single-loop and quadrature coils were double that of the Prior Design One and Prior Design Two. The achievable Q-ratios of ^{23}Na coils are generally lower than for hydrogen coils because of elevated RF losses in the sample volume at lower frequencies. However, a Q-ratio above 3 is desirable [13], and this was achieved for the two developed transceiver coils but not for the already available surface coils. The electronics of the prior designs were not studied in detail, but the applied components could be a reason for the sub-optimal results. The phantom resembling a human head could be another reason, as these are general-purpose surface coils and should provide adequate results for structures of different sizes than the human head.

The Hybrid responsible for driving the quadrature coil in quadrature should ideally split the power equally and provide a phase difference of 90° degrees between the power supplies to the loop elements during transmission and combine the two received signals with a phase difference -90° during reception. The two coil elements had to be decoupled appropriately to drive them in quadrature. The inductive decoupling resulted in transmission coefficients, S_{12} and S_{21} , of about -17dB at resonance, which allowed for independent tuning. The coupling is only an issue at resonance when significant current runs in the loops, increasing the potential for mutual inductance. The Hybrid provided a phase shift of 85° , less than intended. The offset is probably a result of the adjustment procedure, which was done by observing the magnitude plots of the S-parameters shown in Figure 4.17, especially plots (c-f), instead of focusing on the phase. As exemplified in Figure 2.26, a Hybrid with 85° phase shift will produce a circularly polarized field in the region where field lines of the two magnetic fields are orthogonal but simultaneously produce a weak circularly polarized field rotating in the opposite direction. However, no opposite component will be produced in a region where the field lines meet at 85° . In other words, the most effective circularly polarized field will be in a slightly different region than visualized in the field calculations.

MRI scans with the quadrature coil were performed with the correct coaxial cables attached to the transmit and receive ports of the T/R switch. Considering the phase difference introduced by the Hybrid and the working principle of a Hybrid in Figure 2.27, the right side loop connected to the same side of the Hybrid as the transmit port will have phase 0 degrees and the left side loop connected across from the transmit port will have phase +85 degrees. By looking at the image of the quadrature coil in Figure 4.13, the current direction in the right side loop will be opposite to that in the left side loop because the matching circuits are reversely connected to the coaxial cables. In the illustration of the circularly polarized field created by the quadrature coil in Figure 4.6 with the z-axis disappearing into the paper, the direction of the field is the same as what would be produced above two coils oriented in the same way as the ones on the quadrature coil. The static field calculations rotate against the clock, and the precessional motion of a spin system with a positive gyromagnetic ratio is also against the clock, as illustrated in Figure 2.2. The attachment of the coaxial cables confirms that the field induced during transmission has the expected precessional direction of an atom with a positive gyromagnetic ratio like ^{23}Na [50].

The enhancing coil was developed to explore the possibilities of enhancing the field of a birdcage coil. The Q-ratio and S_{11} parameters were not relevant to compare to the other coils because it does not include a connection to the MRI machine. The single-loop pick-up probe shown in Figure 4.11 was used to tune the coil, but the inductive matching of this probe to the enhancing coil was not prioritized. The coil is not perfectly tuned, but the S_{11} magnitude at 33.78MHz indicates that an RF field oscillating at the ^{23}Na frequency will induce a signal in the coil, which will be enough to explore the enhancing idea.

All coils were used to scan the selected phantom in Figure 3.7 three times with three different scanning parameters. The left impression of the three different scanning regimes is that scan CN-197 produces the most blurry image, making the phantom seem small compared to scans CN-1442 and CN-2552, which presents more noisy images. These impressions can be explained through the resolution and the undersampling ratio for the three scans presented in Table 3.1. Scan CN-197 had a resolution of $4.5 \times 4.5 \times 4.5\text{mm}^3$ and a k-space sampling of 10%, both lower for this scan than the other two. A lower sampling ratio of k-space introduces noise. However, there is less noise in the CN-197 scans than in scans CN-1442 and CN-2552. Probably because of the lower resolution of the CN-197 scan. The reconstruction matrix of scan CN-197 was 120×120 and not 80×80 as for the other two scans, which might have resulted in a different noise distribution. The low resolution before interpolation has increased the edge blurring because the edge signal was spread between the interpolated pixel values. Scans CN-1442 and CN-2552 had a resolution of $3 \times 3 \times 3\text{mm}^3$ but differed in k-space sampling ratios with 12% and 25%, respectively. The CN-1442 scans have increased noise in the background compared to scan CN-2552, likely because of the reduced k-space sampling.

All the presented transceiver surface coils produced at least one image where the circular shape of the phantom could be recognized easily, except for Prior Design Two. The scans acquired with the single-loop and quadrature coils in Figures 4.20 and 4.23, respectively, show shapes resembling a crescent moon because they are sensitive to a

more extensive part of the phantom. The favorable geometric shapes of the developed transceiver coils wrapping around the phantom are likely reasons for this observation. More of the wire is close to the phantom, which means that the RF waves have a shorter length of travel. The signal falls off with distance into the phantom, and the single-loop shows a more bent line than the Prior Design One in scan CN-2552, aligning with the flat geometry of Prior Design One compared to the bent single-loop. The quadrature coil shows almost half of the phantom perimeter, which makes sense as the two loops combined cover a bent shape of 15cm underneath the coil holder, while the single-loop coil only covers 9cm. Comparing the B_1 corrected images of scan CN-197 for the Prior Design One, Prior Design Two, single-loop, and quadrature coils show an advantage of the bent coil shape by a more half-moon shaped corrected area for the single-loop coil, but especially for the quadrature coil. The scans performed with the quadrature coil have a significantly more highlighted small area immediately inside the phantom. This highlight is probably where the magnetic field lines meet at 85° , and a proper circularly polarized field exists. The area is small, as indicated by the static field calculations illustrating the circularly polarized field of the quadrature coil. The background of scans CN-1442 and CN-2552 are more noisy for the prior designs than for the single-loop and the quadrature coils. The noisy background can be explained by the prior designs' less optimal tuning and matching. The prior designs' high return losses at the ^{23}Na frequency result in a weaker transmit signal and a reduction in the received signal to the MRI system.

The enhancing coil was placed in the center underneath the phantom inside the birdcage coil, but the enhancement in the MRI scans was shifted to the right side of the coil, and a weaker signal appeared to the left. The static magnetic field calculations of a cycle of the rotating field inside the coils in Figure 4.7 showed both an enhanced and a suppressed region, except when the field lines are vertically oriented when the enhancement is symmetrical. The field calculations can explain the shifted enhancement. Alone, the enhancing coil's field profile resembles the single-loop coil's field profile shown in Figure 4.3. The current direction in the enhancing coil switches when the birdcage coil's field component perpendicular to the enhancing coil's area switches between decreasing and increasing. The rotating field inside the birdcage coil also changes between a positive and negative perpendicular component. These two changing factors result in an enhancement skewed to one side through the field's rotation cycle but with opposite signs. The enhanced side of the static field calculations is opposite of the enhanced side of the MRI images in Figure 4.22, but this is due to the arbitrarily chosen directions of current in the static field calculations. The static magnetic field calculations assumed that the coil setup was used for transmission, but in this thesis, the enhancing coil was detuned during transmission and only active during reception. However, by the principle of reciprocity, the intensity pattern of the transmission field will be the same for the reception field with the same setup, just with the opposite phase change [83]. The static field calculations do not present an accurate simulation of the magnetic flux density inside the birdcage coil during transmission, but the relative differences are likely to apply. If the enhancing coil could be placed on the center's left side, the ROI would be enhanced.

Central vertical lines from all CN-197, CN-1442, and CN-2552 scans were plotted

in Figures 4.35, 4.36, and 4.37, and all lines were aligned to the point where the normalized intensity reached 0.4. The positioning of the phantom could have been done more precisely during the acquisitions to avoid the need to align the lines. The vertical line plots indicate that Prior Design One and the single-loop and quadrature coils perform similarly in the central line of the phantom when the signal is normalized to the image maximum. The curve of Prior Design Two has a slightly narrower peak compared to the other surface coils in all three vertical line plots. The magnetic field of this design should be approximately similar to the one displayed for a circular wire loop in Figure 2.12, which has a diameter of 15cm, as do Prior Design Two. However, this does not seem to be the case. The irregular shape of the field can be caused by magnetic materials in the coil. The scans acquired with the birdcage coil with and without the enhancing coil inside have received signals from the entire phantom. The enhancing coil lines show an enhanced signal close to the enhancing coil and a fall-off toward the phantom center, and the enhancement makes the mean of the normalized intensity lower for the unenhanced parts of the phantom compared to the birdcage scan. These effects are most prominent in the vertical line plot of scan CN-197 but are also recognizable from the other two. The peak of the line from the enhanced birdcage scan does not reach a value of one, probably because the normalization was to the maximum value of the entire imaged slice, and the enhancement was skewed to the left. The vertical line plots for scan CN-197 also included lines from the images corrected with the DAM from the quadrature and enhanced birdcage coil scans. The line from the corrected quadrature coil has a slightly wider peak than the uncorrected one, which indicates a more homogeneous receive field, although the improvement is tiny. However, the corrected image in Figure 4.32 (3) shows a larger bright region, which indicates a broader region of homogeneous signal in the center compared to the uncorrected image in Figure 4.32 (2). The field map for the quadrature coil in Figure 4.32 (1) managed to capture the trends of signal change and enhance the weaker signals. The line from the corrected enhanced birdcage coil scan indicates a reduction of the overall signal amplitude without softening the signal fall-off towards the phantom center, which is confirmed by visually comparing the original and the corrected image in Figure 4.33 (2) and (3). The noise seems to have restricted the DAM method's ability to capture the field inhomogeneities.

The horizontal line plots in figures 4.38, 4.39, and 4.40 illustrate the width of the field homogeneity approximately three centimeters into the phantom for scans CN-197, CN-1442, and CN-2552, respectively. The plot for the CN-197 scan is the most informative and is discussed here. The plot shows a relatively narrow peak of the quadrature coil line, probably because of the small highlighted central region with a circularly polarized field. The single-loop coil's region with signal strength above 50% is 8cm wide, only one centimeter wider than the quadrature coil's. The peaks of the lines of the prior designs are also narrower than the single-loop coil's, which can be explained by the geometric shape of the single-loop coil wrapping around the phantom. This theory is supported by the split peak of the single-loop line, indicating that the single-loop coil is less sensitive in the middle. The quadrature coil lines' peaks are not split because the region of the circularly polarized field is centered in the phantom. The corrected version of the quadrature coil has a peak as wide as the single-loop coil's peak because of the inhomogeneity correction with the DAM method. The lines

from the birdcage coil with the enhancing coil show a slightly stronger signal to the left, aligning with the enhancement seen in the image for the CN-197 scan. All coils image the entire width of the phantom at this depth because the penetration depth, approximated by the coil radius, is more than 3cm for all coils in this thesis.

The SNR values reflect the expected coil performance from laboratory measurements and magnetic field calculations. Neither of the prior designs is perfectly tuned and matched to the conditions of the experiment, which is a probable reason for the slightly lower SNR measurements compared to the single-loop coil. The shape of the single-loop coil is less probable to affect the SNR measurement because the measurement is done in a small central area. The difference in SNR is most prominent for scans CN-1442 and CN-2552, which is reflected by the elevated noise in the background of the MRI images acquired with the prior designs compared to the background of the single-loop coil scans. The quadrature coil's SNR towers over the rest in Figure 4.34. As expected, the SNR of the quadrature coil is improved by a factor of $\approx \sqrt{2}$ compared to the single-loop coil. The improvement beyond $\sqrt{2}$ might be because the loops of the quadrature coil are slightly smaller and overlap in the middle, bringing the wires closer to the sample region. The birdcage coil alone has a low SNR compared to the transceiver coils, and with the enhancing coil inside, the birdcage coil's SNR is even lower. Birdcage coils are known to have lower SNR than surface coils, even though they are driven in quadrature.

Material choices could influence the image quality and produce noise. From table 2.3, it is clear that neither PET-G nor PLA have magnetic susceptibility of significance. The passive components used, i.e., the capacitors, wires, inductors, and diodes, were specifically chosen because of their non-magnetic materials and MRI compatibility. The capacitors and inductors had high SR to withstand the high voltage. No apparent inhomogeneity artifacts are visible in the MRI images acquired with the coil designs developed in this thesis. As expected from the field calculations shown in Figures 4.3 and 4.5, the signal intensity falls off with distance from the coil. Inhomogeneity artifacts did appear in the images acquired with Prior Design Two, which does not show a round shape. The phantom seems more egg-shaped here than in the other MRI images. Some magnetic materials in the coil components can cause this shape change.

The ultimate goal of this project was to image human brains with the developed coils. The phantom resembles a person's head, except for the cylindrical shape. The coils may perform slightly differently when scanning a person's head than reported here. However, the variable tuning and matching capacitors in the single-loop and quadrature coils can adjust for this. A more pressing issue to address before the coils can be used for in vivo imaging is safety measures. Suppose the MRI machine is to fail and pour an overly large current amplitude through the coils. In that case, nothing will stop the coils from transferring more energy to the sample, resulting in a high SAR potentially dangerous to the patient. Another concern is that the components can heat up if their SR is met and start acting differently than intended. Although this is unlikely to occur if the correct sequences are run with the coils, safety measures provide additional assurance. A fuse could be placed in the circuit to stop current from flowing when the voltage rises above a threshold, avoiding a high SAR. A thorough evaluation of SAR and safety requires specialized software and human tissue models [81].

Chapter 6

Conclusions and Future Work

This project aimed to build a surface coil with high ^{23}Na -MRI sensitivity to a small Region of Interest (ROI). The design and implementation of three designs were completed, and their performances were analyzed against a commercial and two other pre-existing designs. Designs of this thesis proved significantly better in the defined ROI.

The two transceiver surface coils, the single-loop and quadrature coils, achieved an increased SNR compared to the birdcage coil and two general-purpose surface coils used for comparison. The quadrature coil has superior results because it produces a circularly polarized field in the ROI. Both coils received a signal above 50% of the maximum signal in a region 3-4 cm into the phantom and 7-8 cm wide. The circularly polarized magnetic field increases the quadrature coil's efficiency and SNR but reduces the magnetic field homogeneity compared to the single-loop coil. Inhomogeneity corrections using a B_1 field map created with the DAM method improved images acquired with the quadrature coil. By tuning and matching the prior designs again, they could probably achieve similar SNR values to those of the single-loop coil but in a slightly smaller region because of the single-loop coil's bent shape. The SNR values of the quadrature coil will remain out of reach because of the advantages of a circularly polarized field compared to a linearly polarized field.

A second resonator to enhance the field of a birdcage coil was also developed, and promising results were presented. However, the position of the enhanced region was skewed relative to the placement of the enhancing loop. A theory explaining the displacement of the enhanced region was proposed, but it needs to be confirmed. Careful positioning of the enhancing coil relative to the object to be imaged could enhance the ROI with more success. Changes in scanner parameters and transmit gain could also improve the results for this design and can be explored in future projects.

Because of the promising results from this thesis, exploring the coils' properties in vivo could also be of interest as a future outlook. However, safety measures should be installed before these coils are used in vivo to ensure acceptable SAR values in the sample and avoid overheated components. With these additional installations, the coils can be used to plan and conduct studies to extend the current work.

Bibliography

1. Brown RW and al. et. Magnetic Resonance Imaging: Physical Principles and Sequence Design. John Wiley and Sons, Inc., 1999. Chap. 1 Magnetic Resonance Imaging: A Preview:1–16
2. Gerlach W and Stern O. Der experimentelle Nachweis der Richtungsquantelung im Magnetfeld. Zeitschrift für Physik 1922; 9(1):349–52. DOI: [10.1007/BF01326983](https://doi.org/10.1007/BF01326983)
3. Rabi II, Kellogg JMB, and Zacharias JR. The Magnetic Moment of the Proton. Phys. Rev. 1934; 46(3):157–63. DOI: [10.1103/PhysRev.46.157](https://doi.org/10.1103/PhysRev.46.157)
4. Bloch F, Hansen WW, and Packard M. Nuclear induction. Phys. Rev. 1946; 69(3-4):127–7. DOI: [10.1103/PhysRev.69.127](https://doi.org/10.1103/PhysRev.69.127)
5. Purcell EM, Torrey HC, and Pound RV. Resonance Absorption by Nuclear Magnetic Moments in a Solid. Phys. Rev. 1946; 69(1-2):37–8. DOI: [10.1103/PhysRev.69.37](https://doi.org/10.1103/PhysRev.69.37)
6. Lauterbur PC. Image Formation by Induced Local Interactions: Examples Employing Nuclear Magnetic Resonance. Nature 1973; 242:190–1. DOI: [10.1038/242190a0](https://doi.org/10.1038/242190a0)
7. Mansfield P and Maudsley AA. Medical imaging by NMR. The British journal of radiology 1977; 50(591):188–94. DOI: [10.1259/0007-1285-50-591-188](https://doi.org/10.1259/0007-1285-50-591-188)
8. Faraday M. Experimental researches in electricity: reprinted from the Philosophical Transactions of 1831-1843, 1846-1852. Vol. 2. R. and JE Taylor, 1839
9. Maxwell JC. A Dynamical Theory of the Electromagnetic Field. The Royal Society (Great Britain) 1865. DOI: [10.5479/sil.423156.39088007130693](https://doi.org/10.5479/sil.423156.39088007130693)
10. Brown RW and al. et. Magnetic Resonance Imaging: Physical Principles and Sequence Design. John Wiley and Sons, Inc., 1999. Chap. 4 Magnetization, Relaxation and the Bloch Equations:51–65
11. Brown RW and al. et. Magnetic Resonance Imaging: Physical Principles and Sequence Design. John Wiley and Sons, Inc., 1999. Chap. 7 Signal Detection oncepts:93–110
12. Hilal SK, Maudsley AA, Ra JB, Simon HE, Roschmann P, Wittekoek S, Cho ZH, and Mun SK. In vivo NMR imaging of sodium-23 in the human head. Journal of computer assisted tomography 1985; 9(1). DOI: [10.1097/00004728-198501000-00001](https://doi.org/10.1097/00004728-198501000-00001)
13. Wiggins GC, Brown R, and Lakshmanan K. High-performance radiofrequency coils for ^{23}Na MRI: Brain and musculoskeletal applications. NMR in Biomedicine 2016; 29(2):96–106. DOI: [10.1002/nbm.3379](https://doi.org/10.1002/nbm.3379)

14. Madelin G, Lee JS, Regatte RR, and Jerschow A. Sodium MRI: Methods and applications. *Progress in Nuclear Magnetic Resonance Spectroscopy* 2014; 79:14–47. DOI: [10.1016/j.pnmrs.2014.02.001](https://doi.org/10.1016/j.pnmrs.2014.02.001)
15. Wang J, Ou SW, and Wang YJ. Distribution and function of voltage-gated sodium channels in the nervous system. *Channels (Austin)* 2017; 11(6):534–54. DOI: [10.1080/19336950.2017.1380758](https://doi.org/10.1080/19336950.2017.1380758)
16. Alberts B, Bray D, Hopkin K, Johnson A, Lewis J, Raff M, Roberts K, and Walter P. *Essential Cell Biology*. Fourth ed. Garland Science, 2014. Chap. 12 Transport Across Cell Membranes:383–418
17. Ogawa S, Lee TM, Kay AR, and Tank DW. Brain magnetic resonance imaging with contrast dependent on blood oxygenation. *Proc Natl Acad Sci U S A* 1990; 87(24):9868–72. DOI: [10.1073/pnas.87.24.9868](https://doi.org/10.1073/pnas.87.24.9868)
18. Glover GH. Overview of Functional Magnetic Resonance Imaging. *Neurosurgery Clinics of North America* 2011; 22(2):133–9. DOI: [10.1016/j.nec.2010.11.001](https://doi.org/10.1016/j.nec.2010.11.001)
19. Thulborn KR. Quantitative sodium MR imaging: A review of its evolving role in medicine. *NeuroImage* 2018; 168. *Neuroimaging with Ultra-high Field MRI: Present and Future*:250–68. DOI: [10.1016/j.neuroimage.2016.11.056](https://doi.org/10.1016/j.neuroimage.2016.11.056)
20. Huhn K, Engelhorn T, Linker RA, and Nagel AM. Potential of Sodium MRI as a Biomarker for Neurodegeneration and Neuroinflammation in Multiple Sclerosis. *Frontiers in Neurology* 2019; 10. DOI: [10.3389/fneur.2019.00084](https://doi.org/10.3389/fneur.2019.00084)
21. Hagiwara A, Bydder M, Oughourlian TC, Yao J, Salamon N, Jahan R, Villablanca JP, Enzmann DR, and Ellingson BM. Sodium MR neuroimaging. *American Journal of Neuroradiology* 2021; 42(11). DOI: [10.3174/ajnr.A7261](https://doi.org/10.3174/ajnr.A7261)
22. Wheeler-Kingshott CAG, Riemer F, Palesi F, Ricciardi A, Castellazzi G, Golay X, Prados F, Solanky B, and D'Angelo EU. Challenges and perspectives of quantitative functional sodium imaging (fNaI). *Frontiers in Neuroscience* 2018; 12(NOV). DOI: [10.3389/fnins.2018.00810](https://doi.org/10.3389/fnins.2018.00810)
23. Akbari A, Lemoine S, Salerno F, Marcus TL, Duffy T, Scholl TJ, Filler G, House AA, and McIntyre CW. Functional Sodium MRI Helps to Measure Corticomedullary Sodium Content in Normal and Diseased Human Kidneys. *Radiology* 2022; 303. PMID: 35133199:384–9. DOI: [10.1148/radiol.211238](https://doi.org/10.1148/radiol.211238)
24. Zaric O, Juras V, Szomolanyi P, Schreiner M, Raudner M, Giraudo C, and Trattnig S. Frontiers of Sodium MRI Revisited: From Cartilage to Brain Imaging. *Journal of Magnetic Resonance Imaging* 2021; 54(1):58–75. DOI: [10.1002/jmri.27326](https://doi.org/10.1002/jmri.27326)
25. Gast LV, Platt T, Nagel AM, and Gerhalter T. Recent technical developments and clinical research applications of sodium (^{23}Na) MRI. *Progress in Nuclear Magnetic Resonance Spectroscopy* 2023; 138-139:1–51. DOI: [10.1016/j.pnmrs.2023.04.002](https://doi.org/10.1016/j.pnmrs.2023.04.002)

26. Wilcox M, Wright SM, and McDougall M. A Review of Non-1H RF Receive Arrays in Magnetic Resonance Imaging and Spectroscopy. *IEEE Open Journal of Engineering in Medicine and Biology* 2020; (1):290–300. DOI: [10.1109/OJEMB.2020.3030531](https://doi.org/10.1109/OJEMB.2020.3030531)
27. Yen YF, Takahashi AM, and Ackerman JL. X-nuclear MRS and MRI on a standard clinical proton-only MRI scanner. *Journal of Magnetic Resonance Open* 2023; 16-17:100118. DOI: [10.1016/j.jmro.2023.100118](https://doi.org/10.1016/j.jmro.2023.100118)
28. Brown RW and al. et. *Magnetic Resonance Imaging: Physical Principles and Sequence Design*. John Wiley and Sons, Inc., 1999. Chap. 27 Introduction to MRI Coils and Magnets:827–62
29. Choi CH, Hong SM, Felder J, and Shah NJ. The state-of-the-art and emerging design approaches of double-tuned RF coils for X-nuclei, brain MR imaging and spectroscopy: A review. *Magnetic Resonance Imaging* 2020; 72:103–16. DOI: [10.1016/j.mri.2020.07.003](https://doi.org/10.1016/j.mri.2020.07.003)
30. Mispelter J, Lupu M, and Briguet A. *NMR Probeheads for Biophysical and Biomedical Experiments*. Second. Imperial College Press, 2015. Chap. 2 Radio Frequency Components:23–154
31. Barisano G, Seppehrband F, Ma S, Jann K, Cabeen R, Wang DJ, Toga AW, and Law M. Clinical 7 T MRI: Are we there yet? A review about magnetic resonance imaging at ultra-high field. *The British journal of radiology* 2019; 92(1094). DOI: [10.1259/bjr.20180492](https://doi.org/10.1259/bjr.20180492)
32. Wilferth T, Mennecke A, Gast LV, Lachner S, Müller M, Rothhammer V, Huhn K, Uder M, Doerfler A, Nagel AM, and Schmidt M. Quantitative 7T sodium magnetic resonance imaging of the human brain using a 32-channel phased-array head coil: Application to patients with secondary progressive multiple sclerosis. *NMR in biomedicine* 2022; 35(12). DOI: [10.1002/nbm.4806](https://doi.org/10.1002/nbm.4806)
33. Kaggie JD, Lanz T, McLean MA, Riemer F, Schulte RF, Benjamin AJV, Kessler DA, Sun C, Gilbert FJ, Graves MJ, and Gallagher FA. Combined ²³Na and ¹³C imaging at 3.0 Tesla using a single-tuned large FOV birdcage coil. *Magnetic Resonance in Medicine* 2021; 86(3):1734–45. DOI: [10.1002/mrm.28772](https://doi.org/10.1002/mrm.28772)
34. Giovannetti G, Flori A, Martini N, Francischello R, Aquaro GD, Pingitore A, and Frijia F. Sodium radiofrequency coils for magnetic resonance: From design to applications. *Electronics* 2021; 10:1788
35. Chen CN, Hoult DI, and Sank VJ. Quadrature Detection Coils-A Further sqrt(2) Improvement in Sensitivity. *Journal of Magnetic Resonance* 1983; 54(2):324–7. DOI: [10.1016/0022-2364\(83\)90057-4](https://doi.org/10.1016/0022-2364(83)90057-4)
36. Hayes CE and Axel L. Noise performance of surface coils for magnetic resonance imaging at 1.5 T. *Medical Physics* 1985; 12:604–7. DOI: [10.1118/1.595682](https://doi.org/10.1118/1.595682)
37. Park BS, Rajan SS, and McCright B. Sensitivity and uniformity improvement of phased array MR images using inductive coupling and RF detuning circuits. *Magnetic Reso-*

- nance Materials in Physics, Biology and Medicine 2020; 33(5):725–33. DOI: [10.1007/s10334-020-00827-7](https://doi.org/10.1007/s10334-020-00827-7)
38. Yan X, Zhang X, Gore JC, and Grissom WA. Improved traveling-wave efficiency in 7 T human MRI using passive local loop and dipole arrays. *Magnetic Resonance Imaging* 2017; 39:103–9. DOI: [10.1016/j.mri.2017.02.003](https://doi.org/10.1016/j.mri.2017.02.003)
 39. Hussain S, Mubeen I, Ullah N, Shah SSUD, Khan BA, Zahoor M, Ullah R, Khan FA, and Sultan MA. Modern Diagnostic Imaging Technique Applications and Risk Factors in the Medical Field: A Review. *BioMed Research International* 2022; 2022. DOI: [10.1155/2022/5164970](https://doi.org/10.1155/2022/5164970)
 40. Logothetis NK. What we can do and what we cannot do with fMRI. *Nature* 2008; 453(7197):869–78. DOI: [10.1038/nature06976](https://doi.org/10.1038/nature06976)
 41. Young H, Freedman R, Ford A, and Estrugo K. *University Physics with Modern Physics*. 15th ed. Pearson, 2019. Chap. 44 Particle Physics and Cosmology:1511–52
 42. Mispelter J, Lupu M, and Briguet A. *NMR Probeheads for Biophysical and Biomedical Experiments*. Second. Imperial College Press, 2015. Chap. Appendix A - Physical Constants and Useful Formulae:691–708
 43. Young H, Freedman R, Ford A, and Estrugo K. *University Physics with Modern Physics*. 15th ed. Pearson, 2019. Chap. 41 Quantum Mechanics II: Atomic Structure:1388–435
 44. Brown RW and al. et. *Magnetic Resonance Imaging: Physical Principles and Sequence Design*. John Wiley and Sons, Inc., 1999. Chap. 5 The Quantum Mechanical Basis of Precession and Excitation:65–82
 45. Brown RW and al. et. *Magnetic Resonance Imaging: Physical Principles and Sequence Design*. John Wiley and Sons, Inc., 1999. Chap. 2 Classical Response of a Single Nucleus to a Magnetic Field:17–34
 46. Brown RW and al. et. *Magnetic Resonance Imaging: Physical Principles and Sequence Design*. John Wiley and Sons, Inc., 1999. Chap. 6 The Quantum Mechanical Basis of Thermal Equilibrium and Longitudinal Relaxation:83–92
 47. Glazer M and Wark J. *Statistical mechanics*. 1st ed. Oxford University Press, 2001. Chap. 2 The Statistics of Distinguishable Particles:15–28
 48. Tofts PS. PD: Proton Density of Tissue Water. *John Wiley and Sons, Ltd*, 2003 :83–109. DOI: [10.1002/0470869526.ch4](https://doi.org/10.1002/0470869526.ch4)
 49. Brown RW and al. et. *Magnetic Resonance Imaging: Physical Principles and Sequence Design*. John Wiley and Sons, Inc., 1999. Chap. 3 Rotating Reference Frames and Resonance:35–50
 50. Mispelter J, Lupu M, and Briguet A. *NMR Probeheads for Biophysical and Biomedical Experiments*. Second. Imperial College Press, 2015. Chap. 5 Quadrature driving:295–344

51. Brown RW and al. et. Magnetic Resonance Imaging: Physical Principles and Sequence Design. John Wiley and Sons, Inc., 1999. Chap. 8 Introductory Signal Acquisition Methods: Free Induction Decay, Spin Echos, Inversion Recovery, and Spectroscopy:111–37
52. Brown RW and al. et. Magnetic Resonance Imaging: Physical Principles and Sequence Design. John Wiley and Sons, Inc., 1999. Chap. 10 Multi-Dimensional Fourier Imaging and Slice Selection:165–206
53. Brown RW and al. et. Magnetic Resonance Imaging: Physical Principles and Sequence Design. John Wiley and Sons, Inc., 1999. Chap. 9 One-Dimensional Fourier Imaging, k-Space, and Gradient Echos:138–64
54. Liang ZP and Lauterbur PC. Principles of Magnetic Resonance Imaging: A Signal Processing Perspective. Series on Biomedical Engineering. IEEE Press, 2000. Chap. 8 Image Resolution, Noise, and Artifacts:233–90
55. Schick F. Whole-body MRI at high field: Technical limits and clinical potential. *European Radiology* 2005; 15(5):946–59. DOI: [10.1007/s00330-005-2678-0](https://doi.org/10.1007/s00330-005-2678-0)
56. Glover GH, Hayes CE, Pelc NJ, Edelstein WA, Mueller M, Hart HR, Hardy CJ, O'donnell M, and Barber WD. Comparison of Linear and Circular Polarization for Magnetic Resonance Imaging. *Journal of Magnetic Resonance* 1985; 64:255–70
57. Brown RW and al. et. Magnetic Resonance Imaging: Physical Principles and Sequence Design. John Wiley and Sons, Inc., 1999. Chap. 20 Magnetic Field Inhomogeneity Effects and T2 star Dephasing:569–618
58. Haynes WE. *CRC Handbook of Chemistry and Physics*. Ed. by Haynes WM. 95th. CRC Press, 2014 :131–6
59. Wapler MC, Leupold J, Dragonu I, Elverfeld DV, Zaitsev M, and Wallrabe U. Magnetic properties of materials for MR engineering, micro-MR and beyond. *Journal of Magnetic Resonance* 2014; 242:233–42. DOI: [10.1016/j.jmr.2014.02.005](https://doi.org/10.1016/j.jmr.2014.02.005)
60. Niesporek SC, Nagel AM, and Platt T. Multinuclear MRI at Ultrahigh Fields. *Topics in Magnetic Resonance Imaging* 2019; 28:173–88. DOI: [10.1097/RMR.000000000000201](https://doi.org/10.1097/RMR.000000000000201)
61. Edmonds DT and Mailer JPG. Double Qaadrupole Resonance of Spin-3/2 Nuclei: ²³Na. *Journal of Magnetic Resonance* 1979; 36(3):411–8. DOI: [10.1016/0022-2364\(79\)90117-3](https://doi.org/10.1016/0022-2364(79)90117-3)
62. Parrish TB, Fieno DS, Fitzgerald SW, and Judd RM. Theoretical basis for sodium and potassium MRI of the human heart at 1.5 T. *Magnetic Resonance in Medicine* 1997; 38(4):653–61. DOI: [10.1002/mrm.1910380420](https://doi.org/10.1002/mrm.1910380420)
63. Gurney PT, Hargreaves BA, and Nishimura DG. Design and analysis of a practical 3D cones trajectory. *Magnetic Resonance in Medicine* 2006; 55(3):575–82. DOI: [10.1002/mrm.20796](https://doi.org/10.1002/mrm.20796)

64. Riemer F, Solanky BS, Stehning C, Clemence M, Wheeler-Kingshott CA, and Golay X. Sodium (^{23}Na) ultra-short echo time imaging in the human brain using a 3D-Cones trajectory. *Magnetic Resonance Materials in Physics, Biology and Medicine* 2014; 27(1):35–46. DOI: [10.1007/s10334-013-0395-2](https://doi.org/10.1007/s10334-013-0395-2)
65. Shannon C. Communication in the Presence of Noise. *Proceedings of the IRE* 1949; 37:10–21. DOI: [10.1109/JRPROC.1949.232969](https://doi.org/10.1109/JRPROC.1949.232969)
66. Paling D, Solanky BS, Riemer F, Tozer DJ, Wheeler-Kingshott CAM, Kapoor R, Golay X, and Miller DH. Sodium accumulation is associated with disability and a progressive course in multiple sclerosis. *Brain* 2013; 136(7):2305–17. DOI: [10.1093/brain/awt149](https://doi.org/10.1093/brain/awt149)
67. Sadiku MNO. *Elements of electromagnetics*. 3rd. Oxford University Press, 2001
68. Young H, Freedman R, Ford A, and Estrugo K. *University Physics with Modern Physics*. 15th ed. Pearson, 2019. Chap. 22 Gauss's law:746–74
69. Young H, Freedman R, Ford A, and Estrugo K. *University Physics with Modern Physics*. 15th ed. Pearson, 2019. Chap. 27 Magnetic Field and Magnetic Forces:906–45
70. Young H, Freedman R, Ford A, and Estrugo K. *University Physics with Modern Physics*. 15th ed. Pearson, 2019. Chap. 30 Inductance:1016–45
71. Bowick C, Blyler J, and Ajluni C. *RF circuit design*. 2nd ed. Elsevier Science, 2011. Chap. 1 Components and Systems:1–22
72. Young H, Freedman R, Ford A, and Estrugo K. *University Physics with Modern Physics*. 15th ed. Pearson, 2019. Chap. 31 Alternating current:1046–75
73. Mispelter J, Lupu M, and Briguet A. *NMR Probeheads for Biophysical and Biomedical Experiments*. Second. Imperial College Press, 2015. Chap. 1 Introduction:1–22
74. Terman FE. *Radio Engineers Handbook*. First. McGraw-Hill Company, Inc., 1943
75. Michael-Ortner et al. magpylib. Version 4.5.1. 2023 Jun 25. Available from: <https://magpylib.readthedocs.io/en/latest/>
76. Bowick C, Blyler J, and Ajluni C. *RF circuit design*. 2nd ed. Elsevier Science, 2011. Chap. 2 Resonant Circuits:23–36
77. Young H, Freedman R, Ford A, and Estrugo K. *University Physics with Modern Physics*. 15th ed. Pearson, 2019. Chap. 42 Molecules and Condensed Matter:1436–69
78. Bowick C, Blyler J, and Ajluni C. *RF circuit design*. 2nd ed. Elsevier Science, 2011. Chap. 5 The transistor at Radio Frequencies:103–24
79. Bowick C, Blyler J, and Ajluni C. *RF circuit design*. 2nd ed. Elsevier Science, 2011. Chap. 4 Impedance matching:63–102
80. Mispelter J, Lupu M, and Briguet A. *NMR Probeheads for Biophysical and Biomedical Experiments*. Second. Imperial College Press, 2015. Chap. 3 Introduction to Linear Network Analysis:155–96

81. Mispelter J, Lupu M, and Briguet A. NMR Probeheads for Biophysical and Biomedical Experiments. Second. Imperial College Press, 2015. Chap. 10 Probe Evaluation and Debugging:655–90
82. Rytting D. Network Analyzer Error Models and Calibration Methods. 1998
83. Hoult DI. The principle of reciprocity. *Journal of Magnetic Resonance* 2011; 213(2):344–6. DOI: [10.1016/j.jmr.2011.08.005](https://doi.org/10.1016/j.jmr.2011.08.005)
84. Gruber B, Froeling M, Leiner T, and Klomp DW. RF coils: A practical guide for non-physicists. *Journal of Magnetic Resonance Imaging* 2018; 48(3):590–604. DOI: [10.1002/jmri.26187](https://doi.org/10.1002/jmri.26187)
85. Mispelter J, Lupu M, and Briguet A. NMR Probeheads for Biophysical and Biomedical Experiments. Second. Imperial College Press, 2015. Chap. 9 Heterogeneous Resonators:601–54
86. Roemer PB, Edelstein WA, Hayes CE, Souza SP, and Mueller OM. The NMR Phased Array. *Magnetic Resonance in Medicine* 1990; 16(2):192–225. DOI: [10.1002/mrm.1910160203](https://doi.org/10.1002/mrm.1910160203)
87. Mispelter J, Lupu M, and Briguet A. NMR Probeheads for Biophysical and Biomedical Experiments. Second. Imperial College Press, 2015. Chap. 8 Homogeneous resonators:473–600
88. Hayes CE, Edelstein WA, Schenck JF, Mueller OM, and Eash M. An Efficient, Highly Homogeneous Radiofrequency Coil for Whole-Body NMR Imaging at 1.5T. *Journal of Magnetic Resonance* 1985; (63):622–8
89. Tropp J. The theory of the Bird-Cage Resonator. *Journal of Magnetic Resonance* 1989; 82(1):51–62. DOI: [10.1016/0022-2364\(89\)90164-9](https://doi.org/10.1016/0022-2364(89)90164-9)
90. Mispelter J, Lupu M, and Briguet A. NMR Probeheads for Biophysical and Biomedical Experiments. Second. Imperial College Press, 2015. Chap. 4 Interfacing the NMR Probhead:197–294
91. Murphy-Boesch J and Koretsky AP. An in Vivo NMR Probe Circuit for Improved Sensitivity. *Journal of Magnetic Resonance* 1983; 54(3):526–32. DOI: [10.1016/0022-2364\(83\)90333-5](https://doi.org/10.1016/0022-2364(83)90333-5)
92. Drozd JM and Joines WT. Determining Q Using S Parameter Data. *IEEE Transactions on Microwave Theory and Techniques* 1996; 44(I). DOI: [10.1109/22.543972](https://doi.org/10.1109/22.543972)
93. NEMA. Determination of Signal-to-Noise Ratio and Image Uniformity for Single-Channel Non-Volume Coils in Diagnostic MR Imaging. National Electrical Manufacturers Association, 2014. Available from: www.nema.org
94. Gudbjartsson H and Patz S. The rician distribution of noisy mri data. *Magnetic Resonance in Medicine* 1995; 34(6):910–4. DOI: [10.1002/mrm.1910340618](https://doi.org/10.1002/mrm.1910340618)
95. Crasto N, Kirubarajan A, and Sussman D. Anthropomorphic brain phantoms for use in MRI systems: a systematic review. *Magnetic Resonance Materials in Physics, Biology and Medicine* 2022; 35(2):277–89. DOI: [10.1007/s10334-021-00953-w](https://doi.org/10.1007/s10334-021-00953-w)

96. Mitchell HH, Hamilton TS, Steggerda FR, and Bean HW. The chemical composition of the adult human body and its bearing on the biochemistry of growth. *Journal of Biological Chemistry* 1945; 158(3):625–37. DOI: [10.1016/S0021-9258\(19\)51339-4](https://doi.org/10.1016/S0021-9258(19)51339-4)
97. Kumar A and Bottomley PA. Optimized quadrature surface coil designs. *Magnetic Resonance Materials in Physics, Biology and Medicine* 2008; 21(1-2):41–52. DOI: [10.1007/s10334-007-0090-2](https://doi.org/10.1007/s10334-007-0090-2)
98. Axel L, Costantini J, and Listerud J. Technical Note Intensity Correction in Surface-Coil MR Imaging. *AJR. American journal of roentgenology* 1987; 148(2):418–20. DOI: [10.2214/ajr.148.2.418](https://doi.org/10.2214/ajr.148.2.418)
99. Insko EK and Bolinger L. Mapping of the Radiofrequency Field. *Journal of Magnetic Resonance* 1993; 103(1):82–5. DOI: [10.1006/jmra.1993.1133](https://doi.org/10.1006/jmra.1993.1133)
100. Stollberger R and wach P. Imaging of the Active B1 Field in vivo. *Magnetic Resonance in Medicine* 1996; 35(2):246–51. DOI: [10.1002/mrm.1910350217](https://doi.org/10.1002/mrm.1910350217)
101. Ishimori Y, Shimanuki T, Kobayashi T, and Monma M. Fast B1 mapping based on double-angle method with T1 correction using standard pulse sequence. *Journal of Medical Physics* 2022; 47(1):93–8. DOI: [10.4103/jmp.jmp_78_21](https://doi.org/10.4103/jmp.jmp_78_21)
102. Zhang X. Sensitivity enhancement of traveling wave MRI using free local resonators: An experimental demonstration. *Quantitative Imaging in Medicine and Surgery* 2017; 7(2):170–6. DOI: [10.21037/qims.2017.02.10](https://doi.org/10.21037/qims.2017.02.10)
103. Hoult DI and Lauterbur PC. The Sensitivity of the Zeugmatographic Experiment Involving Human Samples. *Journal of Magnetic Resonance* 1979; 34(2):425–33
104. Autodesk. Fusion 360. 2023 Jun 22. Available from: <https://www.autodesk.com/products/fusion-360/overview?term=1-YEAR&tab=subscription>
105. Ortner M and Bandeira LGC. Magpylib: A free Python package for magnetic field computation. *SoftwareX* 2020; 11:100466. DOI: [10.1016/j.softx.2020.100466](https://doi.org/10.1016/j.softx.2020.100466)
106. Engelhardt M. LTspice. Ed. by Linear Technology AD. 2023. Available from: <https://www.analog.com/en/resources/design-tools-and-calculators/ltspice-simulator.html>
107. Regulation (EU) 2017/745 of the European Parliament and of the Council of 5 April 2017 on medical devices, amending Directive 2001/83/EC, Regulation (EC) No 178/2002 and Regulation (EC) No 1223/2009 and repealing Council Directives 90/385/EEC and 93/42/EEC (Text with EEA relevance.) 2017
108. Smith DC. Signal and noise measurement techniques using magnetic field probes. 1999. Available from: <https://api.semanticscholar.org/CorpusID:109310383>
109. Mispelter J, Lupu M, and Briguet A. NMR Probeheads for Biophysical and Biomedical Experiments. Second. Imperial College Press, 2015

110. Woletz M, Roat S, Hummer A, Tik M, and Windischberger C. Technical Note: Human tissue-equivalent MRI phantom preparation for 3 and 7 Tesla. *Medical Physics* 2021; 48(8):4387–94. DOI: [10.1002/mp.14986](https://doi.org/10.1002/mp.14986)
111. Schulte RF, Sacolick L, Deppe MH, Janich MA, Schwaiger M, Wild JM, and Wiesinger F. Transmit gain calibration for nonproton MR using the Bloch-Siegert shift. *NMR in Biomedicine* 2011; 24(9):1068–72. DOI: [10.1002/nbm.1657](https://doi.org/10.1002/nbm.1657)
112. Multicomp-pro. Soft Tinned Copper Wire, TCW16-500G-1230997 datasheet. 2023
113. RF/Microwave Products. Kyocera. 2023 :444–52. Available from: <https://catalogs.kyocera-avx.com/RF-Microwave.pdf>
114. Johanson Capability Guide. 10335. Johanson Manufacturing Corporation. 2017 :4

Appendices

A GitHub repository

A GitHub repository was created for the calculations and plots of this thesis. The README file briefly explains which files contain the final code.

The repository is called "[pyfigures-master](https://github.com/MariAlsaker/pyfigures-master)" and was published simultaneously with the ending of this master's project in June 2024.

Link: <https://github.com/MariAlsaker/pyfigures-master/tree/master>

B Travel report, PRESIMAL

In October 2023, I was fortunate to receive an invitation from the Max Planck Institute of Biological Cybernetics in Tübingen (see image in Figure 1), Germany, to seek assistance in constructing MRI surface coils for my master's project. Thanks to PRESIMAL's travel grant for researchers, I was able to go. My master's project is called "MRI Surface Loop Coil Development for the Study of Sodium Flux in the Visual Cortex". The original plan was to build a single surface loop coil to increase the resolution of sodium MRI (3T) image modalities available in Bergen. Hopefully, an increased resolution will enable future studies in functional sodium MRI with the goal of diagnosing patient groups with vascular impairment. Through discussions with Senior research Scientist Nikolai Avdievitch, currently working in Tübingen, the project was extended to 3 different surface coil designs to better account for the low SNR in sodium MRI.

At the max Planck Institute for Clinical Cybernetics, I spent 5 whole days with the research environment of Nikolai Avdievitch, where the focus generally is MRI coil development for brain imaging at high fields (>3T). Through discussions with Nikolai and his Postdoctoral fellow, Georgiy Solomakha, I learned how to proceed when building surface coils in an experimental setting, and what to be aware of when preparing coils for specific MRI experiments.

The visit to the Max Planck Institute for Clinical Cybernetics has strengthened collaboration and contributed to knowledge exchange. My research poster summarizing this work won a prize in the poster contest at the MMIV conference 2023. I am very grateful to PRESIMAL for the opportunity to learn about this important field within precision imaging from some of the most prominent researchers in the field.

Mari Maaløy Alsaker




Figure 1: *Picture of a famous neighborhood in Tübingen, Germany.*

C Poster presented at the MMIV conference in December 2023

In December 2023, the Mohn Medical Imaging and Visualization Center (MMIV) held its annual conference in collaboration with PRESIMAL, NorPrem, and Kin at the Grand Hotel in Bergen. This time, the conference heading read "Bringing AI and Precision Medisin to Patient Care". Speakers came from large health institutions in Norway and also from abroad.

Abstracts for poster presentations were gathered, and this project was included under the title "MRI surface loop coil development for studying the sodium flux in the visual cortex". Figure 2 shows the poster presented at this conference, which received the People's Choice Poster Award (third place).

More information about the conference can be found here: <https://mmiv.no/mmiv-conference-2023/>



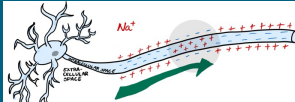
MRI Surface Loop Coil Development for the Study of Sodium Flux in the Visual Cortex

Mari Maaløy Alsaker¹, Alexander R. Craig-Craven^{2,3}, Alaa S. A. Assadi³, Ivan Maximov⁴, Nikolai Avdievitch⁵, Renate Grüner^{1,2}, Frank Riemer²

¹Department of Physics and Technology, University of Bergen, ²MMIV, Department of radiology, Haukeland University Hospital, ³Medical technical department, Haukeland University Hospital, ⁴Western Norway University of Applied Sciences, ⁵Max Planck Institute of Biological Cybernetics, Tübingen, Germany

INTRODUCTION

- fMRI BOLD (Blood-Oxygen-Level-Dependent imaging) method is the most used method for measuring brain activity in vivo, but not the most accurate [1].
- Intra and extra cellular sodium concentration changes are directly coupled to signal transmission along the nerve cells in the brain.

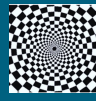


- In vivo functional sodium MRI (²³Na-MRI) at 3T can be a more accurate biomarker of brain activity, but improvements are needed to confirm this [2].
- Challenges connected to sodium MRI [3]:
 - Intrinsically low SNR
 - Lower gyromagnetic ratio than hydrogen
 - A relatively short relaxation time
- The sensing probe of an MR experiment is the RF coil, an antennae sensitive to the MR signal.
- The best sensitivity for a given sample is obtained when the probe coil fits as closely as possible to the sample [5].
- The visual cortex is close to the surface of our head and easy to stimulate for generating a fMRI signal.
- Before this project the only RF coil for sodium imaging available in Bergen was a birdcage head coil.

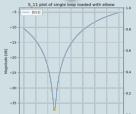
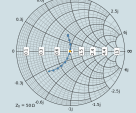
HYPOTHESIS

The SNR of sodium MRI experiments in Bergen can be improved by customizing an MR coil to fit the structure of interest, load it with an appropriate phantom and tune it to the sodium resonant frequency at 3T.

If the structure of interest is the visual cortex, penetration depth only needs to be 3-4 cm.



$\omega_0 = \gamma B_0 = \frac{1}{\sqrt{LC}}$
 $f_0 = 33.78 \text{ MHz}$

RESULTS

The three different coil designs have been constructed. Tuning and matching with a head phantom load have been performed using a VNA. Next, we want to test them in the MRI machine using a UTE sequence with 3D cones readout. Expected results, compared to birdcage coil:

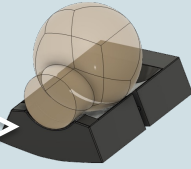
- Single loop coil:** higher SNR, but only a small area of approximately homogeneous field.
- Enhancing loop coil:** higher SNR [6] in the small area of homogeneous enhancement.
- Quadrature coil:** improved SNR by a factor of $\sqrt{2}$ compared to the single lonely loop coil [7].

METHODS

Different coil configurations were considered by simulating magnetic fields in python and electrical simulations in LTspice. The three following configurations were chosen:

- Single loop coil** – closer to the sample
- Enhancing loop coil** [6] – to enhance the circularly polarized field of the head coil.
- Quadrature coil** [7] – creates a circularly polarized field

Coil holders were designed in Autodesk Fusion 360 to fit closely to the human head or a Hoffman phantom




DISCUSSION

- Specialized MRI coils requires close collaboration with MRI manufacturers in most cases.
- Quantitative MRI requires detailed protocols for the MRI settings
- Sodium fMRI
 - Lower magnetic susceptibility than hydrogen.
 - Low SNR because of low sodium concentration in the human body



REFERENCES

- M. E. Raichle, Trends in Neurosciences, Feb 2009.
- C. A. Gandini Wheeler-Kingshott, Frontiers in Neuroscience, Nov 2018.
- O. Zanic, Journal of Magnetic Resonance Imaging, (1) 2021.
- M. T. Gohmare, The British Journal of Radiology, Mar 2021.
- J. Mispelner, NMR Probeheads for Biophysical and Biomedical Experiments, 2015.
- X. Zhang, Quantitative imaging in Medicine and Surgery, Feb 2017.
- C. Chen, Journal of Magnetic Resonance, 1993.




ACKNOWLEDGEMENTS

I would like to thank PRESIMAL for giving me the funding to travel to Tübingen to visit Max Planck Institute of Clinical Cybernetics. The travel gave me a lot of input on my master's project and good help from Nikolai and his postdoctoral fellow, Georgi Solomkha. Thanks to Atiq Ur Rehman for helping me with lab work at the University of Bergen. The 3D printing was done at the 3D print lab at Haukeland University Hospital with the valuable help of Rolf Arne Haakonson.

MAX PLANCK INSTITUTE
FOR BIOLOGICAL CYBERNETICS






Figure 2: Poster for the MMIV conference – This poster was presented at the international conference of MMIV held in Bergen on the 8th and 9th of December 2013.